UNIVERSITÀ
DEGLI STUDI
DI PADOVA

Sede Amministrativa: Università degli Studi di Padova

Centro di Ateneo di Studi e Attività Spaziali (CISAS) ‘‘Giuseppe Colombo’’

SCUOLA DI DOTTORATO DI RICERCA IN: Scienze Tecnologie e Misure Spaziali

INDIRIZZO: Misure Meccaniche per l'Ingegneria e lo Spazio

CICLO XXVII

NEW METHODOLOGIES IN RELIABILITY-BASED DESIGN OPTIMIZATION FOR STRUCTURES

Direttore della Scuola: Ch.mo Prof. Giampiero Naletto

Coordinatore d’indirizzo: Ch.mo Prof. Stefano Debei

Supervisore: Ch.mo Prof. Ugo Galvanetto

Co-supervisore: Ch.mo Prof. Mirco Zaccariotto

Dottorando: Marco Menegozzo

Summary

In the last decades, also due to the ever increasing importance assumed by civil air transport and its deregulation, the aeronautical structural design results to be characterized by two contrasting needs: on the one hand, the reduction of costs, and, on the other hand, the increase of the aircraft reliability. The costs minimization often results in fuel saving and, hence, in a mass optimization of the airplane; however, this risks to collide with the necessity to maximize the system reliability. The probabilistic approach to structural design, as it is proposed by the Reliability-Based Design Optimization (RBDO) phylosophy, allows to combine these antithetical requirements. After all, the traditional deterministic approach, which is based on the use of safety factors, often proves to be inadequate, since it can cause both a structural overweight and an underestimation of risks.

Probabilistic optimization consists of two separate processes: an external loop of deterministic optimization and an internal reliability assessment loop; these two steps are executed repeatedly, until the optimal configuration is reached; this condition is such that one or more performances are maximized and, at the same time, the feasibility constraints result to be respected with the desired level of likelihood.

Despite the growing interest towards the RBDO methodologies in the aeronautical field, to this day some applicative areas remain, which have not been sufficiently treated in literature; one of them is the aeroelastic field. Moreover, it is important to higlight that every single applicative case requires a deep study at a numerical level, aimed at determining which are the optimization and reliability assessment algorithms which are best fit for that particular situation; next, the two chosen algorithms have to be interconnected, to create a single probabilistic optimization loop.

One of the novelties that are proposed in this thesis consists on the use of RBDO in the frame design of a wing section, in order to prevent aeroelastic instabilities and to optimize such a structure; this optimization methodology, based on the elastic axis, had been previously applied by following a deterministic approach only (even though on a three-dimensional case). Another subject matter that was treated is essentially numerical: the creation of a simple RBDO algotithm, that was then successfully applied to the sizing of a beam. Subsequently, two analyses were carried on, aiming at applying RBDO first to the structure of a rectangular wing, and then to a shear web, and promising results were obtained in both cases.

In the future continuation of the present work, the various subject matters that have been treated will converge towards the determination of a global, unified procedure for the probabilistic optimization of a wing structure. Such an approach, that will also aim to prevent aeroelastic phenomena, will be devoted to reproduce as more realistically as possible the system and the surrounding environment; therefore, it will reckon with both structural nonlinearities and the forces generated by random gusts.

Sommario

Mai come oggi, complice anche la crescente importanza che ricopre il trasporto civile aereo e la liberalizzazione di tale mercato, la progettazione strutturale in ambito aeronautico risulta essere dominata da due esigenze contrastanti: da un lato, la riduzione dei costi, dall'altro, l'aumento dell'affidabilità del velivolo. La minimizzazione dei costi si traduce spesso in una minore spesa di carburante e, quindi, in un'ottimizzazione della massa dell'aereo; tuttavia, ciò rischia di scontrarsi con l'imperativo di massimizzare l'affidabilità del sistema. L'approccio probabilistico alla progettazione, così come proposto dalla filosofia Reliability-Based Design Optimization (RBDO), consente di coniugare queste due esigenze fra loro antitetiche. D'altro canto, il tradizionale approccio deterministico, basato sui coefficienti di sicurezza, risulta spesso inadeguato, in quanto può portare sia ad un eccessivo appesantimento strutturale che, caso opposto, ad una riduzione della sicurezza del sistema.

L'ottimizzazione probabilistica consta di due processi distinti: un loop esterno di ottimizzazione deterministica ed un ciclo interno di verifica dell'affidabilità: questa successione continua fino a che si converge alla configurazione ottimale, tale cioè da massimizzare una o più performances e, allo stesso tempo, che rispetti i vincoli relativi al livello minimo di sicurezza richiesto.

Nonostante il crescente interesse verso le metodologie RBDO in campo aeronautico, ad oggi permangono aree applicative che non sono ancora state sufficientemente trattate in letteratura; tra queste, l'ambito aeroelastico. Inoltre, va sottolineato che ogni singolo caso applicativo richiede uno studio approfondito, a livello numerico, volto a determinare quali siano gli algoritmi di ottimizzazione e di verifica dell'affidabilità che meglio si adattano alla situazione; questi, in seguito, vanno interconnessi per creare un unico ciclo di ottimizzazione probabilistica.

Uno degli elementi di novità che vengono proposti in questa tesi consiste nell'impiego della RBDO al progetto strutturale della sezione di un'ala, allo scopo di prevenirne fenomeni di instabilità di natura aeroelastica, oltre che di ottimizzarne la struttura; tale metodologia di ottimizzazione, basata sull'asse elastico, in precedenza risultava applicata (seppure ad un caso tridimensionale) soltanto in maniera deterministica. Un'altra tematica che è stata trattata ha invece una natura essenzialmente numerica: la costruzione di un semplice algoritmo di ottimizzazione probabilistica, applicato con successo al dimensionamento di una trave. In seguito, è stata affrontata un'analisi volta ad applicare la RBDO prima alla struttura di un'ala rettangolare e poi ad un longherone rastremato, con risultati promettenti.

Nella futura prosecuzione del presente lavoro, le varie tematiche affrontate confluiranno nella determinazione di una metodologia unitaria per l'ottimizzazione probabilistica della struttura di un'ala. Tale approccio, che mirerà anche alla prevenzione di fenomeni aeroelastici, si proporrà di riprodurre il sistema e l'ambiente circostante nel modo più fedele possibile, e terrà quindi conto delle nonlinearità strutturali e delle sollecitazioni dovute alle raffiche di vento aventi natura stocastica.

List of publications

- Coccon M. N., Menegozzo M., Galvanetto U., New methodologies in Reliability-Based Design Optimization for Aerospace Structures, WCCM XI - ECCM V - ECFD VI 2014 Conf. Proc., Barcelona, Spain, 20th - 25th July, 2014.
- Coccon M. N., Menegozzo M., Galvanetto U., A new methodology in Reliability-Based Design Optimisation for Aeronautical Structures, Royal Aeronautical Society *4th Aircraft Structural Design Conference* Conf. Proc., Belfast, Northern Ireland, 7th - 9th October, 2014.

Table of contents

Chapter 1

Introduction

1.1. Originality and motivation

In the last decades, there has been an ever increasing motivation for aerospace systems to achieve both better performances and lower costs and, on the other hand, a higher reliability. The need to minimize weight and maximizing performances collides with the costly and fatal conseguences of failure, due to the extreme difficulty to perform maintenance during flight. Moreover, a diversified amount of uncertainties arises from the system and from the surrounding environment, which causes the system performances to change or fluctuate, thus constituting an inherent source of risk. Reliability-Based Design Optimization (RBDO) provides an answer to this kind of issues (Yao *et al.*, 2011). RBDO is a probabilistic design methodology that allows to reckon with these contrasting needs: indeed, it can be used to enhance the reliability of a physical system and to maximize its performances, in full compliance with the desired feasibility constraints. In general, a higher reliability implies a greater cost, and a lower reliability also implies a greater cost due to failure consequences (Du, 2006): this proves the importance of a probabilistic approach in design, in order to achieve the desired trade-off between performances and safety.
In traditional design, to account for uncertainties, safety factors are widely used (Yao *et al.*, 2011); anyway, such an approach poses some limitations: indeed, bigger safety factors could result in a performance loss; on the other hand, being these coefficients defined based principally on the past experience, it could be likely that they don't keep into account all the possible risks, thus leading to a potential danger.

RBDO allows to optimize the desired performances (e.g., the mass minimization of an aeronautical device) while limiting the probability of failure to a maximum predefined value. The difference between deterministic optimization and probabilistic optimization (performed via RBDO) is depicted in Fig. 1.1. We want to design a system (for instance, a beam) so that its mass results to be minimized, and let us call x_1 and $x_2$its geometrical dimensions, that can be varied (as "degrees of freedom") to reach the desired goal: for example, the dimensions of the beam rectangular cross-section. Clearly, the optimization process is limited by some feasibility *constraints* (see Fig. 1.1), such as the yield stress and the maximum allowed deflection. Generally, a deterministic optimization loop continues automatically until one of the deterministic constraints is reached: this is the case of the red *design point* of Fig. 1.1; however, this point corresponds to a 50% probability of failure, since it is located exactly on the border between the feasible and the infeasible regions. Conversely, the *reliable optimal solution* (i.e., the green design point in Fig. 1.1) could result more "prudent", but it meets the predefined reliability level.

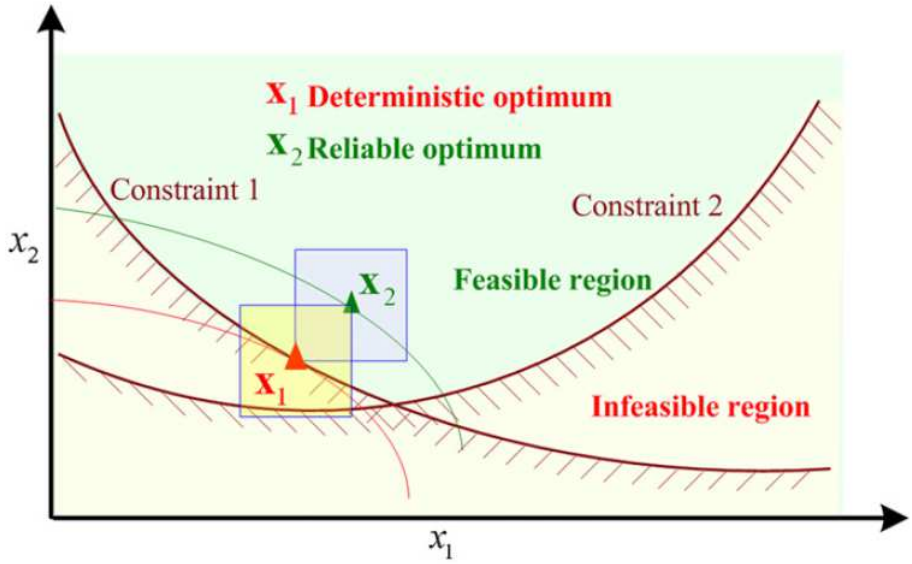

Figure 1.1: graphical representation of Reliability-Based Design Optimization (from W. Yao e*t al.*, 2011).

Despite the probabilistic approach is already practiced in many branches of the aerospace field, at present there is an ever increasing interest on the unified approach that is offered by RBDO methodologies; moreover, a lack of RBDO literature exists for some particular aerospace applications, such as in the aeroelasticity field. In addition, it is important to highlight that, for every single different structural contest, one has to build and adapt its correlated RBDO implementation, such that it results to be as more accurate and stable as possible, and less time-consuming; to achieve this result, one has to investigate the most suitable algorithms for both reliability analysis and optimization, and then integrate them into a global unified procedure.
Huo *et al.* (2013) proposed a methodology for the wing optimization based on elastic axis, limited to a deterministic case, in which the goal of minimizing the structural mass is pursued together with the need of preventing aeroelastic instabilities. In the present thesis, such a problem was revisited from a reliability-based point of view. Moreover, an investigation of some possible ways to reduce the computational time in structural RBDO was made, also by employing Design Of Experiments (DOE) and Response Surface Methodology (RSM); a very simple RBDO algorithm is presented as well.

1.2. Outline

Chapter 2 provides the prerequisites to be able to deal with reliability assessment; hence, the fundamentals of uncertainty modeling are revised, with a particular focus on the fundamentals of probability theory and statistics. Then, uncertainty analysis is presented, and some key concepts, such as that of *reliability* and *probability of failure*, are introduced. In Chapter 3, the main reliability assesssment methods are illustrated: Monte Carlo Simulation (MCS), First and Second Order Reliability Methods (FORM and SORM), and First Order Second Moment method (FOSM); then, such algorithms are tested on some structural examples, in order to evaluate their efficiency. In Chapter 4, deterministic optimization is treated, and the various methodologies for implementing it are illustrated: the analytical method, the graphical method, the *gradient-based numerical methods*, and *genetic algorithms* (GA). Chapter 5 serves to describe how Reliability assessment and

deterministic optimization converge into *Reliability-Based Design Optimization* (RBDO); Then, a very simple RBDO algorithm that was developed is presented; subsequently, such an algorithm is applied to the probabilistic design of a cantilever beam. Finally, two of the best-established RBDO algorithms are introduced: Reliability Index Approach (RIA) and Performance Measure Approach (PMA). Chapter 6 concerns the application of the reliability-based design to some aeronautical structures, and aims to describe the RBDO cases with an increasing level of lifelikeness. In the first case, the probabilistic design of a wing airfoil structure is made; the main goals of this analysis are mass minimization and the prevention of aeroelastic instabilities. Subsequently, the probabilistic design of a rectangular wing is described, in which optimization is performed via a genetic algorithm, and Monte Carlo Simulation (MCS) is used to compute the system reliability. The same approach is then used for the design of a tapered shear web, in which Response Surface Methodology (RSM) is used to simplify the expression of the constraint function and to reduce the computational costs. Eventually, Chapter 7 contains the conclusions, in which the main results are recapitulated, and some recommendations on the future continuation of the work are briefly described.

Chapter 2

Uncertainty modeling and analysis

2.1. Introduction

Uncertainty can be defined as the difference between the complete knowledge of a system and its current knowledge.

While studying a physical system, it is useful to split the lack of knowledge into two major families: *aleatory uncertainty* and *epistemic uncertainty*. *Aleatory uncertainty* (or s*tochastic uncertainty*) originates from the inherent variability of a system or the surrounding environment under study; it is related to *natural variability*, and cannot be completely eliminated by collecting more information. Therefore, aleatory uncertainty is *irreducible*. On the other hand, *Epstemic uncertainty* accounts for the incomplete knowledge of nature: this includes the properties of the system under study, as well as its time-varying interactions with the external environment. This lack of knowledge can be, at least partially, overtaken through the collection of more data; thus, epistemic uncertainty is *reducible*.

In the present work, we will focus on aleatory uncertainty. To quantify aleatory uncertainty, probability theory is commonly used (Du X., 2006).

Uncertainties on parameters and model features, as well as numerical errors, have an important impact on the system performances. Neglect or uncorrect treatment of uncertainty may lead to low quality and reliability, costly warranties, over-designed (conservatively) products, low costumer satisfaction, up to catastrophic consequences (Du X., 2006).

In engineering design, uncertainty can be faced at three complementary levels: *modeling*, *analysis* and *design*.

First level: *uncertainty modeling*

The goal of uncertainty modeling is to provide a mathematical quantification of uncertainty. To do so, probability theory and statistics are often used, through which the uncertainty is finally expressed as a random variable with its probability distribution. The latter is the input to uncertainty analysis (second level).

Second level: *uncertainty analysis*

Uncertainty analysis aims to quantify the uncertainty of the design performance (model output) given the uncertainty of the model input (which is provided by *uncertainty modeling*) (Du X.,

2006). Thanks to uncertainty analysis, it is possible to forecast the influence of uncertainty on the design performance, and to evaluate the design reliability.

Third level: *design under uncertainty*

The goal of design under uncertainty is to reduce the effects of uncertainty by making appropriate design choices. Depending on the design requirements, the attention may be focused on safety, robustness or quality.

Design under uncertainty is an iterative process, and every updated design will undergo uncertainty analysis.

2.2. Basics of uncertainty modeling

Uncertainty modeling aims to quantify uncertainty through mathematical tools. A brief overview of some fundamental probability theory and statistics concepts will be presented below.

Probability

Probability quantifies the likelihood of occurrence of an event (Du X., 2006). The probability of an event $\boldsymbol{E}$ is defined as

$$P(\boldsymbol{E}) = \frac{The\ number\ of\ ways\ the\ event\ \boldsymbol{E}\ can\ occur}{The\ total\ number\ of\ possible\ outcomes} \tag{2.1}$$

Probability density function

Let us consider a spacecraft orbiting around a planet, which experiences a temperature gradient, at every orbit, between the perihelion and the aphelion. Let us want to record the maximum temperature X which is experienced by a particular instrument at every orbit. One wants to know which is the probability for the temperature to be in any given interval, i.e., the probability distribution for T. To answer this question, one can record the maximum instrument temperature at every orbit and then plot a *histogram* (Figure 2.1 (a)).

In order to be more accurate, one can reduce the bin size (Figure 2.1 (b)). In the limit case, the histogram becomes a smooth curve (Figure 2.1 (c)), which is the *probability density function* (*pdf*), or *probability distribution*, for X.

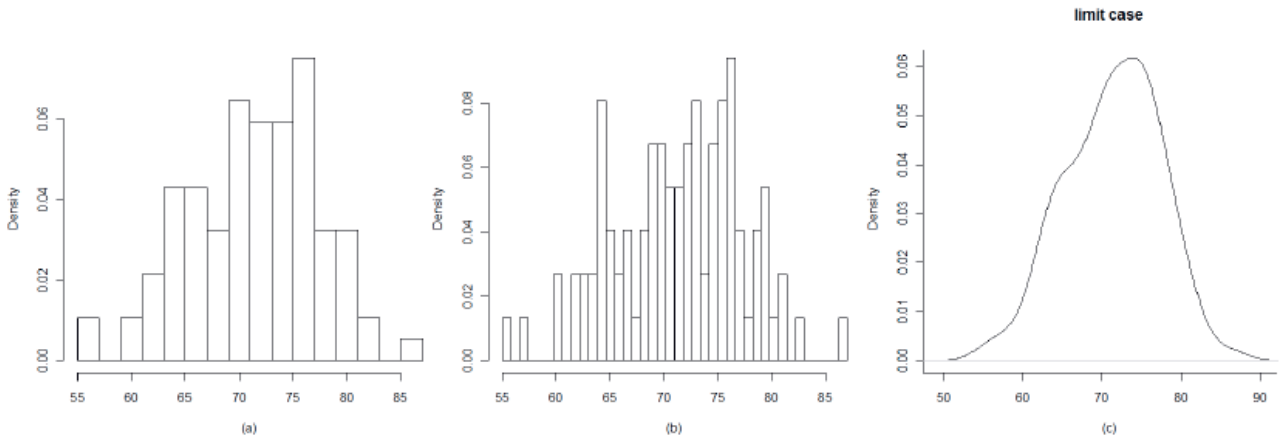

Figure 2.1: if one reduces the bin size of a histogram, the limit case is given by the *probability density function (pdf)* of the random variable under study (from Zhang, 2008).

A mathematical formulation for the *pdf* is provided below.

Let X be a continuous random variable. Then, a probability density function (pdf) of X is a function $f(X)$ such that, for any two values a and b with $a \leq b$,

$$P(a \leq X \leq b) = \int_a^b f(X)dX \qquad (2.2)$$

where P stands for *probability*.

The definition above is valid under the two following conditions:

1) $f(X) \geq 0$ for every X

2) $\int_{-\infty}^{+\infty} f(X)dX = 1$

Thus, the probability for the instrument to reach a maximum value of tempreature between 60º and 70º is given by the grey area (Figure 2.2) divided by the total area under the *pdf* curve.

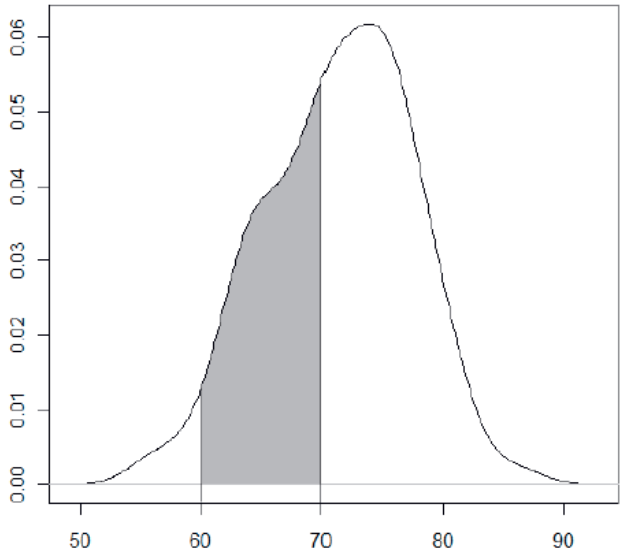

Figure 2.2: the probability for the random variable X to lie in the selected interval is equal to grey area divided by the total area under the *pdf* curve (from Zhang, 2008).

Cumulative distribution function

The cumulative distribution function $F(x)$ for a continuous random variable X with probability density function f is defined by

$$F(x) = P(X \leq x) = \int_{-\infty}^{x} F(X)\, dX \qquad (2.3)$$

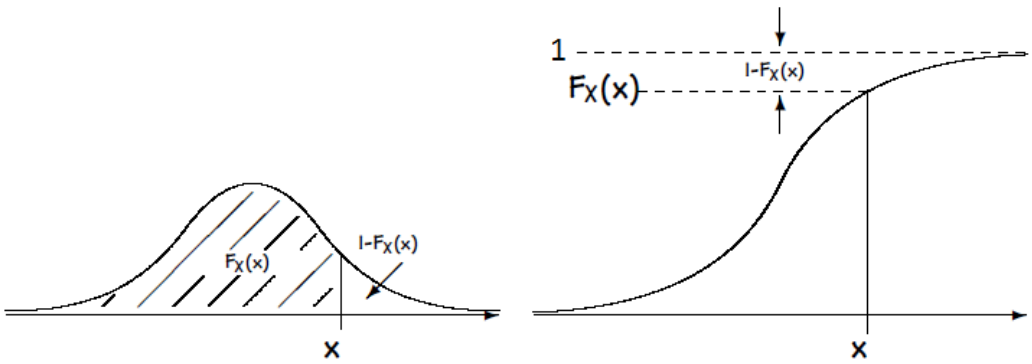

Figure 2.3: probability density function (left) and cumulative distribution function (right) (from B. Schroeder).

where *x* is meant as a particular value that is assumed by the random variable *X*.

An important theorem on cumulative distribution functions is reported below.

Theorem:

Let X be a random variable with cumulative distribution function F. Then, for a real number a, we have

$$P(X > a) = 1 - F(a) \tag{2.4}$$

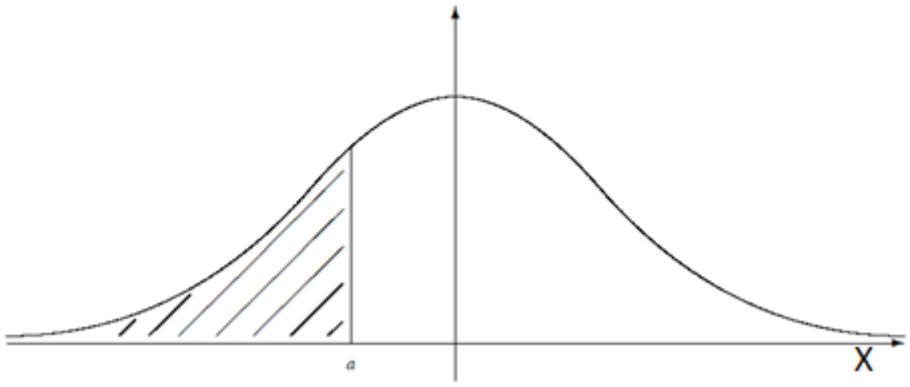

Figure 2.4: the probability, for the random variable X, to be bigger than a real number a is the reciprocal of the cumulative distribution function at a (from B. Schroeder).

Mean

The *mean* of a continuous random variable X with probability density function f_X is

$$\mu_X := \int_{-\infty}^{+\infty} X\, f_X(X) dX \tag{2.5}$$

Variance

Variance is a measure of how spread a distribution around its mean is, and is expressed as

$$\sigma^2 = \int_{-\infty}^{+\infty} (X - \mu_X)^2 f_X(X) dX \tag{2.6}$$

For a finite number N of samples, the variance is calculated by

$$S^2 = \frac{1}{N} \sum_{i=1}^{N} (x_i - \mu_X)^2 \tag{2.7}$$

As N increases significantly, the variance expression is given by

$$S^2 = \frac{1}{N-1} \sum_{i=1}^{N} (x_i - \mu_X)^2 \tag{2.8}$$

which best approximates the variance value when *N* approaches infinity.

Percentile value

Consider a continuous random variable *X* and a real number α; the percentile value x^{α} is a value below which the probability of the actual values of *X* being equal or less than x^{α} is α, i.e.

$$P(X \leq x^{\alpha}) = F_X(x^{\alpha}) = \int_{-\infty}^{x^{\alpha}} f(X)dX = \alpha \qquad (2.9)$$

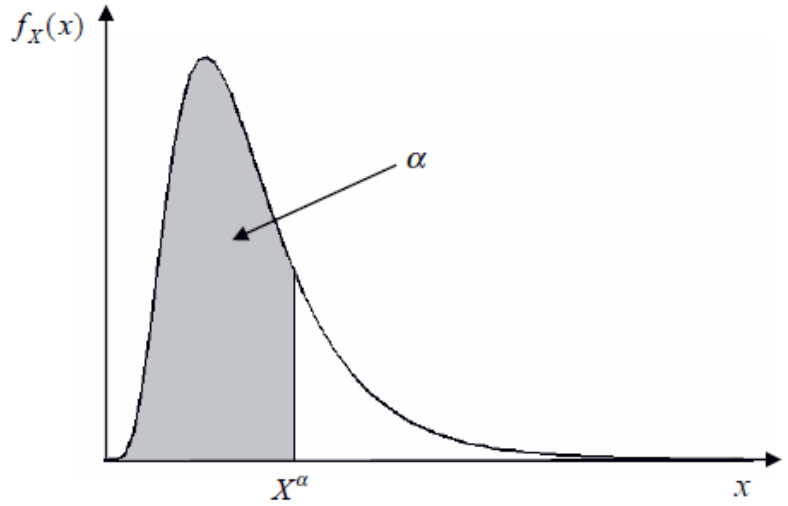

Figure 2.5: percentile value of a distribution. The grey area is equal to α (from Du X., 2006).

Normal distribution

A *Normal Distribution* (*also called Gaussian Distribution or Bell Curve*) is a particular kind of theoretical frequency distribution, which is symmetric about its mean. The maximum value of the pdf is reached at the mean of the random variable, and such function decreases monotonically along both directions, so that the function is bell-shaped. The distribution is defined by two parameters: the mean (μ_X) and the standard deviation (σ_X). Some features regarding the items concentration about the mean are shown in Figure 2.6.

This is the most popular statistical distribution, and will often be used in this work.

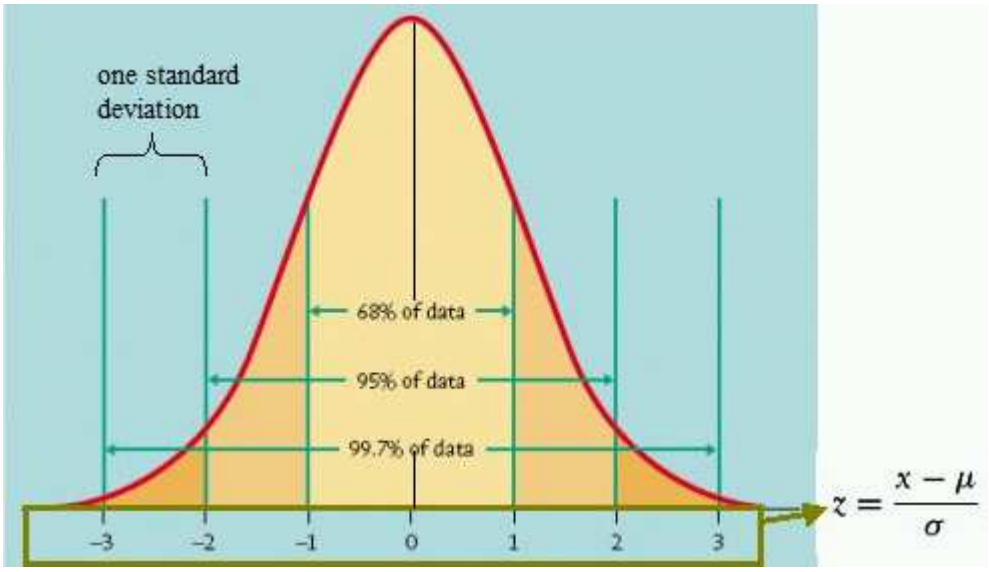

Figure 2.6: a (standard) normal distribution with some data regarding the items concentration about the mean (from faculty.virginia.edu).

Considering a normally distributed random variable *X*, its normal distribution is determined by a mean value μ_X and a standard deviation σ_X, and its notation is $X \sim N(\mu_X, \sigma_X)$.

The *probability density function* (*pdf*) of a normal distribution is given by:

$$f_X(x) = \frac{1}{\sqrt{2\pi} * \sigma_X} * \exp\left[-\frac{1}{2} * \left(\frac{x-\mu_X}{\sigma_X}\right)^2\right], \qquad -\infty < x < +\infty \tag{2.10}$$

The *cumulative distribution function* (*cdf*) is expressed as

$$F_X(x) = \int_{-\infty}^{x} \frac{1}{\sqrt{2\pi} * \sigma_X} * \exp\left[-\frac{1}{2} * \left(\frac{x-\mu_X}{\sigma_X}\right)^2\right] dx, \qquad -\infty < x < +\infty \tag{2.11}$$

A normal distribution with zero mean (μ = 0) and unit variance ($\sigma^2 = 1$) is called a *standard normal distribution* (Figure 2.6).

A normal random variable $X \sim N(\mu_X, \sigma_X)$ can be transformed into a standard normal variable through the following expression:

$$Z = \frac{X-\mu_X}{\sigma_X} \tag{2.12}$$

its probability density function $\varphi(Z)$ and cumulative distribution function $\Phi(Z)$ are given by

$$\varphi(Z) = \frac{1}{\sqrt{2\pi}} exp\left(-\frac{1}{Z^2}\right) \qquad -\infty < z < +\infty \tag{2.13}$$

$$\Phi(Z) = \int_{-\infty}^{z} \frac{1}{\sqrt{2\pi}} exp\left(-\frac{1}{Z^2}\right) dz \qquad -\infty < z < +\infty \qquad (2.14)$$

2.3. Uncertainty analysis

An engineering system can be schematized through a mathematical model with some inputs and outputs.

The inputs are design variables and random variables. While design variables are under the control of the designer (e.g., dimensions or the choice of materials), random variables account for all those conditions which can't be modifed by him (e.g., the external temperature or the direction and speed of wind gusts).

The system output or response, on the other hand, can be seen as a *performance*, such as the stress or strain which is experienced by a structure.

If the input variables $\boldsymbol{X}$ are random, the output variable Y will be random as well.

A major issue in uncertainty analysis is to evaluate the impact of input parameters uncertainties on the system response. From a mathematical point of view, the goal is to evaluate the distribution of a response variable given the distributions of the input variables (Du X., 2006).

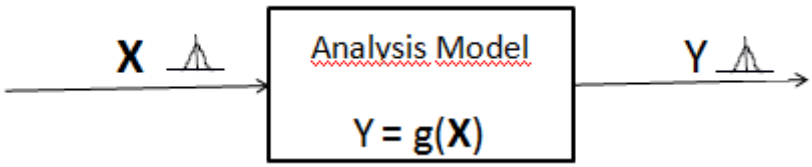

Figure 2.7: mathematical model for the probabilistic design of an actual engineering system.

From now on, the mathematical model $Y = g(\boldsymbol{X})$ will be called *performance function*, which describes the relation between the response and the input variables.

The task of uncertainty analysis is to quantify the uncertainty associated with the model output (Du X., 2006).

2.3.1. Reliability

Reliability is the likelihood that a component (or a system) will perform its intended function without failure for a specified period of time under stated operating conditions (Yao et al., 2011, Ingram-Cotton et al., 2007, and MIL-STD-785REVB, 1980).

For a system to be considered safe, the value of the performance function $Y = g(\boldsymbol{X})$ has to lie over a certain threshold. If it outgoes such a limit, the system cannot be considered safe anymore. The threshold value is defined as the *limit state*, and divides the random variables space into a *safe region* and a *failure* (or *unsafe*) *region*. From now on, $Y = g(\boldsymbol{X}) = 0$ will be considered as the threshold value for the performance function, i.e. the *limit state function*. Hence, the safe region extends where $g(\boldsymbol{X}) > 0$, whereas the area with $g(\boldsymbol{X}) < 0$ is the *unsafe region* (Figure 2.8).

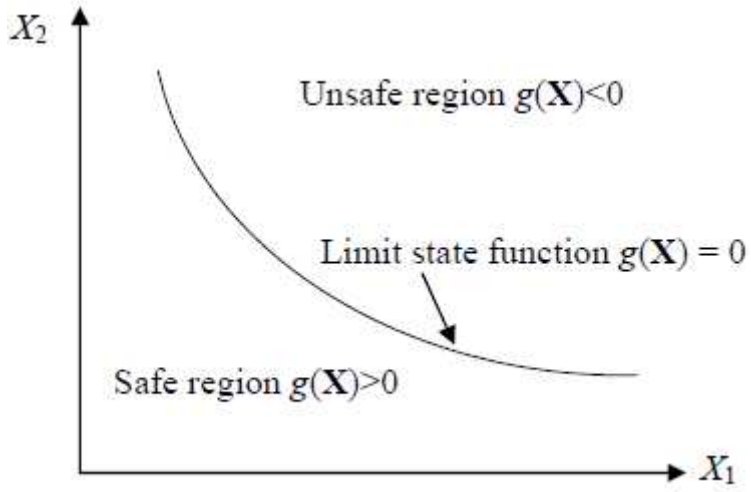

Figure 2.8: graphical expression of the limit state function for a two-dimensional problem (from Du X., 2006).

A simple engineering example of what has just been presented is the case of a specimen being stimulated; in this case, the performance function can be defined as

$Y = g(\boldsymbol{X}) = X_2 - X_1$, where X_1 is the acting stress, and X_2 is the strength of the material.

The *Reliability* (R) is expressed as the probability, for the performance function, to be above the limit-state value, i.e.,

$$R = P(g(\boldsymbol{X}) > 0) \tag{2.15}$$

while the *probability of failure* (p_f) is defined as

$$p_f = 1 - R = P(g(\boldsymbol{X}) < 0) \tag{2.16}$$

In structural applications, the probability of failure is generally low; hence, it is often convenient to relate it to the left tail of the performance function (Figure 9).

This could be the case of the previous example, where the probability of failure is expressed as

$$p_f = P(g(\boldsymbol{X}) < 0) = P(X_2 - X_1 < 0) \tag{2.17}$$

which reports on the (very low) probability of the stress overtaking the material strenght.

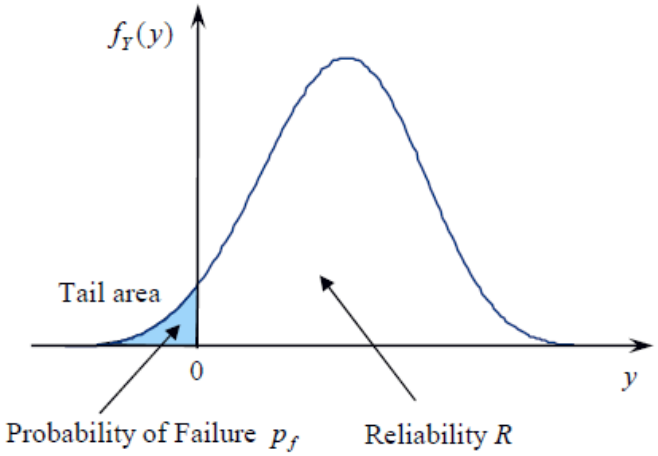

Figure 2.9: *pdf* of a performance function $y = g(\boldsymbol{X})$. The shaded area refers to the *unsafe region*, i.e., the one such that $y = g(\boldsymbol{X}) < 0$ (from Du X., 2006).

If one needs to improve the reliability of a design, it is possible to do it by shifting the *pdf* (through varying the value of the mean) and/or by shrinking it (i.e., reducing variance) (see Figure 2.10). This can be done by conveniently changing the values of the design variables, and this is one of the goals of *Reliability-Based Design*.

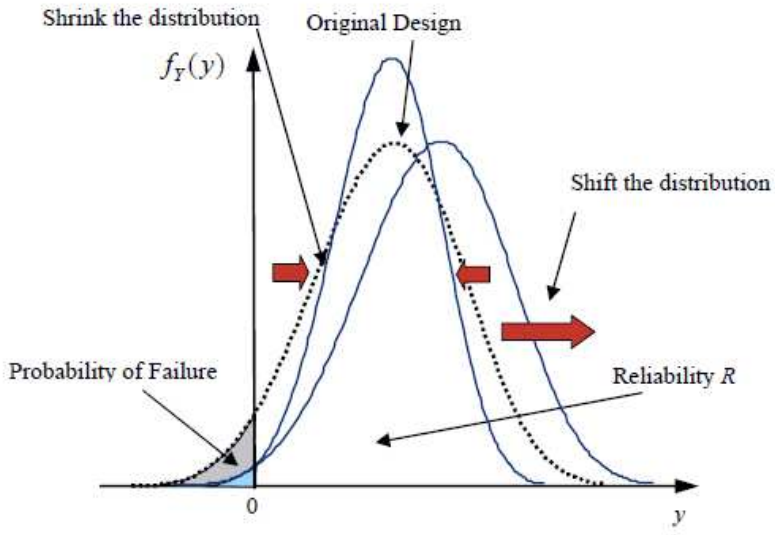

Figure 2.10: reliability can be increased trough acting on the mean and the variance of the *pdf*(s) (from Du X., 2006).

2.3.2. Robustness

Robustness is the degree of tolerance of a system to be insensitive to variations in both the system itself and the environment (Yao et al., 2011). In other words, a design is considered as *robust* if its functionality is not significantly affected by small changes in parameters, models, assumptions and in the external environment (IEEE Std. 933-1999). Figure 2.11 depicts the case of the response *pdf* of two different designs: even though the mean is the same, *Design 1* is more robust than *Design 2*, because of its lower standard deviation.

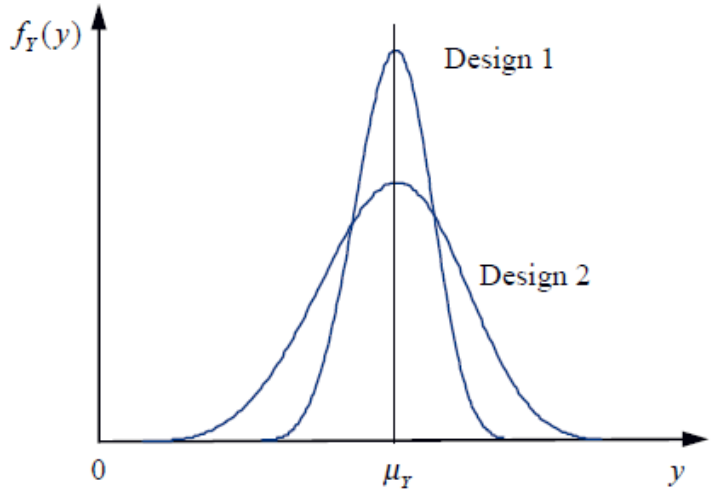

Figure 2.11: due to its lower standard deviation, *Design 1* is more robust than *Design 2* (from Du X., 2006).

Robust Design is mainly concerned with the event distributed near the mean of the probability density function (small fluctuations around the normal status, see Figure 2.12), whereas Reliability-Based Design Optimization is concerned with the performance distribution at the tails of the probability density function (extreme events) (Yao et al., 2011).

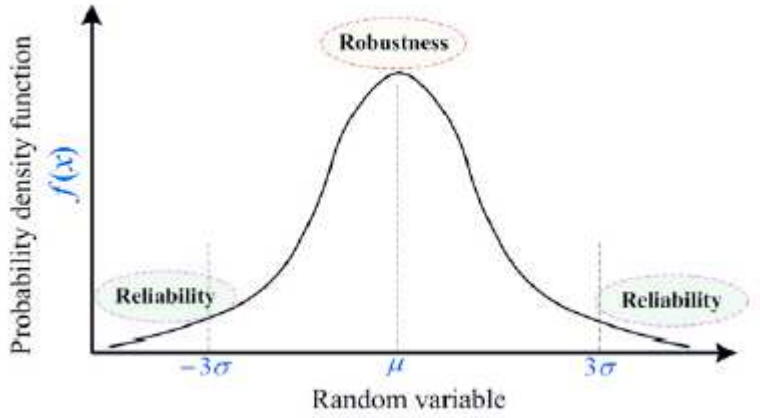

Figure 2.12: robustness and reliability in terms of probability density function (from Yao *et al.*, 2011).

In other words, reliability is mostly focused on safety for preventing catastrophic events, whereas robustness deals with the everyday fluctuations and aims mainly to avoid quality loss.

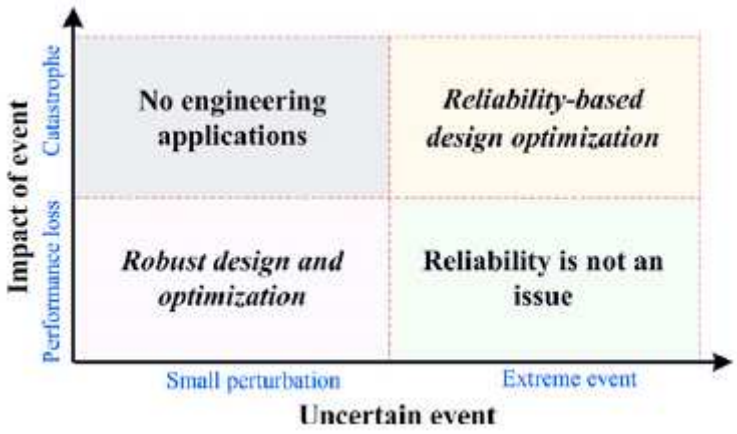

Figure 2.13: domains of application of Robust Design and Reliability-Based Design (from Yao *et al.*, 2011).

2.3.3. Uncertainty analysis algorithms

The main goal of uncertainty analysis is to compute the probability of failure of a system.

Let us consider a *n-dimensional, joint probability density function* $f(\boldsymbol{X}) = f(\boldsymbol{X}_1, \boldsymbol{X}_2, \dots \boldsymbol{X}_n)$. The probability of failure can be computed by the following integral (Breitung, 1989):

$$p_f = \int_D f(\boldsymbol{X}) d\boldsymbol{X} \tag{2.18}$$

where the failure domain *D* is defined as $g(\boldsymbol{X}) < 0$.

In engineering applications, performance functions are normally complex and nonlinear; furthermore, a high number of random variables is usually involved, making multidimensional integration computationally prohibitive. In many cases, performance functions are a black box (e.g., Finite Element Modeling or Computational Fluid Dynamics codes). Therefore, it is frequently almost impossible to find a closed form analytical solution for determining the probability of failure.

To overcome this issue, numerical approximation methods are used. There are three main categories for such algorithms: *uncertainty analysis methods*, *sampling-based methods* and *surrogate models*. Even though they will be treated in detail in the next chapter, a brief hint to them is made below.

Uncertainty analysis methods

These algorithms are used to simplify the integrand in Eq. (18) and to approximate the performance function $g(\boldsymbol{X})$, in order to obtain an analytical solution for the integral. Among these approximation methods, First Order Reliability Method (FORM) and Second Order Reliability Method (SORM) are the most widely applied in engineering problems (Yao et al., 2011, and Rackwitz, 2001).

Sampling-based methods

Also known as *Monte Carlo Simulation* (MCS) methods, they are a class of computational algorithms which perform repeated sampling and simulation, in order to compute the statistics of the response quantities of interest (Yao *et al.*, 2011, Helton *et al.*, 2006, and Landau *et al.*, 2005), like for example the probability of failure. The MCS methods accuracy can be improved by increasing the number of samples, up to tend to the theoretically exact solution.

Surrogate models

When the evaluation of the performance function $g(\boldsymbol{X})$ is strongly time-consuming, a great issue to deal with is the necessity to reduce the computational overload. This task can be accomplished by substituting the original, complex analysis model with a simpler one (i.e., the *surrogate model*). Hence, the related performance functions are more elementary and easier to handle.

2.4. Conclusions

In this chapter, a brief review of uncertainty modeling was made, followed by an introduction to uncertainty analysis. Uncertainties can be *epistemic* or *aleatory*; while the first one can be reduced through a better knowledge of the engineering model and its environment, the latter are irreducible. A generic engineering system can be schematized by an analysis model, which has some inputs (i.e., random variables $\boldsymbol{X}$ and design variables $\boldsymbol{d}$), and one (or more) output(s) Y (i.e., the system *response*). The uncertainties associated with the model input will be propagated to the model output, and this process is described by one or more performance functions $Y = g(\boldsymbol{X})$. In engineering design, uncertainties have to be managed at three different levels. Firstly, input uncertainties must be mathematically quantified through uncertainty modeling, which is performed via statistic tools; as a result, each of them can be expressed as a random variable with its *probability distribution function* (*pdf*). The second step consists in *uncertainty analysis*, which allows to compute the uncertainty associated with the model output, and to determine the system reliability; however, in many engineering applications, this can be computationally prohibitive; to overcome this issue, numerical approximation methods are used. The third step consists in performing *design under uncertainty*, whose main goal is to reduce the impact of uncertainties in the final design by making opportune design choices (i.e., by setting the optimal values for the design variables $\boldsymbol{d}$).

Chapter 3

Reliability assessment methods

3.1. Introduction

To compute the probability of failure of a physical body, one has to deal with non-deterministic quantities (i.e., the *n* random variables $\boldsymbol{X}$) and, hence, the entity of at least some parameters can't be fixed *a priori*.

An uncertainty-based approach is given by considering the possible outcomes of some experiments (e.g. a quantitative measure) or some physical quantities as random variables that are subject to a particular probability distribution; for simplicity, we will henceforth consider *normal distribution*, that is the most commonly used.

A system reliability is determined by its performance function $g(\boldsymbol{X})$, which returns a negative value under system failure conditions, and a positive value when the system is safe. Hence, it can be viewed as the difference between resistance, $\boldsymbol{R}$, and load, $\boldsymbol{S}$:

$$g(R,S) = R - S \tag{3.1}$$

Both the resistance and the load of an engineering system depend on random variables; therefore, they each have a probability distribution: $f_R(R)$ and $f_S(S)$. If these two *pdf*s are combined, they give rise to a *joint probability density function*, i.e., $f_{R,S}(R,S)$ (Figure 3.1).

Once the joint *pdf* is known, the probability of failure is calculated by the following integral:

$$p_f = \int_{-\infty}^{+\infty} \int_{-\infty}^{r \leq s} f_{R,S}(R,S) dr ds \tag{3.2}$$

Such an equation can be generalized to the *n*-dimensional case, with *n* = total number of random variables:

$$p_f = P\{g(\boldsymbol{X}) < 0\} = \int_{g(\boldsymbol{X})<0} f_{\boldsymbol{X}}(\boldsymbol{X}) d\boldsymbol{X} \tag{3.3}$$

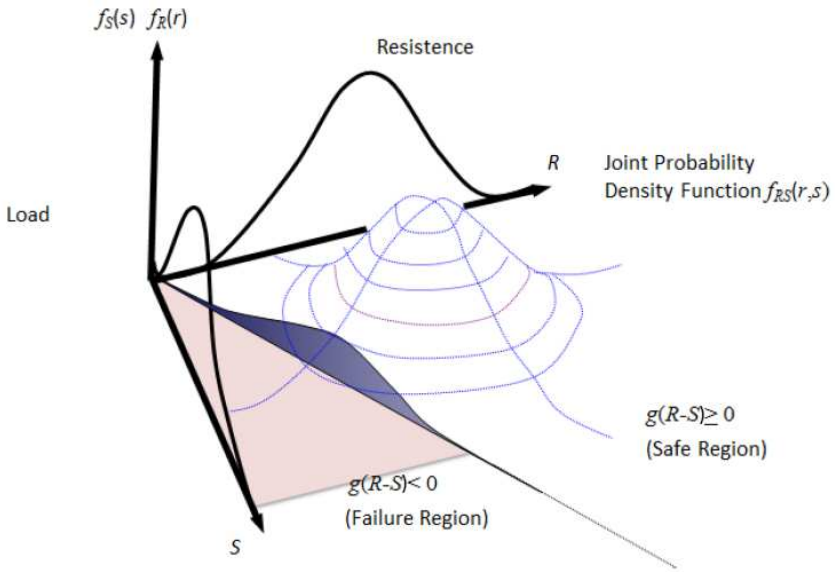

Figure 3.1: joint probability density function, divided between the safe region and the failure region (from uniandes.edu.co).

If one performs *m* experiments (which are depicted in Figure 3.2 as black dots), the probability of failure of a system is equal to the probability of falling in the region where the performance function is less than zero, i.e., the *failure region*.

Therefore,

$$p_f = \frac{number\ of\ items\ falling\ inside\ the\ \boldsymbol{Failure\ region}}{total\ number\ of\ items}$$

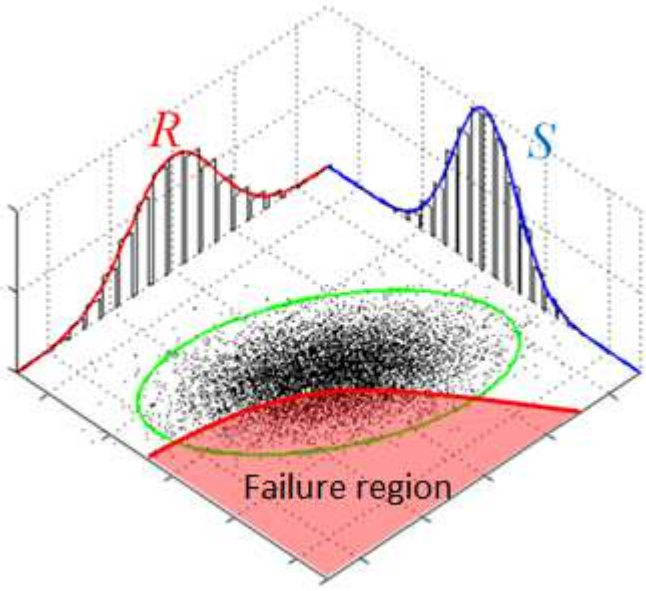

Figure 3.2: let us perform *m* experiments. The probability of failure is the ratio between the number of items falling inside the failure region and the total number of experiments, i.e., *m*.

In order to compute the probability of failure (or the reliability) of a given structure, several different methods can be employed. In this chapter, an overview will be made on the most commonly used methodologies, which belong to the two families of Uncertainty Analysis methods and Monte Carlo Simulation (MCS).

3.2. Monte Carlo Simulation (MCS)

Although statistical methods are gradually spreading more and more in engineering applications, many engineers have only a limited knowledge of probability and statistics. Monte Carlo simulation provides a straightforward approach if one doesn't have a deep theoretical knowledge of statistical methods.

Monte Carlo Simulation (MCS) methods, also called *sampling-based methods*, are a class of algorithms which consists on performing a very large random sampling and making a huge number of simulations on computer, so as to compute the statistics of the response quantities of interest.

Provided a sufficient number of samples, MCS methods can reach the desired level of accuracy; the latter tends to the exact solution as the number of experiments approaches infinity. Because of its robustness, MCS is often used as a benchmark for evaluating the performance of new uncertainty analysis techniques (Yao et al., 2011).

MCS normally requires a huge number of simulations, and can be computationally demanding. Therefore, it may not be suitable for some complex engineering applications, where the need to repeatedly execute a lot of complicated calculations would be computationally prohibitive. Hence, Monte Carlo Simulation is widely used in engineering applications where the model evaluations are not onerous. Alternatively, the computational cost of MCS may be optimized by implementing *variance reduction techniques*, such as *Importance Sampling*, which allows to strongly reduce the number of samples.

Coming back to crude Monte Carlo, a first, simple application of this methodology consists of calculating the area of a circle if one doesn't know its formula.

Let us consider a circle that is inscribed inside a square (see Figure 3.3), and let us randomly sample some points inside the area of the square. Then, divide the number of the points inside the circle by the number of the points that fall outside the square but outside the circle. As the number of the

points (i.e. the samples) increases, the result of the division gradually approaches the value of $\pi/4$, that is just the ratio between the areas of the two geometric figures.

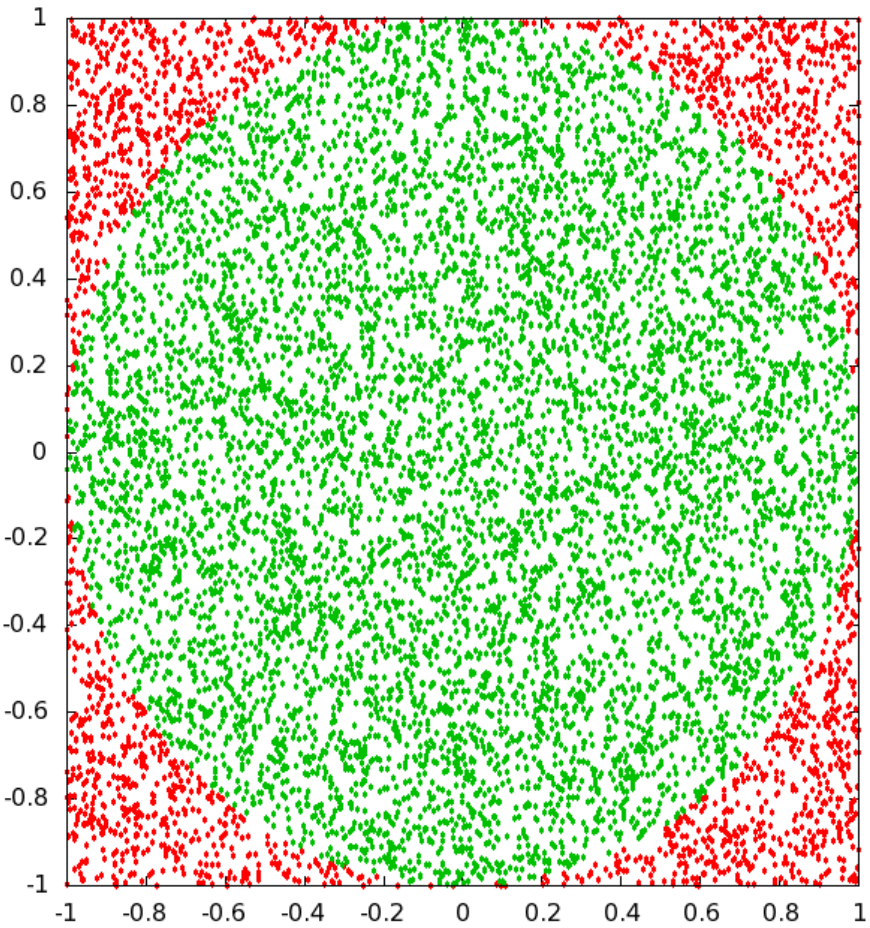

Figure 3.3: Computing the ratio between the areas of a circle and a square (inside which it is inscribed) through Monte Carlo Method (from Fattaruso J.).

Some theoretical basics underlying crude Monte Carlo Method are given below.

Even if MCS is applicable to both the cases of dependent and independent variables, the present dissertation is focused on the case in which only independent random variables are involved.

Let us consider an engineering model whose operation is expressed by a performance function $Y = g(\boldsymbol{X})$, where $\boldsymbol{X}$ is the model input and Y is the output. The process is composed of three steps: sampling of input random variables, evaluation of the performance function for each sample, and statistical analysis on the model output.

Step 1: Sampling of input random variables

At the beginning, a random generator produces a sequence of numbers r_i inside the interval [0, 1]; this way, a uniform random variable R is created.

Subsequently, the samples of the [0, 1] uniform variables are transformed into values of a random variable X_i which follows the desired probability distribution $F_{x_i}(x_i)$ (e.g., a *standard normal distribution*).

This is accomplished by various methods; one of them is the *inverse transformation method*.

Through this technique, the values of the random variable X_i are given by

$$x_i = F_{x_i}^{-1}(r_i) \tag{3.4}$$

where $F_{x_i}^{-1}$ is the inverse of the cumulative distribution function (*cdf*) of the random variable X_i (from Du X., 2006).

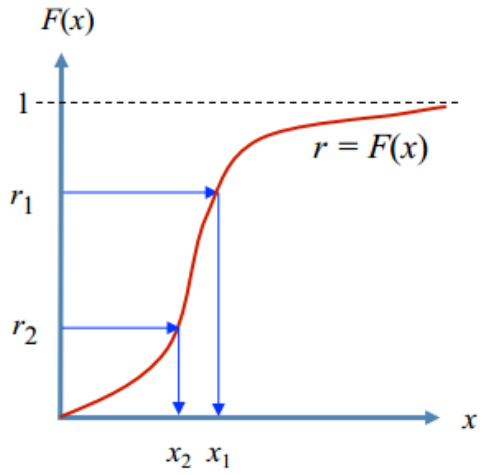

Figure 3.4: transformation of the samples from the [0, 1] uniform distribution to a nonuniform distribution (from Güneş, 2012).

Step 2: Numerical experimentation

Let us suppose that, for a particular random variable X_j (j = 1, 2..., n), N samples are generated; hence, the performance function will be computed for each of the samples:

$$y_{i,j} = g(x_{i,j}), \qquad i = 1,2,...,N \tag{3.5}$$

thus, N output samples are generated.

Step 3: statistical analysis on the model output

For the *j-th* random variable, Each output sample $y_{i,j} = g(x_{i,j})$ is computed, and is compared to the threshold value $y = g(X_{i,j}) = 0$.

If N_f is the total number of items such that $y < 0$, the probability of failure is given by

$$p_f = \frac{N_f}{N} \tag{3.6}$$

where N is the total number of samples.

Hence, the reliability is given by

$$R = 1 - p_f = 1 - \frac{N_f}{N} \tag{3.7}$$

3.3. First and Second Order Reliability Methods

These techniques are *approximation methods*, the aim of which is to determine, with an acceptable level of accuracy, the numerical value of a system reliability, without the need to analytically solve the integral

$$R = \int_{g(\boldsymbol{X})\geq 0} f_X(\boldsymbol{X})\, d\boldsymbol{X} \tag{3.8}$$

Eq. (3.8) corresponds to compute the portion of the volume under the *joint pdf* which lies in the safe region (i.e., $g(\boldsymbol{X}) \geq 0$, see Figure 3.5).

On the other hand, the probability of failure, which is expressed by

$$p_f = \int_{g(\boldsymbol{X})<0} f_X(\boldsymbol{X})\, d\boldsymbol{X} \tag{3.9}$$

corresponds to the volume of the removed part of the *joint pdf* $f_X(\boldsymbol{X})$ in Figure 3.5. In the same figure, the contours of the integrand $f_X(\boldsymbol{X})$ are shown as projected in the $\boldsymbol{X}$ plane.

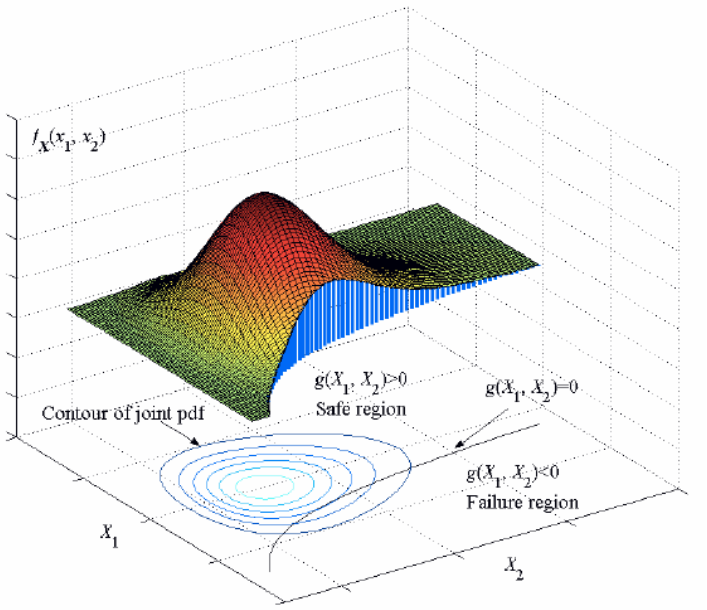

Figure 3.5: the total volume under the *joint pdf* is 1; hence, *reliability* is the portion of such volume which lies in the safe region (from Du X., 2006).

These methods are used in order to ease the computational difficulties and to reduce the computational effort which is required for a complex, multi-dimensional problem. This is done in two phases: the first one consists of simplifying the integrand $f_X(\boldsymbol{X})$, in order to make its contours more regular and symmetric; then, as a second step, the integration boundary $g(\boldsymbol{X}) = 0$ is simplified (Du X., 2006). These two steps allow to provide a simple analytical solution for the probability integration. There are two algorithms for doing this, which differ in the way the probability integration is approximated: the First Order Reliability Method (FORM) and the Second Order Reliability Method (SORM).

3.3.1. First Order Reliability Method (FORM)

Through this technique, the performance function $g(\boldsymbol{X})$ is approximated by the first order Taylor expansion, hence the name of the method.

First phase: simplification of the integral

In order to obtain such a simplification, the random variables $\boldsymbol{X} = (X_1, X_2, \dots, X_n)$ which are involved in the problem are transformed into standard normal variables $\boldsymbol{U} = (U_1, U_2, \dots, U_n)$, i.e., random variables which follow a standard normal distribution. This can be done by the *Rosenblatt Transformation*, which is based on the condition that the cumulative distribution function remains the same before and after the transformation, i.e.,

$$F_{X_i}(x_i) = \Phi(u_i) \tag{3.10}$$

where $\Phi(u_i)$ is the cumulative distribution function (*cdf*) of the standard normal distribution.

As for the random variables, the same formulation will be herein used for standard normal variables: U_i generically identifies the continuous variable and its axis on a coordinate system, whereas u_i is associated to a particular (discrete) value assumed by the variable along the axis.

It is useful to recall [from Eq. (2.12)] that the relationship between a normal random variable *X* and a standard normal variable *U* is given by the following expression:

$$U = \frac{X - \mu_X}{\sigma_X} \tag{3.11}$$

After such a transformation, Eq. (3.9) becomes

$$p_f = \int_{g(\boldsymbol{U})<0} \Phi_{\boldsymbol{U}}(\boldsymbol{U})\, d\boldsymbol{U} \tag{3.12}$$

being $\Phi_{\boldsymbol{U}}(\boldsymbol{U})$ the *joint pdf* of $\boldsymbol{U}$. Recalling that all the random variables are assumed to be independent, the resulting *joint pdf* is equal to the product of every single *pdf* of its respective standard normal distribution, thus resulting

$$\Phi_{\boldsymbol{U}}(\boldsymbol{U}) = \prod_{i=1}^{n} \frac{1}{\sqrt{2\pi}} \exp\left(-\frac{1}{2} u_i^2\right) \tag{3.13}$$

Therefore, the probability integration becomes

$$p_f = \int_{g(u_1,u_2,\ldots,u_n)<0} \int \prod_{i=1}^{n} \frac{1}{\sqrt{2\pi}} \exp\left(-\frac{1}{2} u_i^2\right) du_1\, du_2 \ldots du_n \tag{3.14}$$

The transformation does not affect the precision of the integration, i.e., equations (3.3) and (3.14) give the same result. Nevertheless, the contours of the integrand $\Phi_{\boldsymbol{U}}(\boldsymbol{U})$ become concentric circles (or hyperspheres, for a bigger dimensional problem; see Fig. 3.6): this makes the *pdf* $\boldsymbol{U}$ easier to be integrated.

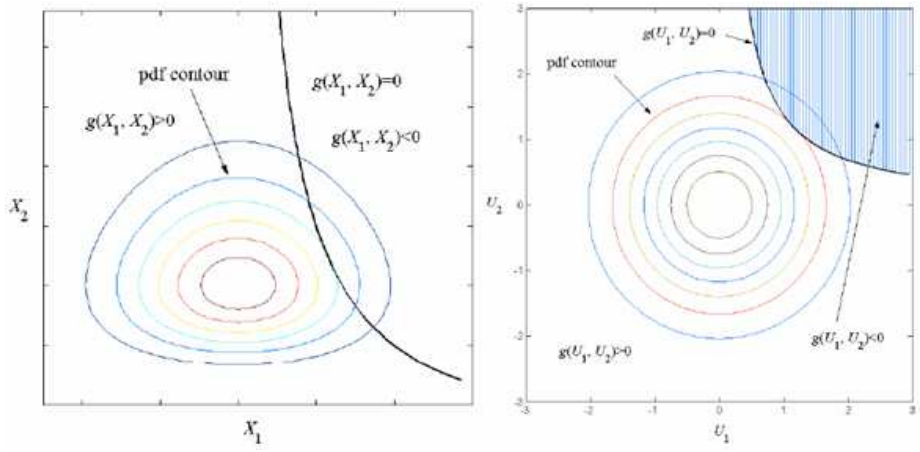

Figure 3.6: probability integration in the random variable space before and after the Transformation from random variable space $\boldsymbol{X}$ to standard normal space $\boldsymbol{U}$ (from Du X., 2006).

Second phase: approximating the integration boundary

As previously stated, in FORM the performance function $g(\boldsymbol{U})$ is approximated by the first order Taylor expansion:

$$G(\boldsymbol{U}) \approx L(\boldsymbol{U}) = g(\boldsymbol{u}^*) + \nabla g(\boldsymbol{u}^*)(\boldsymbol{U} - \boldsymbol{u}^*)^T \quad (3.15)$$

where $L(\boldsymbol{U})$ is the linearized performance function, $\boldsymbol{u}^*$ is the expansion point, T stands for a transpose, and $\nabla g(\boldsymbol{u}^*)$ is the gradient of $g(\boldsymbol{U})$ at $\boldsymbol{u}^*$ (D. Xiaoping, 2006).

In order to minimize the accuracy loss, Hasofer and Lind (1974) suggested to expand the performance function on its boundary $g(\boldsymbol{U}) = 0$ and, to be more precise, at the point having the maximum value of the *joint pdf*: this is called the *Most Probable Point* (MPP) (see Fig. 3.7).

The analytical expression for locating the MPP is given below:

$$\begin{cases} \max_{\boldsymbol{U}} \prod_{i=1}^{n} \frac{1}{\sqrt{2\pi}} \exp\left(-\frac{1}{2} u_i^2\right) \\ g(\boldsymbol{U}) = 0 \end{cases} \quad (3.16)$$

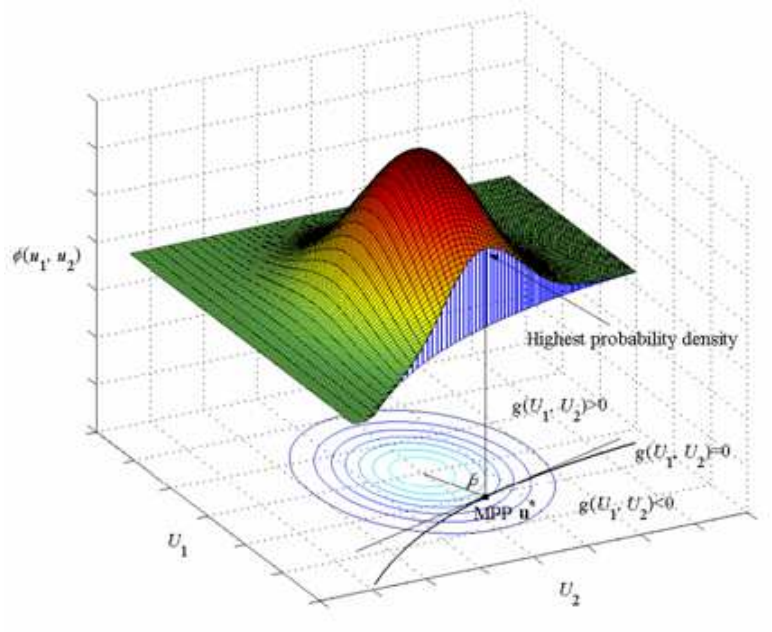

Figure 3.7: the most probable point corresponds to the highest probability density along the limit-state function $g(\boldsymbol{U}) = 0$ (from Du X., 2006).

Since

$$\prod_{i=1}^{n} \frac{1}{\sqrt{2\pi}} \exp\left(-\frac{1}{2} u_i^2\right) = \frac{1}{\sqrt{2\pi}} \exp\left(-\frac{1}{2} \sum_{i=1}^{n} u_i^2\right), \quad (3.17)$$

we see that the maximum value of $\prod_{i=1}^{n} \frac{1}{\sqrt{2\pi}} \exp\left(-\frac{1}{2} u_i^2\right)$ corresponds to the minimum of $\sum_{i=1}^{n} u_i^2$. Hence, Eq. (3.16) can be rewritten as

$$\begin{cases} \min_{\boldsymbol{U}} \|\boldsymbol{u}\| \\ g(\boldsymbol{U}) = 0 \end{cases} \tag{3.18}$$

whereof solution is the Most Probable Point, which is indicated as $\boldsymbol{u}^* = (u_1^*, u_2^*, \dots, u_n^*)$. As shown in Fig. 3.8, the MPP is the shortest distance point of the limit state function $g(\boldsymbol{U})$=0 to the origin $\boldsymbol{O}$ in $\boldsymbol{U}$-space. Such a minimum distance was called *reliability index* β (Hasofer and Lind, 1974), and is such that $\beta = \|\boldsymbol{u}^*\|$. As it will be seen shortly, the knowledge of the shortest distance can be used to predict the probability of the limit-state function less than zero (Du X. *et al.*, 2000).

At the Most Probable Point, g($\boldsymbol{U}$) = 0, so eq. (3.15) becomes

$$L(\boldsymbol{U}) = \sum_{i=1}^{n} \left.\frac{\partial g(\boldsymbol{U})}{\partial U_i}\right|_{\boldsymbol{u}^*} (U_i - u_i^*) \tag{3.19}$$

Naming a_0 and a_1 the following coefficients:

$$a_0 = -\sum_{i=1}^{n} \left.\frac{\partial g(\boldsymbol{U})}{\partial U_i}\right|_{\boldsymbol{u}^*} u_i^* \tag{3.20}$$

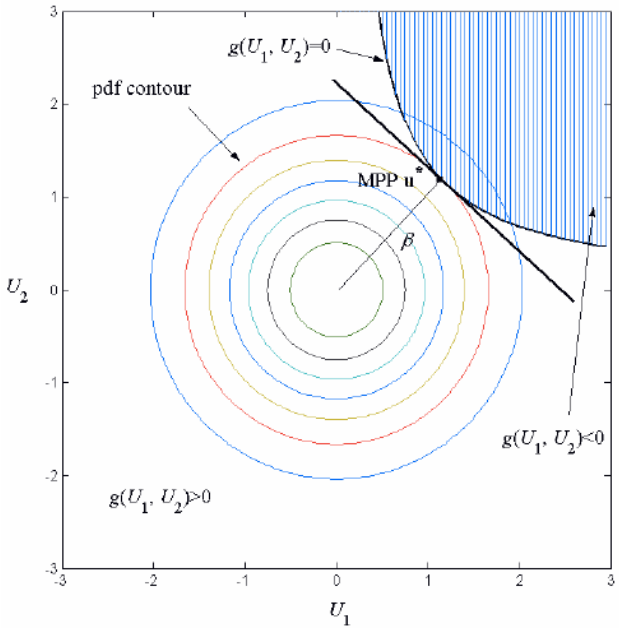

Figure 3.8: The *Most Probable Point* (MPP) as seen in the $\boldsymbol{U}$-space. As it can be seen, this is the closest point of the limit-state function $g(\boldsymbol{U}) = 0$ to the origin of the $\boldsymbol{U}$-space (from Du X., 2006).

and

$$a_i = \left.\frac{\partial g(\boldsymbol{U})}{\partial U_i}\right|_{\boldsymbol{u}^*}, \tag{3.21}$$

equation (3.19) may be rewritten as

$$L(\boldsymbol{U}) = a_0 + \sum_{I=1}^{n} a_i U_i \tag{3.22}$$

Hence, *L(**U**)* is a linear function of standard normal variables; therefore, *L(**U**)* has a normal distribution, too.

Its mean, μ_L, is equal to

$$\mu_L = a_0 = -\sum_{i=1}^{n} \frac{\partial g(\boldsymbol{U})}{\partial U_i}\Big|_{\boldsymbol{u}^*} u_i^* \tag{3.23}$$

while its standard deviation, σ_L, is

$$\sigma_L = \sqrt{\sum_{i=1}^{n} a_i^2} = \sqrt{\sum_{i=1}^{n} \left(\frac{\partial g}{\partial U_i}\Big|_{u_i^*}\right)^2} \tag{3.24}$$

Consequently, the probability of failure is given by

$$p_f \approx P\{L(\boldsymbol{U}) < 0\} = \Phi\left(-\frac{\mu_L}{\sigma_L}\right) = \Phi\left(\frac{\sum_{i=1}^{n} \frac{\partial g}{\partial U_i}\Big|_{\boldsymbol{u}^*}}{\sqrt{\sum_{i=1}^{n}\left(\frac{\partial g}{\partial U_i}\Big|_{\boldsymbol{u}^*}\right)^2}}\right) \tag{3.25}$$

Naming as α_i the following coefficients,

$$\alpha_i = \frac{\frac{\partial g}{\partial U_i}\Big|_{\boldsymbol{u}^*}}{\sqrt{\sum_{i=1}^{n}\left(\frac{\partial g}{\partial U_i}\Big|_{\boldsymbol{u}^*}\right)^2}} \tag{3.26}$$

the expression for the probability of failure becomes

$$p_f \approx P\{L(\boldsymbol{U}) < 0\} = \Phi\left(-\frac{\mu_L}{\sigma_L}\right) = \Phi\left(\frac{\sum_{i=1}^{n} \frac{\partial g}{\partial U_i}\Big|_{\boldsymbol{u}^*}}{\sqrt{\sum_{i=1}^{n}\left(\frac{\partial g}{\partial U_i}\Big|_{\boldsymbol{u}^*}\right)^2}}\right) = \Phi\left(\sum_{i=1}^{n} \alpha_i u_i^*\right) \tag{3.27}$$

From (3.21) and (3.26),

$$\boldsymbol{a} = (\alpha_1, \alpha_2, \dots, \alpha_n) = \frac{\nabla g(\boldsymbol{u}^*)}{\|\nabla g(\boldsymbol{u}^*)\|} \tag{3.28}$$

which is the unit vector of the gradient of the performance function *g(**U**)* at the MPP.

Thus, the probability of failure can also be written as

$$p_f \approx \Phi\left(\sum_{i=1}^{n} \alpha_i u_i^*\right) = \Phi\left(\sum_{i=1}^{n} \boldsymbol{\alpha u}^{*\boldsymbol{T}}\right) \tag{3.29}$$

Since the MPP is the shortest distance point from the performance function curve *g(**U**)=0* to the origin, the MPP is the point of tangency of the curve *g(**U**)=0* and the circle (centred at the origin) with a radius equal to β (figure 3.9). Consequently, the MPP vector results to be perpendicular to the performance function curve at the MPP. The direction of this vector is expressed by the unit vector $u^*/\|u^*\| = u^*/\beta$. On the other hand, the direction of the gradient is also perpendicular to the curve at the MPP, and its direction can be represented by the unit vector $\boldsymbol{a}$ (see Eq. (3.28)) (Du X., 2006).

Hence,

$$\frac{\boldsymbol{u}^*}{\beta} = -\boldsymbol{a} \tag{3.30}$$

or,

$$\boldsymbol{u}^* = -\beta\boldsymbol{a} \tag{3.31}$$

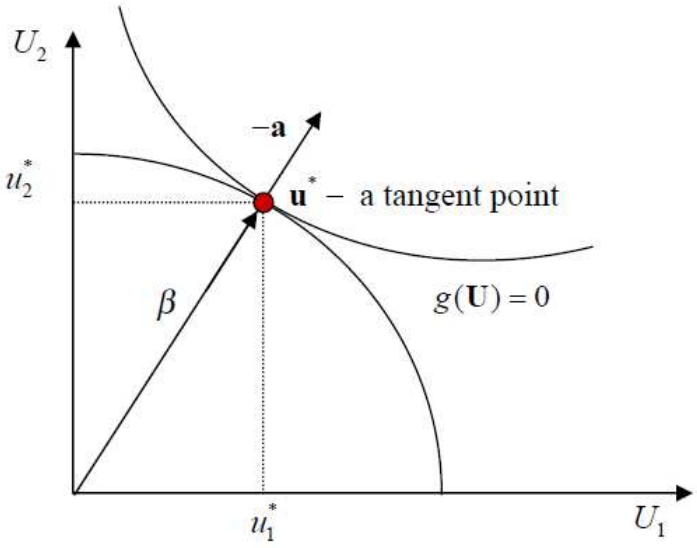

Figure 3.9: geometrical situation of the Most Probable Point $\boldsymbol{u}^*$ (from Du X., 2006).

If one recalls that

$$\boldsymbol{a}\boldsymbol{a}^{\boldsymbol{T}} = \sum_{i=1}^{n} \alpha_i^2 = 1 \tag{3.32}$$

the probability of failure is eventually expressed as

$$p_f = P\{L(\boldsymbol{U}) < 0\} = \Phi(\boldsymbol{a}\boldsymbol{u}^{*\boldsymbol{T}}) = \Phi(-\beta\boldsymbol{a}\boldsymbol{a}^{*\boldsymbol{T}}) = \Phi(-\beta) \tag{3.33}$$

Therefore, the reliability is

$$R = 1 - p_f = 1 - \Phi(-\beta) = \Phi(\beta) \tag{3.34}$$

MPP search

From Eq. (3.33), the evaluation of the probability of failure is possible once the reliability index β has been obtained. The latter can in turn be determined once the MPP has been located. However, the MPP search is often impossible to be performed analytically. Such an issue can be overcome by using numerical methods. One of them is described in the sequel, which is a recursive algorithm where the performance function is linearized. Throughout the iterations, the position of the MPP is updated, until its actual location is obtained.

Let $\boldsymbol{u^k}$ be the MPP coordinates at the *k-th* iteration (see Fig. 3.10); the performance function is linearized in such a point, and is expressed as

$$g(\boldsymbol{u}) = g(\boldsymbol{u^k}) + \nabla g(\boldsymbol{u^k})(\boldsymbol{u} - \boldsymbol{u^k})^T \tag{3.35}$$

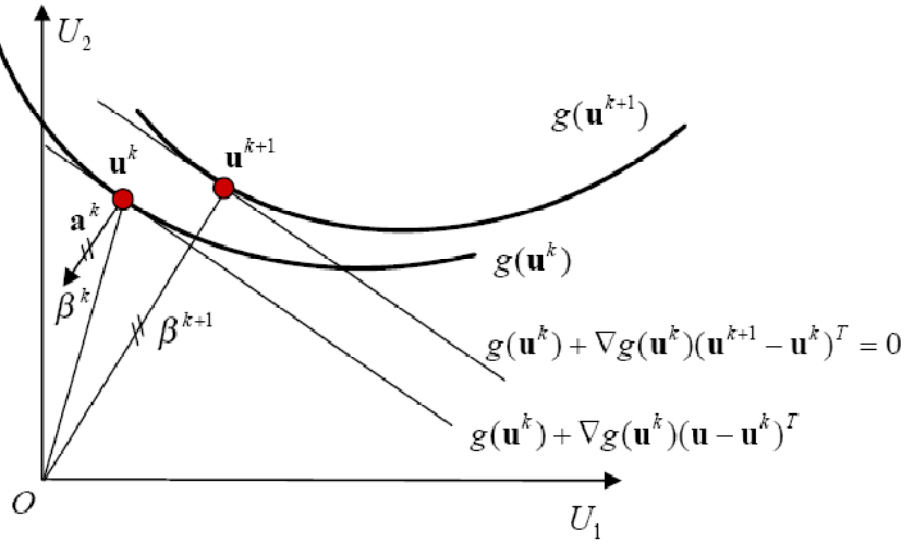

Figure 3.10: MPP search scheme (from Du X., 2006).

Let the linearized function $g(\boldsymbol{u^k})$ be zero; consequently, in the following iteration, the MPP $\boldsymbol{u^{k+1}}$ will lie on the line (the linearized performance function, see Fig. 3.10), i.e,

$$g(\boldsymbol{u^{k+1}}) = g(\boldsymbol{u^k}) + \nabla g(\boldsymbol{u^k})(\boldsymbol{u^{k+1}} - \boldsymbol{u^k})^T = 0 \tag{3.36}$$

From equation (3.31), one deduces that, at the *k-th* iteration,

$$\boldsymbol{u^k} = -\beta^k \boldsymbol{a^k} \tag{3.37}$$

$\boldsymbol{u^{k+1}}$ is the shortest distance point from the origin to the line, as depicted in Fig. 3.10. Hence, the vector $\boldsymbol{u^{k+1}}$ is perpendicular to the line and is directed from the origin $\boldsymbol{O}$ to $\boldsymbol{u^{k+1}}$ (from Du X., 2006).

The versor $\boldsymbol{a^{k+1}}$ is also perpendicular to the line, and its direction is opposite to that of $\boldsymbol{u^{k+1}}$. Since the length of the vector $\boldsymbol{u^{k+1}}$ corresponds to the Euclidean distance from the origin $\boldsymbol{O}$ to the point $\boldsymbol{u^{k+1}}$ (i.e., the reliability index β), it follows that

$$\boldsymbol{u^{k+1}} = -\beta^{k+1}\boldsymbol{a^k} \tag{3.38}$$

Substituting $\boldsymbol{u^k}$ in equation (3.37) and $\boldsymbol{u^{k+1}}$in equation (3.38) into equation (3.36), one obtains

$$g(\boldsymbol{u^{k+1}}) = g(\boldsymbol{u^k}) + \nabla g(\boldsymbol{u^k})(\boldsymbol{a^k})(\beta^k - \beta^{k+1}) = g(\boldsymbol{u^k}) + \|\nabla g(\boldsymbol{u^k})\|(\beta^k - \beta^{k+1}) = 0 \tag{3.39}$$

The updated reliability index is then

$$\beta^{k+1} = \beta^k + \frac{g(\boldsymbol{u^k})}{\|\nabla g(\boldsymbol{u^k})\|} \tag{3.40}$$

whose corresponding updated point is

$$\boldsymbol{u^{k+1}} = -\boldsymbol{a^k}\left[\beta^k + \frac{g(\boldsymbol{u^k})}{\|\nabla g(\boldsymbol{u^k})\|}\right] \tag{3.41}$$

Equations (3.40) and (3.41) are recursive formulae, which can be used to locate the MPP and determine the corresponding reliability index. A starting point is required, and the origin $\boldsymbol{u^0} = \boldsymbol{0}$ is often chosen.

The termination criterion of the MPP search is one of the following:

1) if $\|\boldsymbol{u^{k+1}} - \boldsymbol{u^k}\| \leq \varepsilon_1$, stop; or
2) if $\|\nabla g(\boldsymbol{u^{k+1}}) - \nabla g(\boldsymbol{u^k})\| \leq \varepsilon_2$, stop; or
3) if $\|\boldsymbol{\beta^{k+1}} - \boldsymbol{\beta^k}\| \leq \varepsilon_3$, stop.

Where ε_1, ε_2, ε_3 are very small positive numbers, according to the desired precision level.

Figure 3.11 depicts the flowchart of the MPP search algorithm that has been presented.

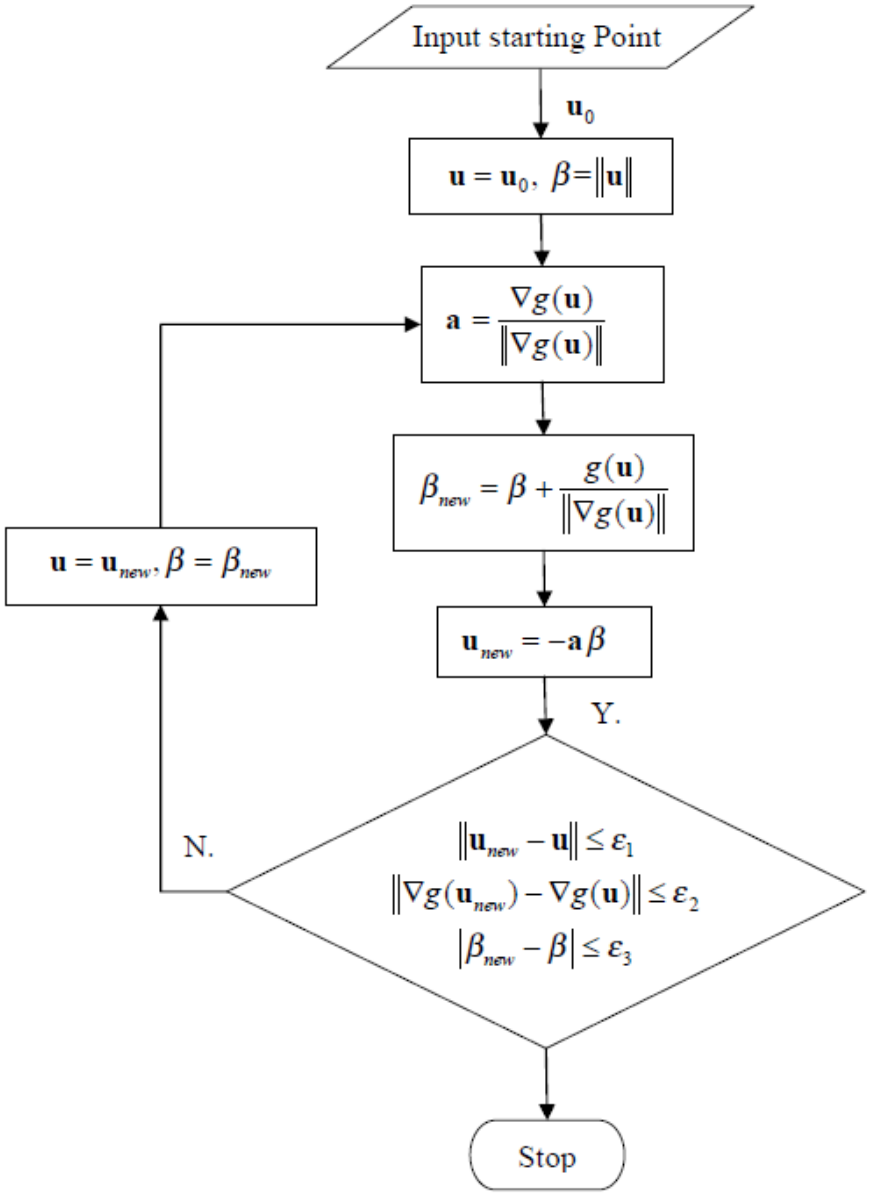

Figure 3.11: flowchart of the recursive MPP search (from Du X., 2006).

3.3.2. Second Order Reliability Method (SORM)

The First Order Reliability Method (FORM) often provides a sufficient precision in the determination of the probability of failure. However, in some cases, the limit-state function in the *U*-space may be highly nonlinear, and the variance range of uncertain variables could be wide. In such cases, the first order approximation of the limit-state function may no longer be adequate, thus resulting in a large error in the reliability estimation. The second-order reliability method (SORM) was established as an attempt to improve the accuracy of FORM (Zhao et al, 1999); through this algorithm, the limit-state function is approximated at the second term of the Taylor expansion at the MPP (Breitung K., 1984). The SORM method is generally more accurate than the FORM, but it is also more computationally demanding; indeed, it requires the determination of the second derivatives of the performance function.

After the random variables $\boldsymbol{X}$ have been transformed into standard normal variables $\boldsymbol{U}$, the performance function $g(\boldsymbol{U})$ is approximated by the second order Taylor expansion at the MPP.

The second order approximation gives

$$g(\boldsymbol{U}) \approx g(\boldsymbol{u}^*) + \sum_{i=1}^{n} \left.\frac{\partial g}{\partial U_i}\right|_{\boldsymbol{u}^*} (U_i - u_i^*) + \frac{1}{2}\sum_{i=1}^{n}\sum_{j=1}^{n} \left.\frac{\partial^2 g}{\partial U_i \partial U_j}\right|_{\boldsymbol{u}^*} (U_i - u_i^*)\left(U_j - u_j^*\right) \qquad (3.42)$$

Assuming that $g(\boldsymbol{u}^*) = 0$ and writing Eq. (3.42) with a vectorial notation, one obtains

$$g(\boldsymbol{U}) \approx \nabla g(\boldsymbol{u}^*)(\boldsymbol{U} - \boldsymbol{u}^*)^T + \frac{1}{2}(\boldsymbol{U} - \boldsymbol{u}^*)\nabla^2 g(\boldsymbol{u}^*)(\boldsymbol{U} - \boldsymbol{u}^*)^T \qquad (3.43)$$

being $\nabla^2 g$ the Hessian matrix, i.e.,

$$\nabla^2 g = \begin{bmatrix} \frac{\partial^2 g}{\partial^2 U_1} & \cdots & \frac{\partial^2 g}{\partial U_1 \partial U_n} \\ \vdots & \ddots & \vdots \\ \frac{\partial^2 g}{\partial U_n \partial U_1} & \cdots & \frac{\partial^2 g}{\partial^2 U_n} \end{bmatrix} \qquad (3.44)$$

In order to determine the probability of failure, Eq. (3.43) has to be simplified once again, due to the second order terms. After linear and orthogonal transformations, $g(\boldsymbol{U})$ becomes a function of *independent and* standard normal variables. Then, following Breitung's formulation (1984), the probability of failure is eventually expressed as

$$p_f = \Phi(-\beta)\prod_{i=1}^{n-1}(1 + \beta k_i)^{-\frac{1}{2}} \qquad (3.45)$$

where β is the reliability index and k_i (i = 1, 2, …, n-1) are the principal curvatures of $g(\boldsymbol{U})$ at the MPP (Du X., 2010). By comparison to Eq. (3.33), one can conclude that $\prod_{i=1}^{n-1}(1 + \beta k_i)^{-\frac{1}{2}}$ is a corrective term which allows to pass from the First Order Reliability Method (FORM) to the Second Order Reliability Method (SORM).

In order to compute the p_f through Eq. (3.45), the values of k_i (i = 1, 2, …, n-1) at the MPP are needed. Such principal curvatures are the eigenvalues of a matrix **A**, whose elements a_{ij} are

$$a_{ij} = \frac{\left(\boldsymbol{R}\nabla^2 g(\boldsymbol{u}^*)\boldsymbol{R}^T\right)_{ij}}{\|\nabla g(\boldsymbol{u}^*)\|} \qquad (3.46)$$

here, $\boldsymbol{R}$ is a $n \times n$ rotation matrix, which, in turn, is attained by applying Gram-Schmidt orthogonalization to another matrix $\boldsymbol{R_0}$.

$\boldsymbol{R_0}$ is given by

$$\boldsymbol{R_0} = \begin{bmatrix} 1 & 0 & \cdots & 0 & 0 \\ 0 & 1 & & 0 & 0 \\ \vdots & & \ddots & \vdots & \\ 0 & 0 & \cdots & 1 & 0 \\ -\alpha_1 & -\alpha_2 & & -\alpha_{n-1} & -\alpha_n \end{bmatrix} \qquad (3.47)$$

where the (n-1) x (n-1) minor is an identity matrix, whereas the last row of $\boldsymbol{R_0}$ is the unit vector $\boldsymbol{-a}$ that was defined in equation (3.28).

SORM method is composed by the two following steps:

1. **MPP search.** This procedure is exactly the same as in FORM. After the determination of $\boldsymbol{u}^*$, the corresponding values of β, $a(\boldsymbol{u}^*)$, $\nabla g(\boldsymbol{u}^*)$, and $\nabla^2 g(\boldsymbol{u}^*)$ are found.
2. **Determination of matrix $\boldsymbol{R}$.** Let us indicate with r_{0i} and r_0 the rows of matrices $\boldsymbol{R_0}$ and $\boldsymbol{R}$, respectively. $\boldsymbol{R_0}$ can be used to get $\boldsymbol{R}$ through the Gram-Schmidt orthogonalization procedure, as follows:

$$\begin{cases} \boldsymbol{r_n = r_{0n}} \\ \boldsymbol{r'_k = r_{0k} - \sum_{j=k+1}^{n} \frac{r_j r_{0k}^T}{r_j r_j^T} r_j}, \qquad \boldsymbol{r_k = \frac{r_k^i}{\|r_k^i\|}}, \qquad k = n-1, n-2, \dots, 1. \end{cases} \tag{3.48}$$

3. **Construction of matrix A.** Equation (3.46) leads to the determination of matrix **A**, whose dimensions are (n-1) x (n-1).

4. **Computation of the principal curvatures.** The k_i are attained through the solution of the following eigenvalue problem:

$$\mathbf{A}\boldsymbol{Z} = k\boldsymbol{Z} \tag{3.49}$$

where $\boldsymbol{Z}$ is a vector with *n-1* elements. The problem is solved by putting the following condition:

$$det(\mathbf{A} - k\boldsymbol{I}) = 0 \tag{3.50}$$

where *det* stands for *determinant* and $\boldsymbol{I}$ is the (n-1) x (n-1)-dimensional identity matrix.

5. **Computation of the probability of failure.** SORM approximates the limit state surface in *U*-space at the MPP by a second-order surface [Fiessler *et al*, 1979]. In Figure 3.12, a graphical comparison between FORM and SORM is depicted. As it can be seen, for a nonlinear limit-state function, the SORM is generally more accurate then FORM. However, its accuracy is guaranteed only for those cases in which the reliability index β is sufficiently large (Du X. et al., 2010). Since SORM requires the computation of the second order derivatives for the performance function, it is not as efficient as FORM when the derivatives are evaluated numerically (Du X., 2006).

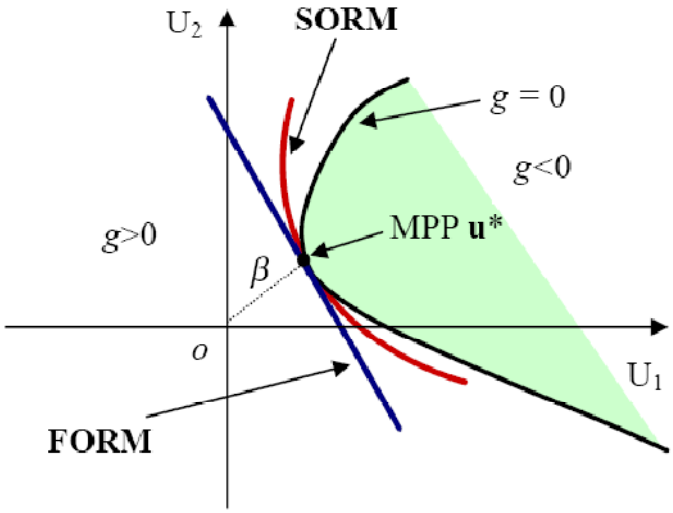

Figure 3.12: Comparison between FORM and SORM (from Du X., 2006).

3.3.3. Inverse reliability analysis

In many engineering applications, it is worthwhile to design a system with a previously settled reliability level, rather than computing the probability of failure a posteriori. For this purpose, *inverse reliability analysis* is used, which consists of determining the performance function that corresponds to the desired reliability R or probability of failure p_f. It may be convenient to work with *percentile values*; this way, the goal is to find the percentile value g^{p_f} which corresponds to the target p_f, i.e.,

$$Pr[g(\boldsymbol{X}) \leq g^{p_f}] = p_f \tag{3.51}$$

The latter equation means that the probability, for the performance function, to be below g^{p_f} is equal to p_f.

In order to determine the g^{p_f}, the inverse FORM method (*iFORM*) can be applied; a brief introduction to this technique is given below.

Let us define a new performance function, such that

$$g'(\boldsymbol{X}) = g(\boldsymbol{X}) - g^{p_f} \tag{3.52}$$

that, after Rosenblatt's transformation, becomes

$$g'(\boldsymbol{U}) = g(\boldsymbol{U}) - g^{p_f} \tag{3.53}$$

From the corresponding limit-state function, i.e.,

$$g'(\boldsymbol{U}) = g(\boldsymbol{U}) - g^{p_f} = 0, \tag{3.54}$$

Let $\boldsymbol{u}^*$ be the MPP for $g'(\boldsymbol{U}) = 0$; hence, $\boldsymbol{u}^*$ is also the MPP for $g'(\boldsymbol{U}) \leq 0$, i.e., for $g(\boldsymbol{U}) \leq g^{p_f}$. From the target probability of failure p_f, the corresponding reliability index β is given by

$$\beta = \left|\Phi^{-1}(p_f)\right| \tag{3.55}$$

The Most Probable Point (MPP) $\boldsymbol{u}^*$ is the point of tangency of both the circle having radius β and the limit-state function $g'(\boldsymbol{U}) = g(\boldsymbol{U}) - g^{p_f} = 0$ (see Fig. 3.13). Moreover, $\boldsymbol{u}^*$ is also the point having the minimum value of $g(\boldsymbol{U})$ on the circle; that point corresponds to the maximum probability of failure, i.e., p_f. Therefore, the aim of the inverse FORM is to find the MPP $\boldsymbol{u}^*$ on the β-circle (or β-sphere, or β-hypersphere, for an higher dimensional problem (Du X., 2006)) such that the performance function $g(\boldsymbol{U})$ is minimized:

$$\begin{cases} find\ u \\ s.t. \\ \min g\ (U) \\ \|u\| = \beta \end{cases} \tag{3.56}$$

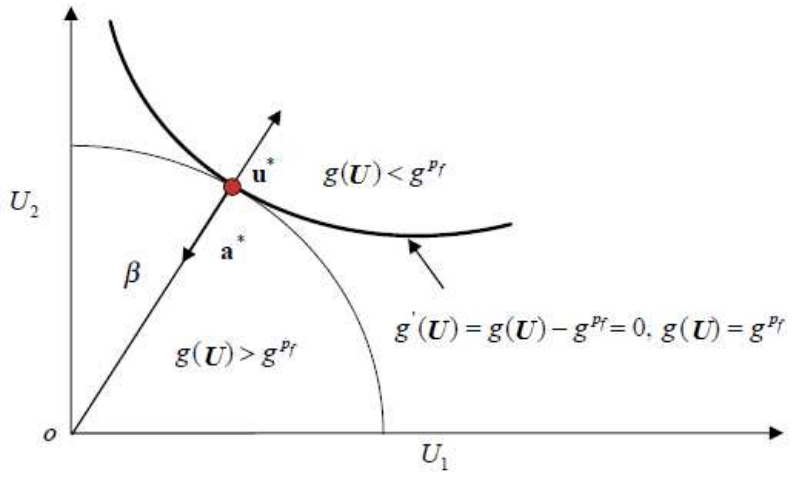

Figure 3.13: scheme of the inverse search for the Most Probable Point (MPP).

Once the MPP $\boldsymbol{u}^*$ has been found, the p_f-percentile value g^{p_f} is computed at that point, i.e.,

$$g^{p_f} = g(\boldsymbol{u}^*) \tag{3.57}$$

3.4. A basic structural example

The example that is now presented will be solved by following the different methods which have been seen in sections 3.2 ad 3.3; this will result in a useful comparison of the various approaches.

Let us consider a statically indeterminate structure, composed of a horizontal beam and a soft vertical support over its right tip, represented as a spring; such a structure, which experiences a vertical force *F*, is subject to some uncertainties; therefore, we are interested on assessing its reliability.

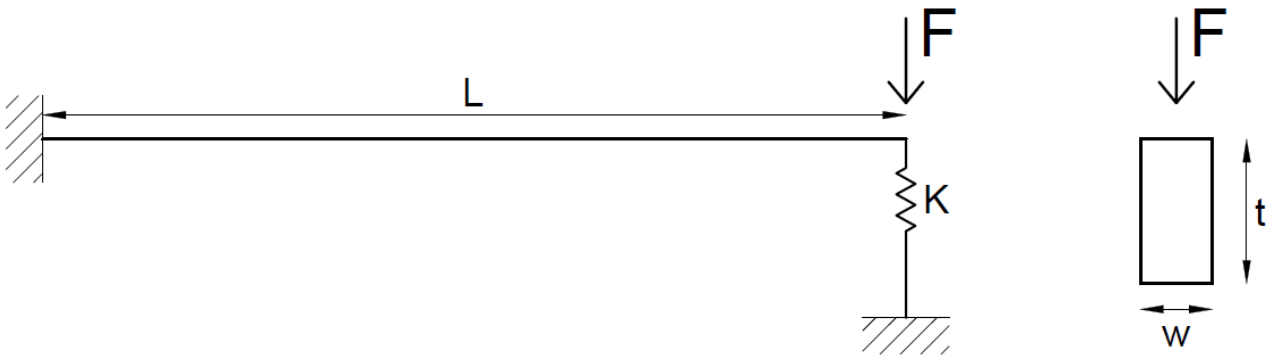

Figure 3.14: statically indeterminate structure.

The data of the problem are the following:

Geometrical features (see Fig. 3.14): L = 300 mm; t = 20 mm; w = 10 mm;

acting force (see Fig. 3.14): F = 1500 N;

Young Modulus: E = 71700 N/ mm^2 (Nominal value) - Material: Al 7075-T6 (from www.matweb.com);

Beam section moment of inertia with respect to the *w* direction: I = 6667 mm^4 (Nominal value);

δ = vertical displacement of the point where the force F is acting.

Two physical quantities are non-deterministic, and follow a standard normal distribution:

-Bending stiffness of the horizontal beam: R_f = E*I.

$$R_f \approx \mathrm{N}\,(478*10^6, 95.6*10^6)\ \mathrm{N}*mm^2$$

-Compressive stiffness of the spring: K ≈ N (40, 8) $\frac{N}{mm}$.

Using the flexibility method, the expression of the vertical displacement δ is found to be

$$\delta = \frac{F*l^3}{3*R_f + K*l^3} \tag{3.58}$$

As for the constraint, the vertical displacement δ has not to exceed a given value of, say, δ_0 =25 mm. Such a value would be overtaken if either the beam or the spring failed.

From equation (3.58), one can easily compute δ in these two extreme cases:

- without the spring: $\delta = \frac{F * l^3}{3 * R_f}$ = 28.24 mm > 25 mm;

- without the beam: $\delta = \frac{F}{K}$ = 37.5 mm > 25 mm.

The goal of this analysis is to assess the probability of failure of the structure, defined as the probability of the maximum allowable value of the tip displacement to be greater than the actual tip displacement, namely

$$p_f = P\left\{ g = \delta_0 - \frac{F * l^3}{3 * R_f + K * l^3} \geq 0 \right\} \tag{3.59}$$

3.4.1. Solving with MCS

Let us implement a simple computer program with Matlab®, to observe the progress of the outputs with an increasing number of simulations. Figures 3.15 to 3.18, that differ by the number of the samples, plot all the couples (R_f , K) that were sampled during the simulations.

It can be clearly seen that the probability of failure p_f gradually converges to a value of 0.006417 (0.6417 %); thus, the reliability R converges to about 99.3583 % .

R = 1 - $p_f \rightarrow$ 0.993583

The straight line in figures 3.15 to 3.18 represents the equation for g = 0, expressed as a function of the two variables R_f and K:

$$K = -\frac{1}{9 * 10^6} * R_f + 60$$

where $-\frac{1}{9 * 10^6}$ is the slope of the line.

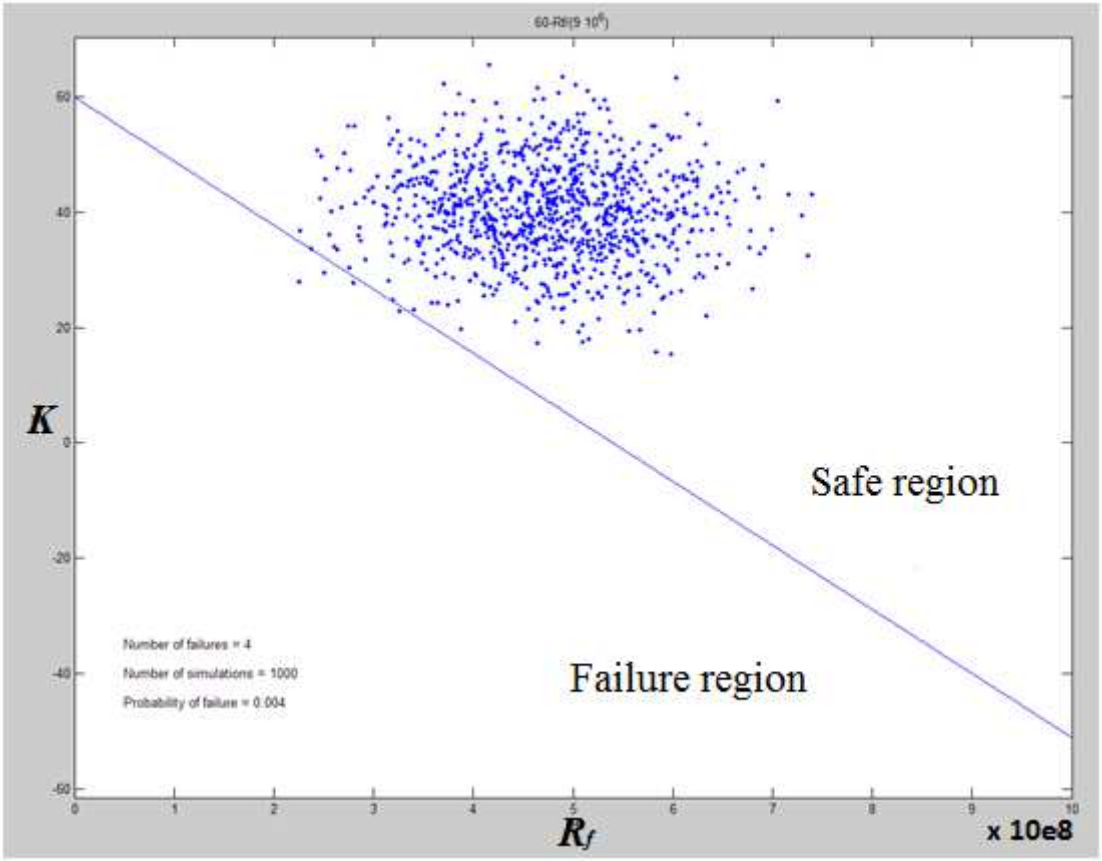

Figure 3.15: 10^3 simulations – probability of failure = 0.004.

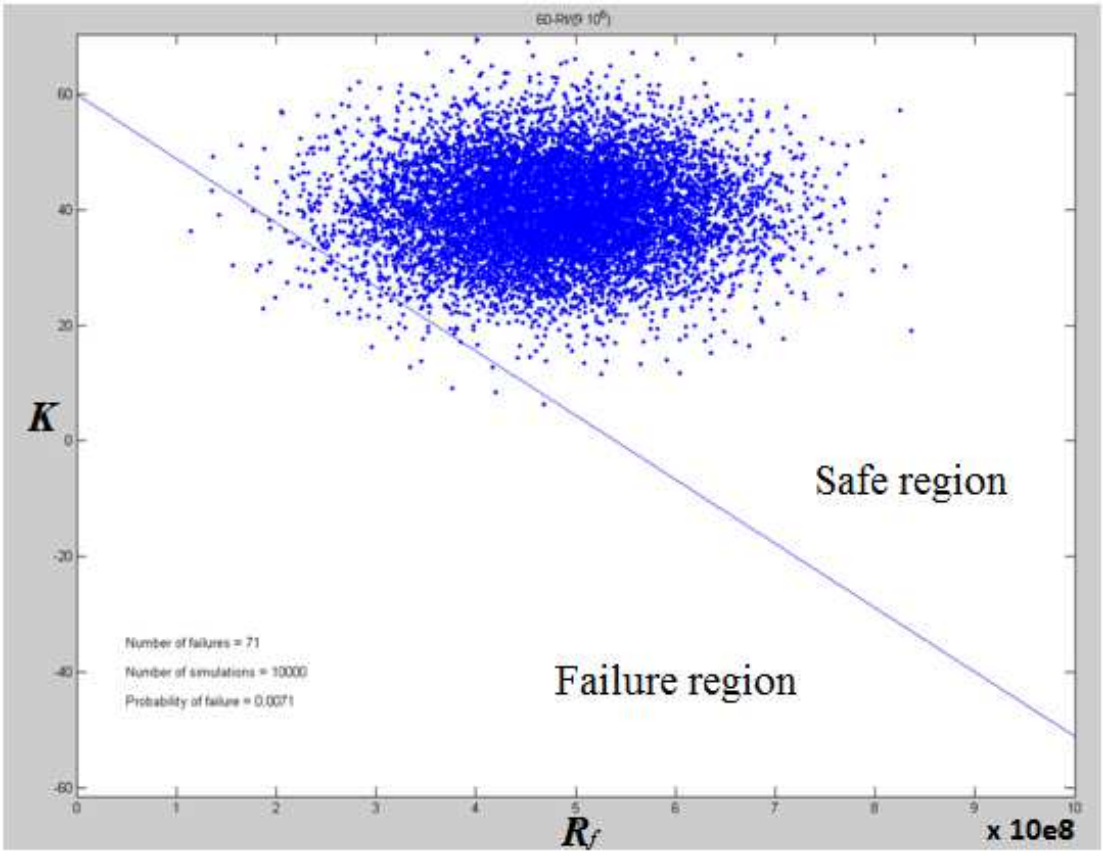

Figure 3.16: 10^4 simulations –probability of failure = 0.0071.

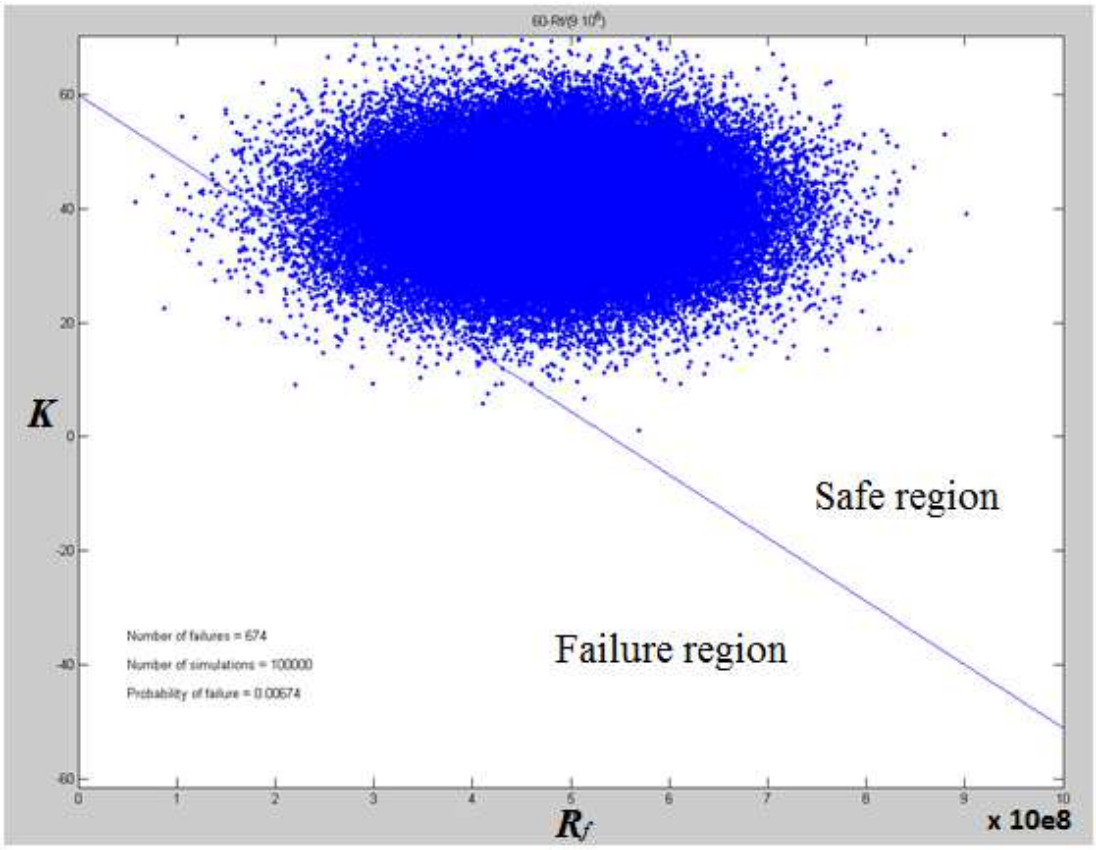

Figure 3.17: 10^5 simulations – probability of failure = 0.00674.

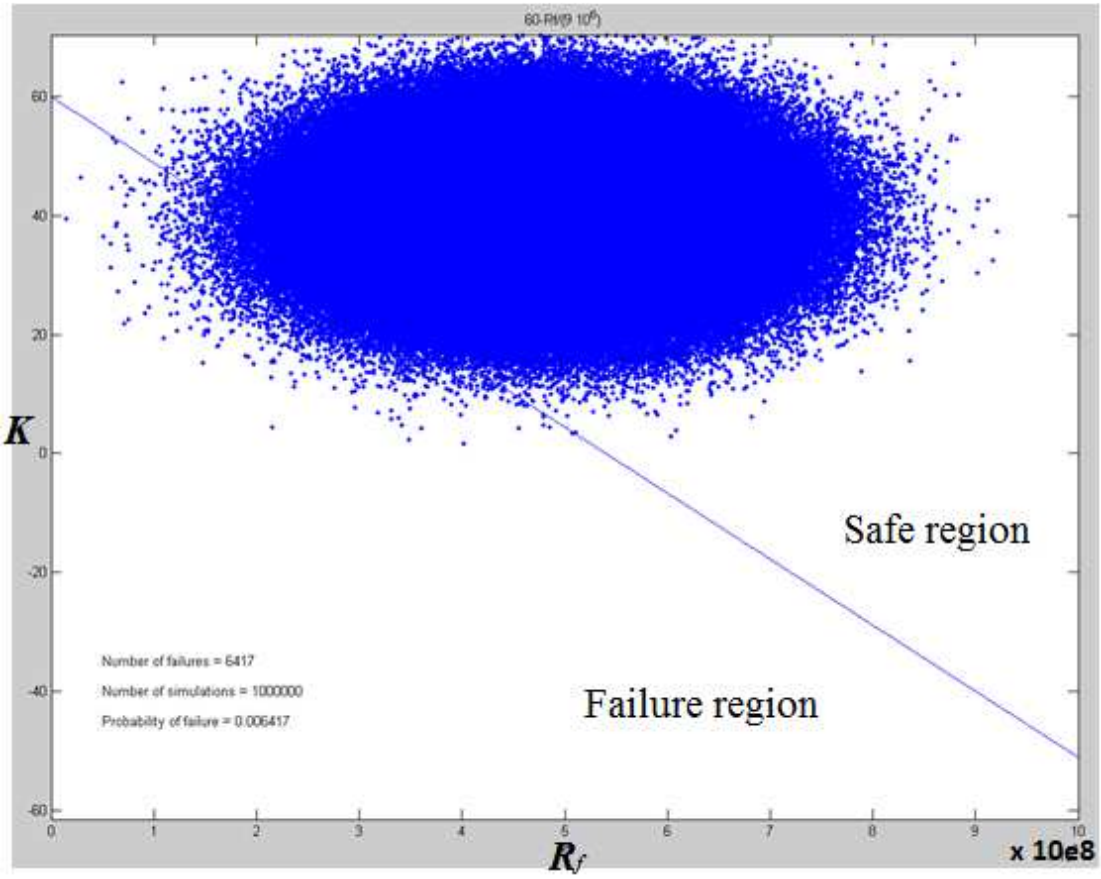

Figure 3.18: 10^6 simulations – probability of failure = 0.006417.

The accuracy of Monte Carlo Simulation depends on the number of simulations *N*. The higher the number of simulations, the more accurate the estimate will be. As the number of simulations *N* approaches infinity, the solution of Monte Carlo simulation will converge to the true probability that is under estimation. Monte Carlo is computationally robust: with a sufficient number of simulations, it always converges (Du X., 2006).

3.4.2. Solving with FORM

First, the normally distributed variables R_f and K are transformed into the standard normal variables:

$$\boldsymbol{X} = \left(R_f, K\right) = (\mu_R + \sigma_R U_R, \mu_K + \sigma_K U_K) \tag{3.60}$$

or

$$\boldsymbol{U} = (U_R, U_K) = \left(\frac{R_f - \mu_R}{\sigma_R}, \frac{K - \mu_K}{\sigma_K}\right) \tag{3.61}$$

The transformed performance function in the *U*-space becomes

$$g = \delta_0 - \frac{Pl^3}{[3(\mu_R + \sigma_R U_R) + (\mu_K + \sigma_K U_K) l^3]} \tag{3.62}$$

The gradient of g($\boldsymbol{U}$) is given by

$$\nabla g(\boldsymbol{U}) = \left(\frac{3\sigma_R P l^3}{[3(\mu_R + \sigma_R U_R) + (\mu_K + \sigma_K U_K) l^3]^2}, \frac{\sigma_K P l^6}{[3(\mu_R + \sigma_R U_R) + (\mu_K + \sigma_K U_K) l^3]^2}\right) \tag{3.63}$$

The starting point for the search of the Most Probable Point (MPP) is set to $\boldsymbol{u}^0 = (0, 0)$.

Iteration 1

At $\boldsymbol{u}^0 = (0, 0)$, $g(\boldsymbol{u}^0) = 8.8902$, $\nabla g(\boldsymbol{u}^0) = (1.838, 1.384)$,

$\|\nabla g(\boldsymbol{u}^0)\| = \sqrt{(-1.838)^2 + (-1.384)^2} = 2.301$,

$a^0 = \frac{\nabla g(\boldsymbol{u}^0)}{\|\nabla g(\boldsymbol{u}^0)\|} = (0.799, 0.601)$,

and $\beta^0 = \|\boldsymbol{u}^0\| = 0$

Iteration 2

$$\boldsymbol{u}^1 = -\boldsymbol{a}^0 \left\{\beta^0 + \frac{g(\boldsymbol{u}^0)}{\|\nabla g(\boldsymbol{u}^0)\|}\right\} = (-3.087, -2.322)$$

At $\boldsymbol{u}^1 = (-3.087, -2.322)$, $g(\boldsymbol{u}^1) = -10.93$, $\nabla g(\boldsymbol{u}^1) = (9.15, 6.89)$,

$\|\nabla g(\boldsymbol{u}^1)\| = 11.45$, $a^1 = \frac{\nabla g(\boldsymbol{u}^1)}{\|\nabla g(\boldsymbol{u}^1)\|} = (0.799, 0.602)$,

and $\beta^1 = \|\boldsymbol{u}^1\| = 3.863$

Iteration 3

$\boldsymbol{u}^2 = -\boldsymbol{a}^1 \left\{\beta^1 + \frac{g(\boldsymbol{u}^1)}{\|\nabla g(\boldsymbol{u}^1)\|}\right\} = (-2.33, -1.75)$,

At $\boldsymbol{u}^2$, $g(\boldsymbol{u}^2) = -2.59$, $\nabla g(\boldsymbol{u}^2) = (5.39, 4.06)$,

$\|\nabla g(\boldsymbol{u}^2)\| = 6.75$, $a^2 = \frac{\nabla g(\boldsymbol{u}^2)}{\|\nabla g(\boldsymbol{u}^2)\|} = (0.799, 0.602)$,

and $\beta^2 = \|\boldsymbol{u}^2\| = 2.91$

The process continues until the solution converges. The search ends after 9 iterations. The complete convergence history is shown in table 3.1.

Iteration	β	g	∇g	(U_x, U_y)
1	0	8.8902	(1.838, 1.384)	(0, 0)
2	3.863	-10.93	(9.15, 6.89)	(-3.087, -2.322)
3	2.91	-2.59	(5.39, 4.06)	(-2.33, -1.75)
4	4.17	-14.8	(11.2, 8.46)	(-3.33, -2.51)
5	3.11	-4.00	(5.96, 4.49)	(-2.49, -1.87)
6	2.57	-0.46	(4.59, 3.46)	(-2.06, -1.54)
7	2.490	0.022	(4.42, 3.33)	(-1.99, -1.49)
8	2.492	-0.02	(4.44, 3.34)	(-1.995, -1.496)
9	2.49036	-0.002	(4.42668, 3.3339)	(-1.9923,-1.4942)

Table 3.1: the MPP search history.

The MPP is found at $\boldsymbol{u}^*$= (-1.9923,-1.4942), and the reliability index is β = 2.49036. The probability of failure is then

$p_f = \Phi(-\beta) = \Phi(-2.4904) = 0.006380$

and the reliability is

R = 1 - p_f = 1 – 0.006380 = 0.99362

If the probability of failure obtained from Monte Carlo simulation with 10^6 simulations can be considered as an accurate solution, the output given by First Order Reliability Method offers a good approximation (Table 3.2) of the real value; at the same time, from a computational point of view,

FORM allows to save time and means, as it is not computationally expensive like Monte Carlo Method.

Method	Monte Carlo	FORM
Number of iterations	10^6	9
Probability of failure (output)	0.006417	0.006380

Table 3.2: Comparison between Monte Carlo Simulation and FORM.

3.4.3. Solving with SORM

In section 3.4.2, the MPP $\boldsymbol{u}^*$ = (-1.9923,-1.4942), the gradient of the limit-state function at the MPP $\nabla g(\boldsymbol{u}^*)$ = (4.42668, 3.3339), the unit vector $\boldsymbol{a}(\boldsymbol{u}^*)$ = (0.8, 0.6), and the reliability index β = 2.49036 were obtained.

The Hessian matrix $\nabla^2(\underline{u^*})$ requires second derivatives, which are given by

$$\frac{\partial^2 g}{\partial U_R^2} = \frac{-18\sigma_R^2 P l^3}{[3(\mu_R + \sigma_R u_R) + (\mu_K + \sigma_K u_K) l^3]^2}$$

$$\frac{\partial^2 g}{\partial U_K^2} = \frac{-2\sigma_K^2 P l^9}{[3(\mu_R + \sigma_R u_R) + (\mu_K + \sigma_K u_K) l^3]^3}$$

$$\frac{\partial^2 g}{\partial U_R \partial U_K} = \frac{-6\sigma_R \sigma_K P l^6}{[3(\mu_R + \sigma_R u_R) + (\mu_K + \sigma_K u_K) l^3]^3}$$

Thus, the Hessian Matrix results

$$H(\boldsymbol{u}^*) = \begin{bmatrix} -1.5675 & -1.1806 \\ -1.1806 & -0.88912 \end{bmatrix}$$

Determination of matrix **R**

First, matrix is $\boldsymbol{R_0}$ constructed:

$$\boldsymbol{R_0} = \begin{bmatrix} 1 & 0 \\ -\alpha_1 & -\alpha_2 \end{bmatrix} = \begin{bmatrix} 1 & 0 \\ -0.8 & -0.6 \end{bmatrix}$$

Let us now compute the rows of matrix **R**.

$$\boldsymbol{r_2} = \boldsymbol{r_{02}} = (-0.8, -0.6)$$

$$\boldsymbol{r_1^I} = \boldsymbol{r_{01}} - \sum_{j=2}^{2} \frac{\boldsymbol{r_j r_{01}^T}}{\boldsymbol{r_j r_j^T}} \boldsymbol{r_j} = \boldsymbol{r_{01}} - \frac{\boldsymbol{r_2 r_{01}^T}}{\boldsymbol{r_2 r_2^T}} \boldsymbol{r_2} = (1,0) - \frac{(-0.8,-0.6)(1,0)}{(-0.8,-0.6)(-0.8,-0.6)^T}(-0.8,-0.6) =$$
$$= (0.36,-0.48)$$

and

$$\boldsymbol{r_{01}} = \frac{\boldsymbol{r_1^I}}{\|\boldsymbol{r_1^I}\|} = (0.6,-0.8)$$

Therefore,

$$\boldsymbol{R} = \begin{bmatrix} \boldsymbol{r_1} \\ \boldsymbol{r_2} \end{bmatrix} = \begin{bmatrix} 0.6 & -0.8 \\ -0.8 & -0.6 \end{bmatrix}$$

Determination of matrix $\boldsymbol{A}$

$$\frac{\boldsymbol{R}\nabla^2 g(\boldsymbol{u}^*)\boldsymbol{R}^T}{\|\nabla^2 g(\boldsymbol{u}^*)\|} = \begin{bmatrix} -1.588 \cdot 10^{-6} & -8.8991 \cdot 10^{-4} \\ -8.8991 \cdot 10^{-4} & -0.4433 \end{bmatrix}$$

$$\xrightarrow{\boldsymbol{yields}} \boldsymbol{A} = [-1.588 \cdot 10^{-6}]$$

Computation of the principal curvature k_1

Let us solve the following eigenvalue problem:

$$\mathbf{A}\boldsymbol{Z} = k\boldsymbol{Z}$$

$$det(\mathbf{A} - k\boldsymbol{I}) = det[-1.588 \cdot 10^{-6}] = 0$$

Hence, the eigenvalue is $k_1 = -1.588 \cdot 10^{-6}$.

Computation of p_f

The probability of failure is

$$p_f^{SORM} = \Phi(-\beta) * \prod_{i=1}^{n-1} (1 + \beta * k_i)^{-\frac{1}{2}} = \Phi(-2.49036) * [1 + 2.49036 * (-1.588 * 10^{-6})] = 0.006380012$$

that is very close to the value that was found by using FORM (p_f^{FORM} = 0.00638).

Table 3.3 summarizes the outputs which were obtained by solving the example with the three different methods presented above.

Method	Monte Carlo	FORM	SORM
Number of iterations	10^6	9	9 + 1
Probability of failure (output)	0.006417	0.006380	0.006380

Table 3.3: Comparison between Monte Carlo Simulation and FORM/SORM.

In this particular case, one can notice a posteriori that there would not have been the necessity to use the SORM method, as the greater computational effort has not resulted in a significant improvement in the accuracy level that had been previously achieved by using FORM.

3.5. Risk analysis of a simple aeronautical structure

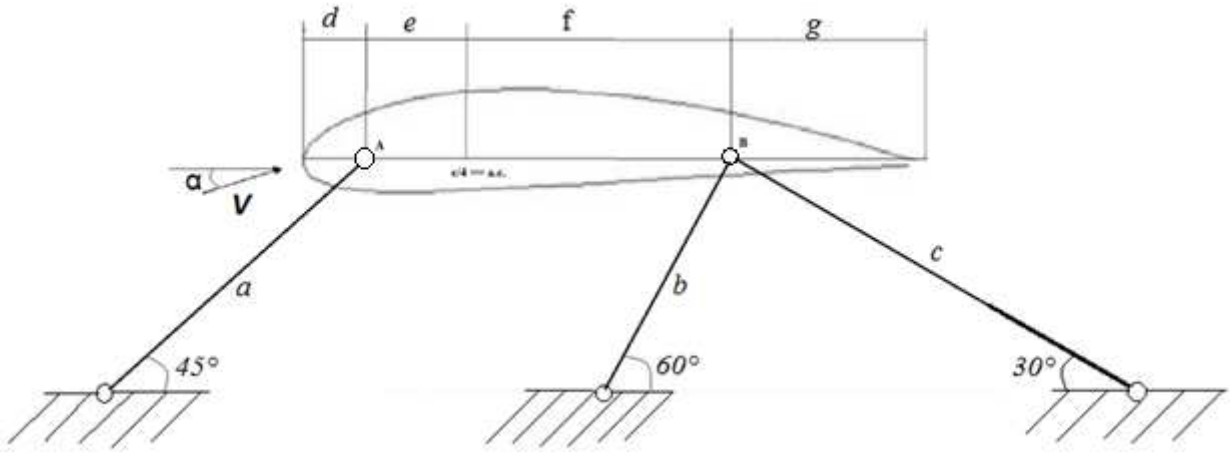

Figure 3.19: the case study consists of a NACA 4415 airfoil.

Reliability assessment will now be applied to the case of a structure which experiences aerodynamic forces (see Fig. 3.19); in this model, some data are deterministic, whereas others (i.e. the air speed and the lift coefficient) follow a random distribution. Prior to perform reliability analysis to the present application, the model has been studied from a deterministic point of view, and the results are reported in Appendix A.

A NACA 4415 airfoil constitutes the cross-section of a rectangular wing of 1.5 *m* chord and 9 *m* depth, which passes through an air stream at a given value of the angle of attack α. Such a wing is bound to a statically determinate structure in two nodes, called A and B. The aerodynamic forces generate stresses on rods *a*, *b*, and *c*. The goal of the simulation is to assess the probability of yielding of the front rod, i.e., the probability, for the stress on beam *a*, to be greater than the yield

stress of the material (*Al 7075-T6*), i.e. σ_Y = 462 *MPa*. Due to the constancy of the cross-section along the wingspan, the problem can be considered as two-dimensional.

Problem data:

Profile NACA 4415:

Chosen angle of attack: α = 0°;

Lift coefficient: $c_L = N$ (0.4,0.1) (normally distributed);

Drag coefficient: $c_D = 0.075$;

Moment coefficient at a quarter of the chord (i.e. ≈ the position of the aerodynamic center): $c_m = -0.1$;

Air flux:

Density ρ = 1.225 kg/m^3;

Velocity V_∞ = N(150,30) m/s (N = normally distributed);

Wing architecture:

e = 0.225 m (see figure 3.19);

f = 0.675 m (see figure 3.19);

Wing surface area S = 13.5 m^2;

Length of the chord: c = 1.5 m;

Section area of rod a: $A_a = 452.39\ mm^2$;

Section area of rods b and c: $A_b = A_c = A_{bc} = 176.71\ mm^2$;

From equation (A.12) (see Appendix A), the limit-state function is defined, in [*MPa*], by

$$G_a(\rho,V,\alpha) = \sigma_a - \sigma_Y = \left(-\frac{\sqrt{2}}{2A_a} * \rho * V^2 * S \left\{ \left[\frac{c_m * c + 2\pi * (\alpha - \alpha_{L=0}) * e}{e + f} \right] - 2\pi * (\alpha - \alpha_{L=0}) \right\} - 462 = 0 \right) \tag{3.64}$$

The following substitution (which is valid for the range of interest of the lift coefficient):

$$2\pi(\alpha - \alpha_{L=0}) = c_L \tag{3.65}$$

and some rearrangements lead to

$$G_a(c_L,V) = \sigma_a - \sigma_Y = \left(-\frac{\sqrt{2}}{2A_a} * \rho * V^2 * S\left\{ \left[\frac{c_m * c - c_L * f}{e+f} \right] \right\} - 462 \le 0 \right) \quad (3.66)$$

3.5.1. Solving the problem with Monte Carlo Method (MCS)

The execution of 10^8 iterations lead to a probability of failure $p_f = 0.0801$, which corresponds to a reliability index β = 1.405. Nevertheless, a good approximation of the p_f value is reached after 10^6 iterations, leading to p_f = 0.0805.

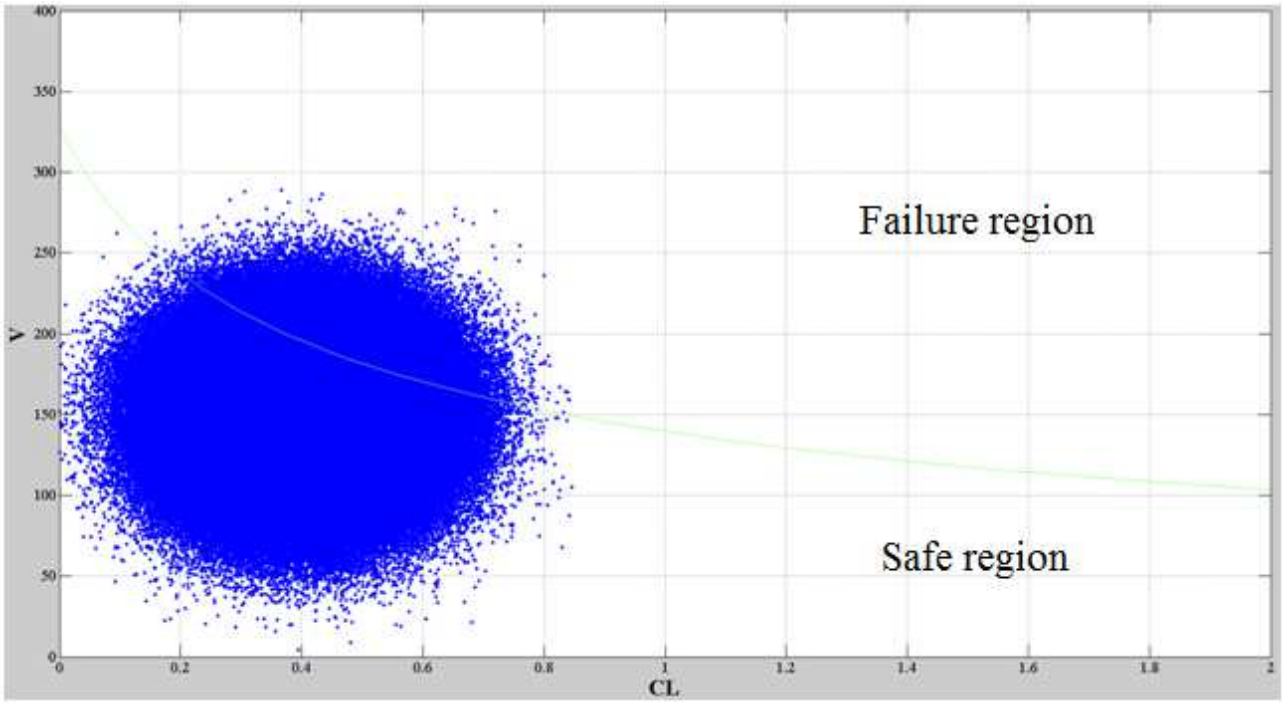

Figure 3.20: The blue *cloud* of points represents the 10^6 MCS simulations. The performance function $G_a(c_L,V) = 0$ is shown in green. The *cloud* is centered at the average values of the lift coefficient and of the velocity.

The limit-state function (3.66) has been used to divide the *safe zone* from the *failure zone*.

3.5.2. Solving the problem with FORM

To execute the simulation with the First Order Reliability Method, it is necessary to compute the gradient of the limit-state function. Before doing this, Rosenblatt Transformation is made, in order to have random variables that follow a standard normal distribution:

$$(c_L,V) = (\mu_{CL} + \sigma * U_{CL}, \mu_V + \sigma * U_V) = (0.4 + 0.1 * U_{CL}, 150 + 30 * U_V) \quad (3.67)$$

By substitution of the so expressed c_L and V into eq. (3.66) and after rearranging, the limit-state function comes to the following form:

$$G_a(\boldsymbol{U}) = G_a(c_L, V) = \sigma_a - \sigma_Y = -\frac{\sqrt{2}}{2A_a}\rho S(150 + 30U_V)^2\left[\frac{c_m c - (0.4+0.1U_{c_L})\cdot f}{e+f}\right] - 462 = 0 \tag{3.68}$$

The gradient of $G_a(c_L,V)$ is given by the derivatives of such a function by each of the different (here, they are only two) standard normal variables:

$$\frac{\partial G_a(U_{CL},U_V)}{\partial U_{CL}} = \frac{\sqrt{2}*\rho*S*f}{20*A_a*(e+f)}(150+30*U_V)^2 \tag{3.69}$$

$$\frac{\partial G_a(c_L,U_V)}{\partial U_V} = -\frac{30*\sqrt{2}*\rho*S}{A_a*(e+f)}(150+30*U_V)[C_m*c-(0.4+0.1*U_{CL})*f] \tag{3.70}$$

Hence,

$$grad(\boldsymbol{U}) = grad(U_{C_L}, U_V) = \left(\frac{\partial G_a(U_{C_L},U_V)}{\partial C_L}, \frac{\partial G_a(U_{C_L},U_V)}{\partial V}\right) =$$
$$\left\{\frac{\sqrt{2}\rho S f}{20A_a(e+f)}(150+30U_V)^2, -\frac{30\sqrt{2}\rho S}{A_a(e+f)}(150+30U_V)\left[c_m c - \left(0.4+0.1U_{C_L}\right)\cdot f\right]\right\} \tag{3.71}$$

The implementation of FORM method brought to convergence at MPP = (0.57125, 1.24315).

The resulting reliability index is then

$$\beta = \sqrt{U_{C_L}^2 + U_V^2} = \sqrt{0.57125^2 + 1.24315^2} = 1.3681 \tag{3.72}$$

As reported in Table 3.4, the convergence criterion on the MPP location, i.e.,

$$\text{if} \quad \|\boldsymbol{u}^{k+1} - \boldsymbol{u}^k\| \le \varepsilon_1, \quad \text{stop} \tag{3.73}$$

was satisfied.

Anyway, the other two alternative convergence criteria were satisfied, which are:

$$\text{if} \quad \|\nabla g(\boldsymbol{u}^{k+1}) - \nabla g(\boldsymbol{u}^k)\| \le \varepsilon_2, \quad \text{stop; or} \tag{3.74}$$

$$\text{if} \quad \|\beta^{k+1} - \beta^k\| \le \varepsilon_3, \quad \text{stop} \tag{3.75}$$

Once the reliability index β is known, the probability of failure is immediately derived:

$$p_f = \Phi(-\beta) = \Phi(-1.3681) = 0.085637 \tag{3.76}$$

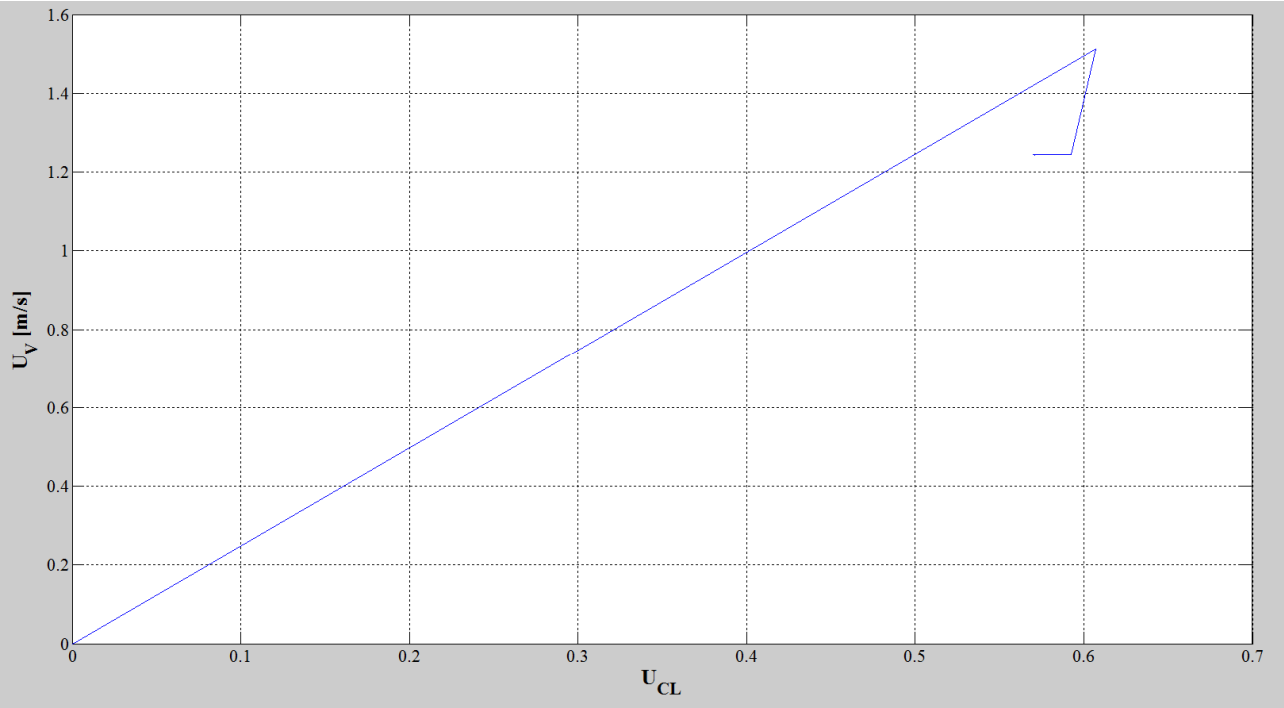

Figure 3.21: MPP search using FORM. As it can be clearly seen, *quasi-convergence* is reached after 3 iterations.

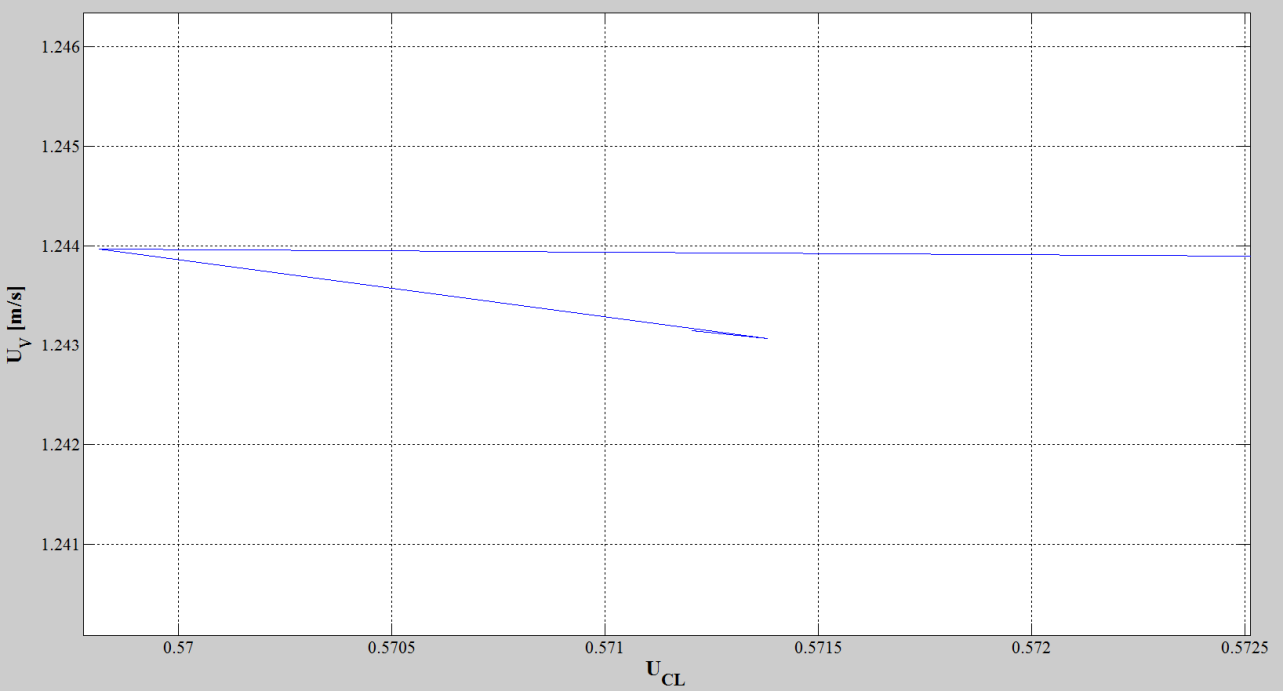

Figure 3.22: zoom on the MPP, located at $\boldsymbol{u}$ = (0.57125, 1.24315).

To make a comparison, recall that, with Monte Carlo Simulation (MCS), $p_f = 0.0801$. The precision here achieved with FORM corresponds to that of MCS after about 3000 iterations.

Iteration #	U_{CL}	U_V
1	0	0
2	0.6073	1.5115
3	0.5927	1.2434
4	0.5698	1.2440
5	0.5714	1.2431
6	**0.5712**	**1.2431**
7	**0.5712**	**1.2431**

Table 3.4: the MPP search (U_{CL} and U_V are in the first and second column, respectively) reaches convergence (with an accuracy of 10e-4) after 6 iterations.

3.5.3. Solving the problem with SORM

In order to increase the accuracy that is obtainable from the Reliability Analysis Methods, the Second Order Reliability Method (SORM) was performed.

In order to build the Hessian Matrix, the second order derivatives of $G_a(\boldsymbol{U}) = G_a(c_L, V)$ are needed:

$$\frac{\partial^2 G_a}{\partial U_{CL}^2} = 0$$

$$\frac{\partial^2 G_a}{\partial U_V^2} = -\frac{900\sqrt{2} * \rho * S}{A_a * (e+f)} * \left[c_m * c - (0.4 + 0.1 * U_{CL}) * f\right]$$

$$\frac{\partial^2 G_a}{\partial U_{CL} \partial U_V} = \frac{3\sqrt{2} * \rho * S * f}{A_a * (e+f)} * (150 + 30 * U_V)$$

Thus, the Hessian Matrix is

$$H(\boldsymbol{u}^*) = \begin{bmatrix} 0 & \frac{3\sqrt{2}\rho S f}{A_a(e+f)}(150 + 30U_V) \\ \frac{3\sqrt{2}\rho S f}{A_a(e+f)}(150 + 30U_V) & -\frac{900\sqrt{2}\rho S}{A_a(e+f)}\left[c_m c - \left(0.4 + 0.1 \cdot U_{c_L}\right) \cdot f\right] \end{bmatrix} =$$

$$= \begin{bmatrix} 0 & 21.7861 \\ 21.7861 & 23.7065 \end{bmatrix}$$

Construction of matrix $\boldsymbol{R}$

First, one constructs matrix $\boldsymbol{R_0}$:

$$\boldsymbol{R_0} = \begin{bmatrix} 1 & 0 \\ -\alpha_1 & -\alpha_2 \end{bmatrix} = \begin{bmatrix} 1 & 0 \\ -0.4175 & -0.9087 \end{bmatrix}$$

Let us now compute the rows of matrix $\boldsymbol{R}$.

$$\boldsymbol{r_2} = \boldsymbol{r_{02}} = (-0.4175, -0.9087)$$

$$\boldsymbol{r_1^I} = \boldsymbol{r_{01}} - \sum_{j=2}^{2} \frac{\boldsymbol{r_j} \cdot \boldsymbol{r_{01}^T}}{\boldsymbol{r_j} \cdot \boldsymbol{r_j^T}} \cdot \boldsymbol{r_j} = \boldsymbol{r_{01}} - \frac{\boldsymbol{r_2} \cdot \boldsymbol{r_{01}^T}}{\boldsymbol{r_2} \cdot \boldsymbol{r_2^T}} \cdot \boldsymbol{r_2} = (0.1743, 0.3794)$$

and

$$\boldsymbol{r_1} = \frac{\boldsymbol{r_1^I}}{\|\boldsymbol{r_1^I}\|} = (0.4175, 0.9087)$$

Therefore,

$$\boldsymbol{R} = \begin{bmatrix} \boldsymbol{r_1} \\ \boldsymbol{r_2} \end{bmatrix} = \begin{bmatrix} 0.4175 & 0.9087 \\ -0.4175 & -0.9087 \end{bmatrix}$$

All the elements needed to compute matrix ***A*** have now been obtained.

Hence,

$$\frac{\boldsymbol{R} \cdot \boldsymbol{\nabla^2 g}(\boldsymbol{u}^*)}{\|\boldsymbol{\nabla^2 g}(\boldsymbol{u}^*)\|} = \begin{bmatrix} 0.2217 & -0.2217 \\ -0.2217 & 0.2217 \end{bmatrix}$$

The 1x1 upper-left minor of the latter matrix is matrix ***A***:

A = [0.2217]

Let us now compute the principal curvature k_1:

The following eigenvalue problem has to be solved:

$$\boldsymbol{A}*\boldsymbol{Z} = k*\boldsymbol{Z}$$

then,

$$det(\boldsymbol{A}\text{-}k*\boldsymbol{I}) = det\left[0.2217 - k*1\right] = 0$$

that returns

$$k_1 = 0.2217$$

which is the needed eigenvalue.

As a final step, the probability of failure is determined:

$$p_f^{SORM} = \Phi(-\beta) * \prod_{i=1}^{n-1} (1+\beta * k_i)^{-\frac{1}{2}} = \Phi(-1.3681) * [1+1.3681 * 0.2217]^{-0.5} = 0.07501$$

that is slightly closer to the MCS solution than SORM method is.

Table 3.5 makes a comparison between the results provided by MCS, FORM and SORM. If the output obtained through MCS can be considered as the theoretically exact solution, it can be observed that the esteem of the probability of failure which was done by SORM is more precise of approximately 12% than the one computed by FORM.

Method	Monte Carlo	FORM	SORM
Probability of failure (output)	0.0801	0.085637	0.075013

Table 3.5: comparison between the probability of failure as esteemed by MCS, FORM and SORM.

3.5.4. First Order Second Moment method (FOSM)

The FOSM method (also known as *Mean Value method*) is based on a first order Taylor series expansion of the performance function; it is evaluated at the mean values of the random variables, and only uses means and covariances of the random variables (Swiler L.P. *et al.*, 2011).
Differently from FORM and SORM, FOSM method is performed analytically, and so it does not need iterations. A brief introduction to this algorithm is made in the sequel.

Let $\sum(\boldsymbol{X})$ be the covariance matrix (see Appendix B) of a generic vector of random variables $\boldsymbol{X}$; let us define the vector $\boldsymbol{a}$ as

$$\boldsymbol{a} = grad(g)|_{\boldsymbol{\mu}} \tag{3.77}$$

i.e., the average value of the gradient of the performance function.

It can be proved that, if $\boldsymbol{X} \in N(\mu_X, \sum(X))$ (i.e. if $\boldsymbol{X}$ follows a normal distribution), then

$$\begin{cases} \mu_g = g(\boldsymbol{\mu_X}) \\ \sigma_g^2 = \boldsymbol{a} \cdot \sum(\boldsymbol{X}) \cdot \boldsymbol{a^T} \end{cases} \tag{3.78}$$

As

$$\frac{\mu_g}{\sigma_g} = \beta\,, \tag{3.79}$$

the probability of failure can be immediately obtained:

$$p_f = \Phi(-\beta) = \Phi\left(-\frac{\mu_g}{\sigma_g}\right) \tag{3.80}$$

When *g(**X**)* is linear and the input variables are normal, the mean value method gives exact results (Swiler L.P. *et al.*, 2011).

To employ this method to the current example, let $\sum(c_L, V)$ be the 2x2 covariance matrix of the two random variables involved in the present simulation:

$$\sum(c_L, V) = \begin{bmatrix} 0.0100 & 0 \\ 0 & 899.9533 \end{bmatrix} \tag{3.81}$$

From Eq. (3.78),

$$\begin{cases} \mu_g = G_a(c_{L,avg}, V_{avg}) \\ \sigma_g^2 = \boldsymbol{a} \cdot \sum(c_L, V) \cdot \boldsymbol{a^T} \end{cases} \tag{3.82}$$

where $\mu_g = G_a(c_{L,avg}, V_{avg})$ is the value of the performance function when c_L and V assume their average values, i.e., 0.4 and 150 m/s, respectively.

The first equation of (3.82) then gives

$$\mu_g = G_a(0.4,150) = -190.59 MPa$$

To determine the standard deviation σ_g (second member of Eq. (3.82)), partial derivatives of the performance function (3.66) are calculated with respect to c_L and V:

$$\frac{\partial G_a}{\partial c_L} = \frac{\sqrt{2} * \rho * V^2 * S * f}{[2 * A_a * (e + f)]} \tag{3.83}$$

$$\frac{\partial G_a}{\partial V} = \frac{-\sqrt{2} * \rho * V * S * (c_m * c - c_L * f)}{(e + f)} \tag{3.84}$$

Using (3.83) and (3.84),

$$\boldsymbol{a} = grad[G_a(c_L, V)]|_{\boldsymbol{\mu}} = \left(\frac{\partial G_a}{\partial c_L}, \frac{\partial G_a}{\partial V}\right)\Big|_{\substack{c_L=0.4 \\ V=150}} = (436.2, 3.6188) \tag{3.85}$$

Then, from the second equation of the system (3.82),

$$\sigma_g = \sqrt{\left[\boldsymbol{a} \cdot \sum(c_L, V) \cdot \boldsymbol{a^T}\right]} = 116.9993$$

Hence,

$$p_f = \Phi\left(-\frac{\mu_g}{\sigma_g}\right) = 0.05166$$

This result is farther from the theoretically exact solution than FORM and SORM are. The reason could be the nonlinearity of the performance function, which significantly reduces the accuracy of FOSM.

3.5.5. A modified FOSM

In order to improve its accuracy, FOSM classical method was modified as follows. In equation (3.80), the mean performance function was approximated as a function of the mean values of the lift coefficient and the aircraft speed.

Let us now compute the real value of $\mu(g)$ as referred to n samples:

$$\mu_g = \sum_{i=1}^{n} \frac{G_a(c_{L,i}, V_i)}{n} \tag{3.84}$$

rather than

$$\mu_g = g(\boldsymbol{\mu_X})$$

The same is done for the mean of the performance function gradient:

$$\overline{\boldsymbol{a}} = \sum_{i=1}^{n} \frac{grad[G_a(c_{L,i}, V_i)]}{n} \tag{3.85}$$

rather than

$$\boldsymbol{a} = grad[G_a(c_L, V)]|_{\boldsymbol{\mu}} = \left(\frac{\partial G_a}{\partial c_L}, \frac{\partial G_a}{\partial V}\right)\Big|_{\substack{c_{L,avg}=0.4 \\ V_{avg}=150}}$$

From (3.84) and (3.85),

$\mu_g = -179.6014\ MPa$, and

$$\boldsymbol{a} = (453.9596, 3.6192)$$

Which were computed by considering $n = 10^6$ in both Eqs. (3.84) and (3.85).

Then, from the second equation of the system (3.80),

$$\sigma_g = 117.6839$$

$$\Rightarrow p_f = 1 - normcdf\,(0, -179.6014, 117.6839) = 1 - 0.9365 = 0.0635$$

This result is substantially more accurate than the one obtained with standard FOSM method.

3.5.6. Comments

The following table is to compare the proposed FOSM methods with the previously implemented methods; here, they are ordered from the most accurate to the least accurate.

Method	Probability of failure
Monte Carlo	0.0801
FORM	0.085637
SORM	0.075013
FOSM (modified)	0.0635
FOSM	0.05166

Table 3.8: comparison between the probability of failure obtained with FOSM methods with the ones previously computed via MCS, FORM and SORM.

As stated previously, the result from Monte Carlo Method can be taken as the correct solution, due to the huge number of simulations that were performed. FORM method gives an approximation with an error of about 0.55%, whereas SORM method brought, in this case, to a relatively poor improvement, if compared with the first order approximation: indeed, using SORM, the error is 0.5%, i.e. only 0.06% closer to the true solution than FORM (with an improvement in accuracy of 12%). This fact suggests that, for this particular application, the bigger computational cost for performing SORM is not fully repayed in terms of improved accuracy, if compared with FORM.

As regards FOSM methods, they resulted to be the least accurate one between the methods that were applied to this example. On the other hand, due to the lack of iterations, the FOSM and modified FOSM are often recommended for complex systems, where a huge number of computations would be otherwise needed. In this way, a considerable amount of time can be saved.

3.6. Conclusions

This chapter was devoted to the description and evaluation of some of the main reliability assessment algorithms. The issue to be solved is the computation of the reliability of a system, which, from an analytical point of view, derives from the integration of the *joint probability density function (jpdf*) of the random variables inside the *safe domain*, i.e., that part of the random variables space in which the structure is expected to survive under predefined (usually extreme) events. The most immediate and easy to use technique is Monte Carlo Simulation (MCS). Provided a sufficient number of simulations, MCS results to be the most accurate method for computing the probability of failure of a system, so much so that it is often used as a benchmark for the validation of other algorithms. On the other hand, MCS is not suitable for repeatedly performing complex computations like those which are concerned with many engineering applications; therefore, approximated methods are often used. Among these ones, the most popular ones are First and Second Order Reliability Methods (FORM and SORM), which simplify the expression of the *jpdf* (i.e., the integrand), and, on the other hand, simplify the integration domain through approximating the limit-state function $g(X) = 0$ at the Most Probable Point (MPP) with a Taylor Expansion of the

first or second order, respectively. These methods were tested first on an elementary, statically indeterminate, structure, and then on an aerofoil which is constrained to the ground through a statically determinate structure. Considering the probability of failure computed via MCS (after 10^6 and 10^8 iterations, respectively) as the exact solution, the execution of FORM brought to an error of 0.0037% and 0.55%, respectively. Compared to FORM, the subsequent implementation of SORM determined an accuracy improvement only in the second case (of 12%), whereas the output relative to the first case remained unchanged. This suggests that the use of SORM method should be considered with a grain of salt, i.e., in compliance with the accuracy needs, and by taking into account that the desired improvement in accuracy (compared to FORM) can be not so significant, and that, in any case, there will be an increase in the computational burden. Anyway, the use of SORM results to be convenient when the performance function is highly nonlinear. While studying the second applicative cases, First Order Second Moment (FOSM) method and a modified version of the latter were applied; when $g(\boldsymbol{X})$ is linear and the random variables are normal, FOSM provides the mathematically exact solution; however, this is not the case of the airfoil simulation, in which these techniques resulted therefore to be significantly less accurate than FORM and SORM.

To sum up, among the reliability assessment methods that have been seen and tested in this chapter, the author's opinion is that the First Order Reliability method (FORM) resulted to be perhaps the one that offers the best compromise between accuracy and computational costs.

Chapter 4

Deterministic optimization

4.1. Introduction

In engineering design, optimization is a technque which allows to satisfy the need of maximizing (or minimizing) a certain performance, while complying with some feasibility requirements. Indeed, in a design, the choice of the dimensions of the system to be realized are normally limited to some predefined intervals; moreover, safety requirements impose additional limitations to the system properties, in order to prevent any form of failure, or even danger for the surrounding environment. The latter conditions are met through the use of some appropriate constraint functions. From a mathematical point of view, optimization is the solution of a constrained extrema problem inside a selected subspace. The analytical formulation of the problem is as follows:

$$\begin{cases} Minimize\ f(d_1, d_2, \dots, d_n) \\ subject\ to \\ g_i(d_1, d_2, \dots, d_n) \leq 0,\ i = 1,2, \dots, n_i \\ h_j(d_1, d_2, \dots, d_n) = 0,\ j = 1,2, \dots, n_e \\ d_k^l \leq d_k \leq d_k^u,\ k = 1,2, \dots, n \end{cases} \tag{4.1}$$

where $(d_1, d_2, \dots, d_n)$ is the vector of the design variables that will be determined during the design; $f(d_1, d_2, \dots, d_n)$ is the design *objective function* (or *fitness function*) which has to be minimized; $g_i(d_1, d_2, \dots, d_n)$ are the *inequality constraints*, which limit the space to a feasible domain; $h_i(d_1, d_2, \dots, d_n)$ are *equality constraints*; d_k^i and d_k^u are, respectively, the lower and the upper bound for each of the *k* design variables. In other words, the problem can be understood as: find the set of design variables ***d*** which minimizes the performance function *f* while respecting the design constraints.

To sum up, an optimization model is normally composed of three main components: the *design objective*, the *design variables* and the *design constraints*. Let us now analyze in detail each of them.

Design variables

The design variables are under the control of the designer, and every different combination of them determines a different design. The goal of the design optimization is to find the best combination of design variables that optimizes the designer's preference (*design objective*) and maintains certain requirements (*constraints*) (Du X., 2006). A typical engineering example of design variables managing is the choice of the geometric dimensions of a structure.

Design variables are normally in one of the following forms:

- **continuous variables**;

- **integers**, e.g. the number of heat pipes in a cooling system for a spacecraft instrument, or the number of teeth in a gear;

- **a discrete variable**, which can take values only from a discrete set (for example, a catalogue).

Design objective

The design objective represents the designer's goals. The mathematical representation for the design objective is the *objective function* (or *fitness function*), which is represented in terms of design variables. Typical examples of objective functions include weight and costs, or aerodynamic efficiency. From a computational point of view, the fitness function is normally expressed as a quantity to be minimized. However, if one wants to maximize the fitness function $f(d_1, d_2, \dots, d_n)$ in equation (4.1), the design objective can be expressed as

$$Maximize\{-f(d_1, d_2, \dots, d_n)\}$$

i.e., with a change of sign.

In many complex design problems, more than one performance have to be optimized; to solve this kind of problems, *multiobjective optimization* is performed.

Design constraints

Constraints are function of the design variables, and limit the domain of the possible solutions; they have to be strictly satisfied. Some examples of design constraints include the maximum allowed deflection or stress in a beam, or the minimum required level of reliability.

4.2. Optimization algorithms

Several kinds of algorithms can be used to solve an optimization problem; they can be divided into some main categories: analytical methods, graphical methods, and numerical methods; in the latter group, the gradient-based algorithms and the genetic algorithms (GA) are the most used.

4.2.1. Analytical method

This kind of method requires the solution of the *Karush-Kuhn-Tucker conditions*, which are a generalization of the Lagrange Multipliers Method (which allows only equality constraints) and are reported below:

$$\begin{cases} \frac{\partial f(\boldsymbol{d})}{\partial d_i} + \sum_{j=1}^{n_i} w_j \frac{\partial g_j(\boldsymbol{d})}{\partial d_i} + \sum_{k=1}^{n_e} v_k \frac{\partial h_k(\boldsymbol{d})}{\partial d_i} = 0, \ i = 1,2,\dots,n \\ w_j g_j(\boldsymbol{d}) = 0, \ \ for\ j = 1,2,\dots,n_i \\ w_j \geq 0, \ for\ j = 1,2,\dots,n_i \\ h_k(\boldsymbol{d}) = 0, \ \ for\ k = 1,2,\dots,n_e \end{cases} \tag{4.2}$$

where w_j and v_k are undetermined constants (from Du X., 2006).

Due to the computational complexities that arise when equations (4.2) are nonlinear, the analytical solution is limited to very simple cases only.

4.2.2. Graphical method

For very simple problems involving up to two variables, the optimal point can be found through the following method:

- plot the constraint boundaries to define the feasible and the infeasible regions;
- plot the contours of the objective function, and find the direction along which the objective function increases or decreases;
- identify the *optimal point*, i.e., that point whose coordinates (d_1, d_2) correspond to the optimal design solution. This point is related to the minimum value of the fitness function inside the allowed region, and it is usually located along one of the constraint boundaries; it often coincides with the tangency point between a contour of the objective function and one of the constraints, as depicted in Fig. 4.1.

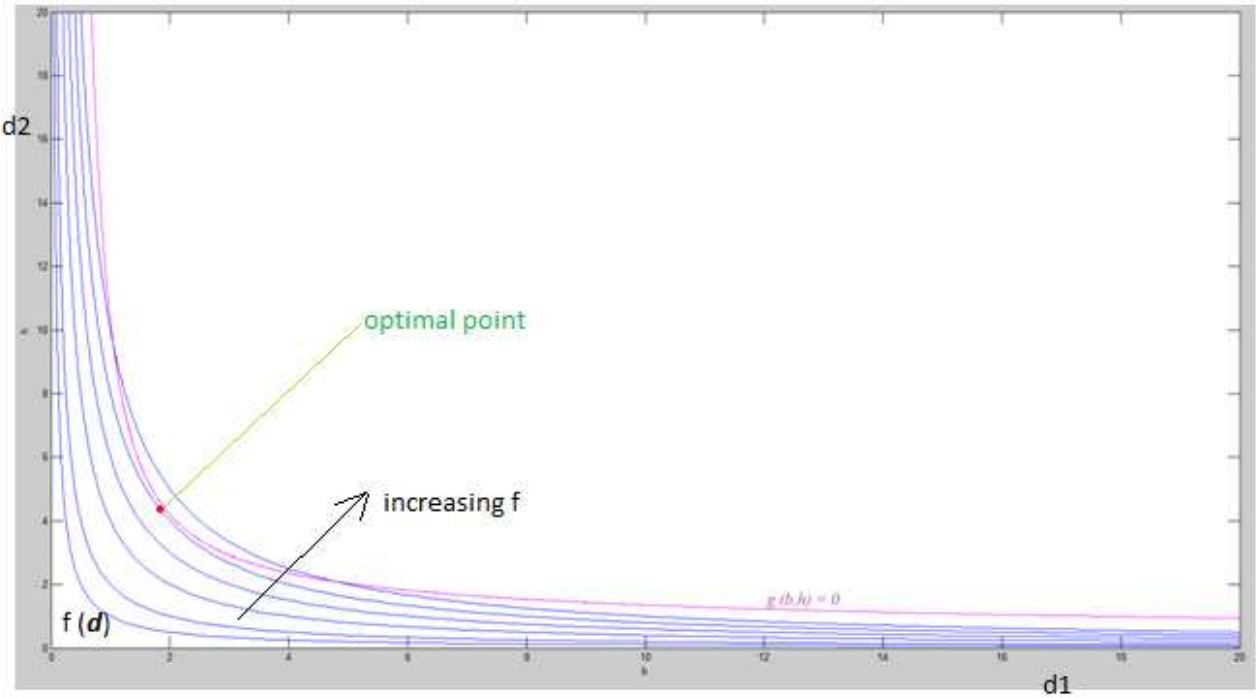

Figure 4.1: example of optimization through the graphical method. The limit-state function $g(d_1, d_2) = g(b, h) = 0$ (in magenta) divides the space into the feasible region and the infeasible region. Each of the blue curves indicates a particular value of the objective function *f*.

4.2.3. Gradient-based numerical method

Due to the high complexity level, most of the engineering problems cannot be solved by analytical or graphical methods. One of the alternatives is given by *gradient-based numerical methods*. With a numerical method, the optimal design starts from an initial design point (starting point) that represents an initial design. The numerical optimizer evaluates the objective function, the constraint functions and their derivatives and, based on their values, the optimizer generates a search direction along which the objective function will be likely to descend (see Fig. 4.2). A step size along the descent direction will be searched such that the objective function will decrease to the lowest possible value without violating any constraint. Then, at the following iteration, the current design point moves along the search direction with the specified step size. A new design point is then obtained. The optimizer evaluates the objective function and the constraint functions again at the new design point and checks whether the solution converges (from Du X., 2006). If convergence is not reached, the optimizer generates a new search direction and the relative step size for the following iteration. This procedure continues until an optimal solution is found.

Let us now consider a simple two-dimensional case of optimal point search, in which the design point after *k* iterations is $\boldsymbol{d^k}$ (see Fig. 4.3); to determine the next iteration, i.e, $\boldsymbol{d^{k+1}}$, the search direction $\boldsymbol{\alpha^k}$ and the step size $\boldsymbol{\beta^k}$ are generated, so that the new design point is

$$\boldsymbol{d^{k+1} = d^k + \beta^k \alpha^k}$$

As for the termination criteria, two of the most popular ones are the following:

1) The distance between two consecutive design points has to be less than a tolerance ε_1:

$$\left\| \boldsymbol{d^{k+1} - d^k} \right\| \leq \varepsilon_1$$

2) The difference between the fitness functions relative to two consecutive design points has to be less than a tolerance ε_2:

$$\left| f\left(\boldsymbol{d^{k+1}}\right) - f\left(\boldsymbol{d^k}\right) \right| \leq \varepsilon_2$$

To perform gradient-based optimization, the available numerical routines are normally used, where the search process is fully automatic.
One of the limits of this kind of methods is that they can converge to local minima rather than global minima (see Fig. 4.4); therefore, to obtain the optimal solution, a different starting point should be used.

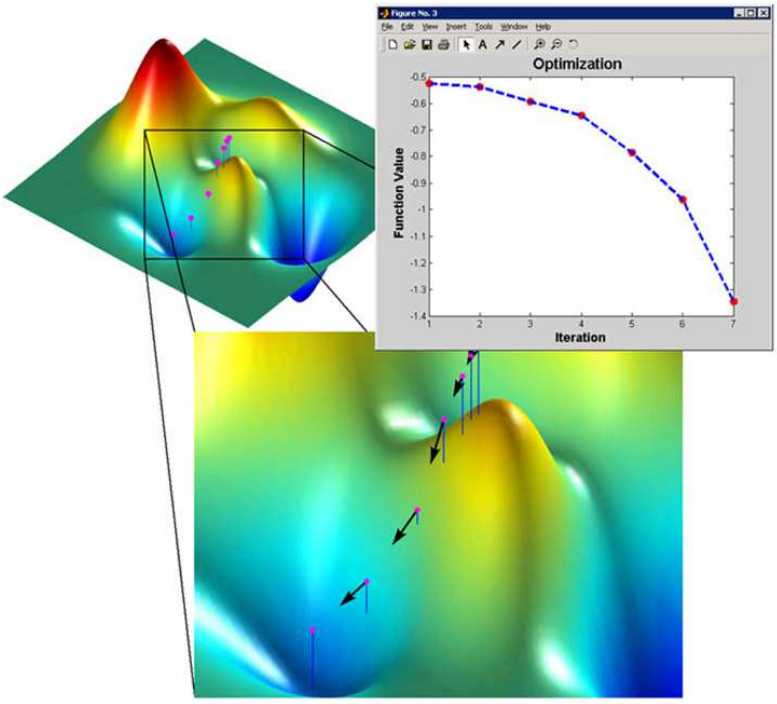

Figure 4.2: example of a a gradient-based optimization procedure to look for a minimum value (from S. Kozola, 2009).

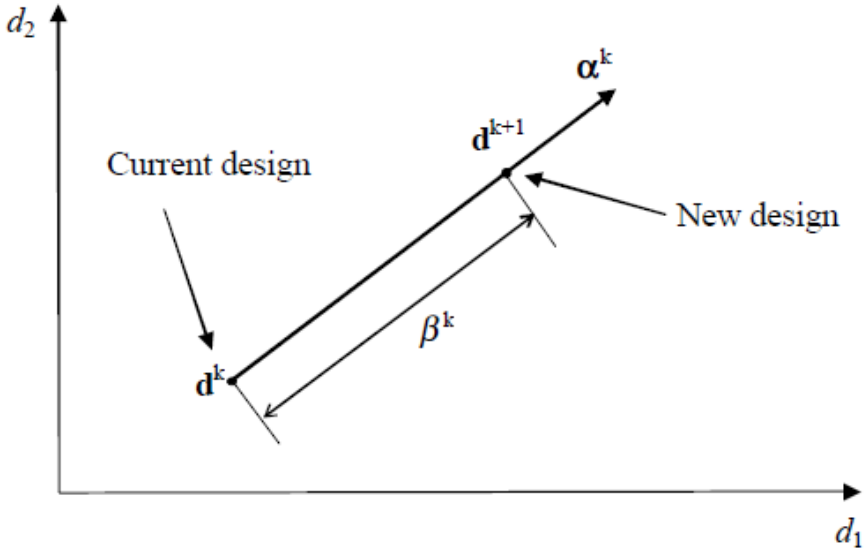

Figure 4.3: example of the *k*-th iteration of an optimal point search: the new design point $\boldsymbol{d^{k+1}}$ is found from the previous design pont $\boldsymbol{d^k}$ by making a $\boldsymbol{\beta^k}$ move along the $\boldsymbol{\alpha^k}$ direction (from Du X., 2006).

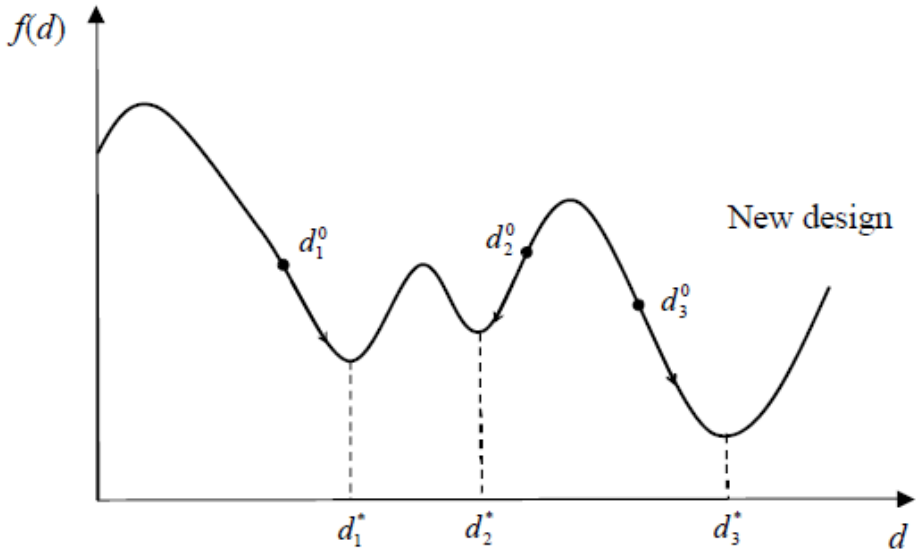

Figure 4.4: this case, in which a single design variable *d* involved, is useful to highlight how the choice of the starting design point is crucial: indeed, for some starting points such as d_1^0 and d_2^0, the gradient-based numerical method can converge to a local minimum (i.e., d_1^* or d_2^*), rather than to the global minimum d_3^* (from Du X., 2006).

4.2.4. Genetic algorithms (GA)

This kind of algorithms act in an heuristic way that mimics the process of natural selection. They are based on the classic view of a chromosome as a string of genes (Holland, 2012). In the selective breeding of plants or animals, for example, offspring are sought to have certain desirable characteristics, which are determined at the genetic level by the way the parents' chromosomes combine. By using this concept, R.A. Fisher (1958) contributed to the development of mathematical genetics by providing a theory specifying the rate at which particular genes would spread through a population. In the case of GAs, a *population* of strings is used, and these strings are often referred to in the GA literature as *chromosomes*. The elements of a string correspond to *genes*, and the values assumed by those genes correspond to *alleles*. The concept of *evolution* is carried out through a generation-by-generation process where, at each stage, a population of individuals produces a set of offspring that indeed constitutes the next generation. Then, a fitness function is associated to each of the new strings, in order to assign the number of offspring which that chromosome will contribute to during the next generation. Starting from the *parent* chromosomes, the recombination of such strings is carried out by using simple analogies of genetic *crossover* and (to a lesser extent) *mutation*, and the search is guided by the results of evaluating the objective function *f* for each string in the population. Based on this evaluation, strings that have higher *fitness* (i.e., represent better solutions) can be identified, and these are given more opportunity to breed (C. Reeves, 2003).

Let us now focus on the processes of recombination.
Crossover is a way of substituting some of the genes in one parent by corresponding genes of the other. Crossover in its simplest form (i.e., one-point crossover) can be defined as follows: given the parents P1 and P2, let us define the crossover point X: the pieces lying on the left of that point are exchanged between the two chromosomes, giving rise to a pair of offspring chromosomes O1 and O2 (see Fig. 4.5) .
Mammals' offspring exhibit a mix of their parents' characteristics mainly due to crossover (Holland, 2012).

P1	1	1	1	1	1	1	1
				X			
P2	0	0	0	0	0	0	0
O1	1	1	1	0	0	0	0
O2	0	0	0	1	1	1	1

Figure 4.5: parent strings (P1 and P2) undergoing crossover, from which the offspring (O1 and O2) is generated.

In *mutation*, on the other hand, a subset of genes is chosen randomly, and the allele value of the chosen genes is changed. In the case of binary strings, this simply means complementing the chosen bits (C. Reeves, 2003). For example, the string O2 (see Figure 4.5), with genes 2 and 7 mutated, would become 0 1 0 1 1 1 0.
If the new population of strings doesn't satisfy the convergence conditions, the recombination process will continue, as shown in the template that follows.

```
Choose an initial population of chromosomes;
while termination conditions not satisfied do
        repeat
                if crossover conditions not satisfied then
                {select parent chromosomes;
                choose crossover parameters;
                perform crossover};
                if mutation condition satisfied then
                {choose mutation points;
                perform mutation};
                evaluate fitness of offspring
        until sufficient offspring created;
select new population;
endwhile
```

Figure 4.6: general template for a genetic algorithm (from Reeves C., 2003).

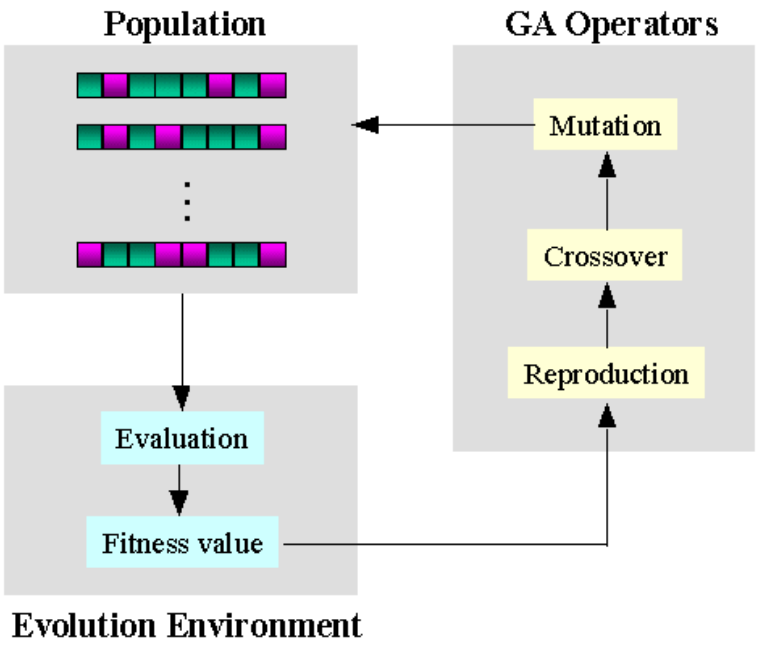

Figure 4.7: evolution flow of a genetic algorithm (from Liao and Sun, 2001).

4.3. Deterministic examples

4.3.1. Statically determined airfoil

As an introductory example to optimization design, a simple case, applied to a statically determinate profile (nearly the same that was analyzed in Chapter 3) will be herein presented. In this case, the performance of a gradient-based algorithm will be observed.

Compared to the case of Chapter 3, the only difference is that: the distance $(e + f)$ between nodes A and B is no more constant, due to the fact that f is now considered as one of the design variables; therefore, the position of the aerodynamic center (*a.c.*) is no more fixed a priori.

The goal of the present simulation is to minimize the ratio between f (i.e., the distance between the aerodynamic centre and node B) and the airplane velocity V, with the constraint about the yield strength that has not to be overtaken. The minimization of the f/V ratio is made with the aim of optimizing the performances while, at the same time, minimizing the wing obstruction (and, hence, its mass).

Anyway, the values of these two variables have to lie inside two intervals, which are, respectively:

- for the length f: [0.35 m; 1 m];
- for the velocity V: [100 m/s; 200 m/s].

Remember that, during the reliability analyses, the value for f was constant and equal to 0.675 m. For the rest, the model data are the same of Chapter 3.

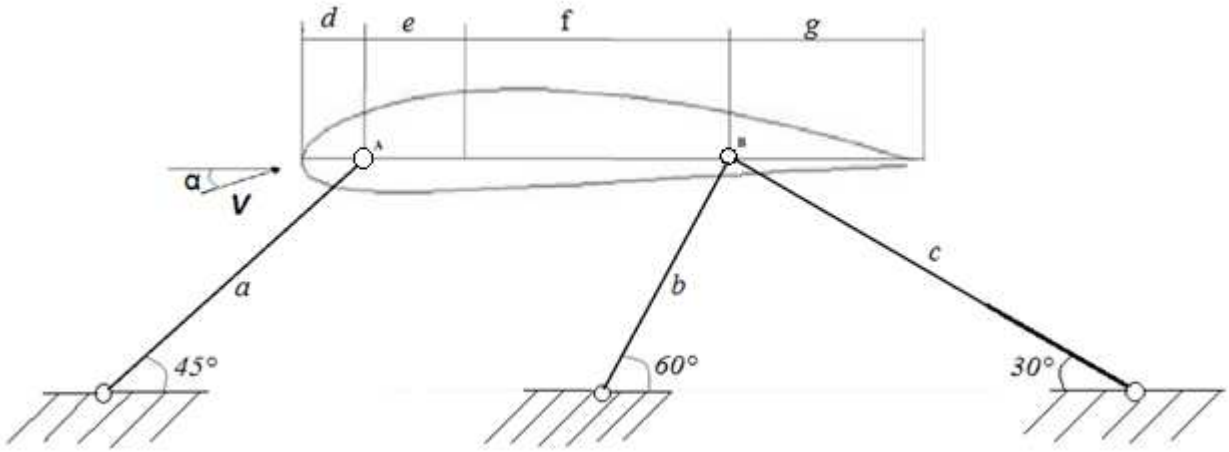

Figure 4.8: the airfoil structure which was optimized. While the airfoil depicted in figure 3.19 has a fixed geometry, in the present application the length f is a design variable.

The optimization model is given by

$$\begin{cases} Min\ \frac{f}{V} \\ s.t. \\ G_a(c_L, V) = \sigma_a - \sigma_Y \leq 0 \\ 0.35\ m\ \leq f\ \leq 1\ m \\ 100\ m/s \leq V \leq 200\ m/s \end{cases} \tag{4.3}$$

Where $\sigma_Y = 462\ MPa$ is the yield strength of the material (Al7075-T6).

A commercial routine implementing the gradient-based method was used.

The Matlab codes used - partially influenced by Du X. (2006) - are given in appendix C.1.

Analysis of the results

The results from Matlab are reported in Appendix C.1. The initial value of (*f,V*) was set to (0.675 m; 150 m/s). With such a starting point, the optimization process converges to:

V(opt)	***f(opt)***	***f/V (opt)***	***G_a(opt)* [safe if ≤ 0]**	***Tension on rod a***
150.0015 m/s	0.35 m	0.0023333	-168.6713 MPa	293.33 MPa

Table 4.1: outputs of the gradient-based optimization, when the starting points were set to *f* = 0.675 *mm* and *V*=150 *m/s*.

The optimal point - i.e. the minimum of the *f/V* ratio - is obtained for a value for a tension of 293.33 MPa, i.e. well under the yield limit of 462 MPa. The optimal value for the velocity is 150.0015 m/s: it lies inside the interval of [100m/s; 200 m/s], but it is extremely close to the value chosen for the starting point (150 m/s); on the other hand, the value of the distance f corresponding to the minimum is 0.35 m, i.e. on the lower limit of the interval. Subsequent simulations showed that such an optimal point is only a *local minimum*, and it is far from the *global minimum*.

Then, a global minimum search was performed, which consisted in varying the starting values of *f* and *V*, until it was found that, while the optimal point is independent on the initial value of *f*, it strongly depends on the initial value of *V*.

The *point of global minimum* is

$$(f, V)_{glob\ min} = (0.35\ m, 188.25\ m/s)$$

which corresponds to the limit value of the performance function, i.e., $G_a(c_L, V) = \sigma_a - \sigma_Y = 0$.

Such an optimal point, that corresponds to the performance function reaching zero (i.e., the material yielding), is obtainable by initializing the velocity with a value between 188.25 m/s and about 199 m/s. For a starting velocity of 188.24 m/s (i.e. 0.01 m/s less than the value of *V* which corresponds to the optimal *f/V* ratio), the optimum is not reached; this fact indicates that, in the present example, the utilized gradient-based routine is efficient only on the *right neighbourhood* of the point corresponding to optimum.

The results referring to the case in which the initialization of (*f*,*V*) was set to (0.36 m; 199 m/s) are reported in Appendix C.1.

The performance function

The trend of the performance function inside the interval is reported in Fig. 4.9. There, the red plane represents the limit case in which the acting tension equals the yield stress of the material: thus, the intersection between the coloured surface and the red plane represents the limit case in which the acting forces are equal to the yield stress of the material: the part of the performance function that lies above such a plane is connected to the deterministic failure of the structure.

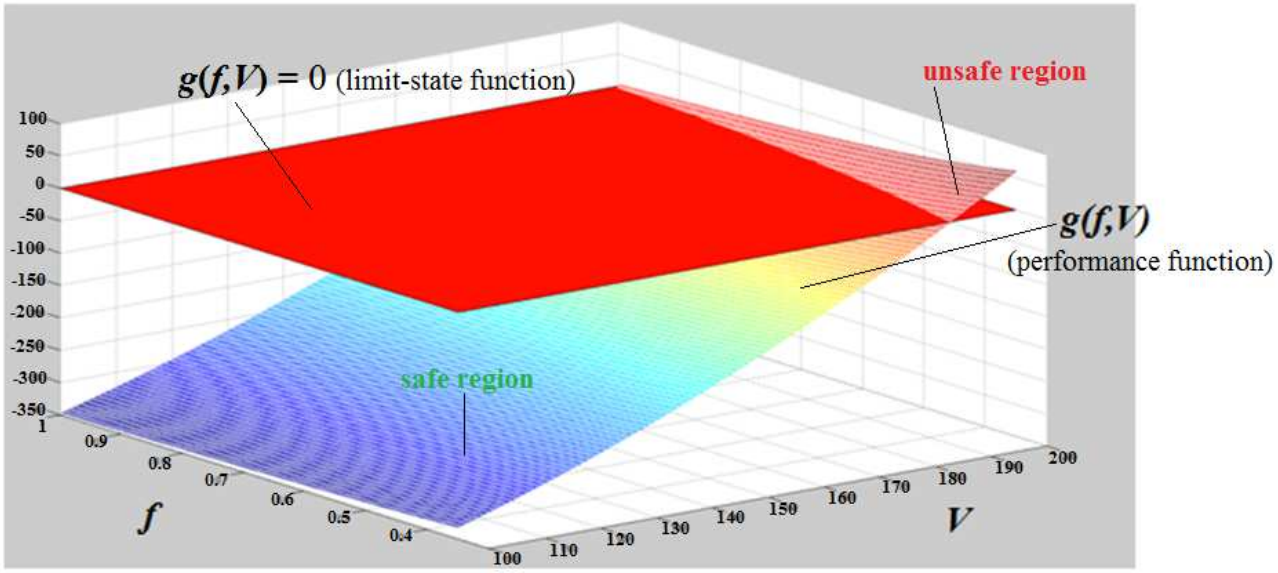

Figure 4.9: The intersection between the coloured performance function and the red plane locates the limit-state function *G*(*V*,*f*) = *0*. The portion of the performance function which lies above such a limit (i.e., on the right) identifies the configurations (couples of *V* and *f*) which bring to failure.

Looking for minimum points

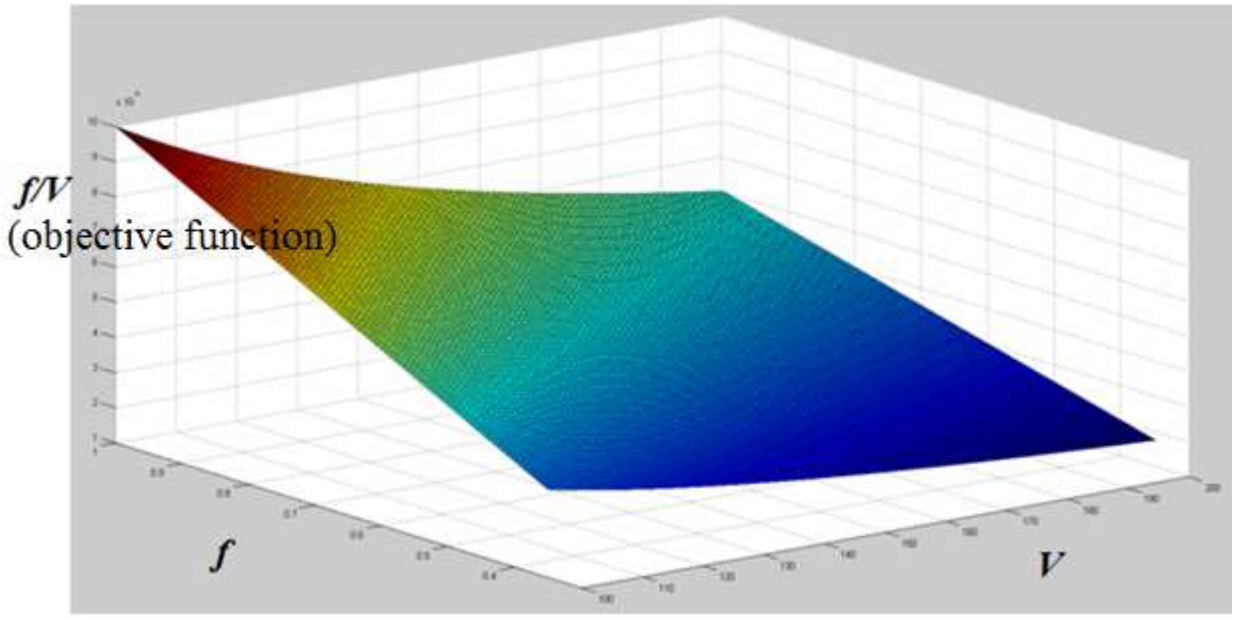

Figure 4.10: the trend of the objective function *f/V* inside the selected interval.

As it can be seen from Fig. 4.10, there is only one minimum in the domain that was chosen: as it can be easily computed, the minimum of *f/V* in the domain is found for the minimum value of f by the maximum of *V*, i.e. 0.35/200 = 0.00175. Moreover, there isn't any *stationary point* (i.e., where the Hessian Determinant is zero): this suggests that, ideally, a gradient-based algorithm would have to converge to (*f*,*V*) = (200,0.35) for whichever starting point on the domain. Nevertheless, one has also to remember the presence of the constraints (namely, the *unsafe region* in Fig. 4.9), which circumscribes the optimum point search to the *allowed region* only. Hence, (*V*, *f*) = (*188.25 m/s*, *0.35 m*) is the *constrained global minimum point*.

4.3.2. Cantilever beam

A cantilever beam having a rectangular section and a fixed length is subjected to a pure bending force on its tip, whose components are P_x and P_y. Let us want to dimension the cross-sectional geometry, such that the beam mass results to be minimized, while respecting the constraint on the maximum allowable stress (i.e., the yield stress). Due to the constant section and the homogeneous density, the mass minimization problem can be reduced to the minimization of the cross-sectional area of the beam, which is expressed as *A* = *b*h* (see Fig. 4.11).

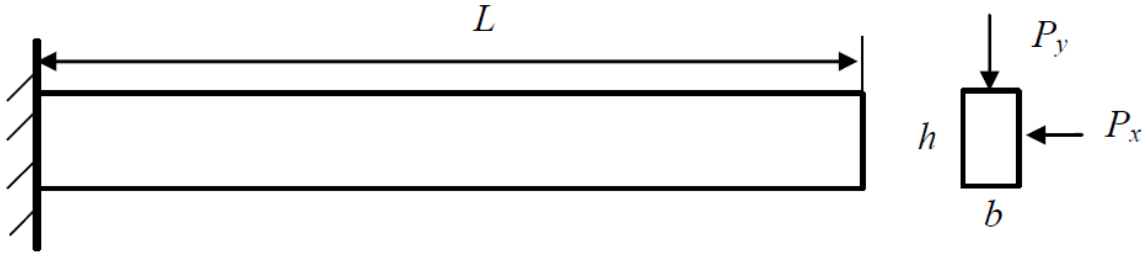

Figure 4.11: cantilever beam subjected to a pure bending force on its tip.

Nevertheless, the section base *b* and heigth *h* values have to lie inside predefined intervals.

Problem data:

L = 2540 *mm*;

E = 200,000 *MPa*;

$P_x = 2227\ N$;

$P_y = 4454\ N$;

$S_Y = 241.3\ MPa$ (yield strength);

$b^l \leq b \leq b^u\ \ [b^l = 25.4\ mm, b^u = 254\ mm]$;

$h^l \leq h \leq h^u\ \ [h^l = 25.4\ mm, h^u = 508\ mm]$;

The constraint is deterministically expressed as the performance function *g* (Equation 4.4); from a deterministic point of view, this function has to be negative, i.e. the acting stress has not to overtake the yield stress *S* of the material, i.e.,

$$g(P_x, P_y) = \frac{6L}{bh}\left(\frac{P_x}{b} + \frac{P_y}{h}\right) - S_Y \leq 0 \tag{4.4}$$

or,

$$g(P_x, P_y) = S - S_Y \leq 0 \tag{4.5}$$

To summarize, the optimization problem is given by:

$$\begin{cases} \min A \\ s.t. \\ g(P_x, P_y) = S - S_Y \leq 0 \\ b^l \leq b \leq b^u \\ h^l \leq h \leq h^u \end{cases} \tag{4.6}$$

The starting point for the optimization process is set to *(b,h)* = (50.8, 50.8) *mm*.

Optimization

Optimization is performed by using the the same gradient-based routine which was used in section 4.3.1, and the chosen algorithm follows *interior point method*. The iterations data and the final results are reported in Appendix C.1. The first optimization loop provides the following results:

(b,h) = (52.0055, 104.011) *mm*

Objective function = 5409.14 mm^2

Approaching the problem from a different starting point

To assess the stability of the gradient-based method in the present application, a new starting point was settled at *d=(203.2, 50.4) mm.*

Optimization:

The optimal objective function results to be $A_{opt} = 5409.14\ mm^2$, the optimal point being

$(b, h)_{opt}$ = (52.0055, 104.011) *mm*.

One can notice that the optimization outputs are exactly the same as in the previous case [i.e., starting from *(b,h)=(50.8,50.8) mm*].

Changing again the starting point

Other starting points were selected as input for the optimization problem, namely:

(b,h)=(228.6, 533.4) mm;

(b,h)=(251.5, 505.5) mm;

(b,h)=(25.65, 25.65) mm;

(b,h)=(127, 381) mm;

nevertheless, all of them leaded to the same result, namely

$(b, h)_{opt}$ = (52.0055, 104.011) *mm*

$A_{opt} = 5409.14\ mm^2$

Inspecting the force-geometry correlation along x and y directions

In the last paragraphs, it was noticed that optimization results brought to beam sections in which the ratio between the horizontal and the vertical side of the section was always equal to 0.5. In order to understand the reason for this, the values of the acting forces P_x and P_y were changed, in order to state whether there is any law which defines the optimal geometry of the section.

In all the optimization cycles that have been performed up to now, the ratio between the acting force along *x* direction and the one along *y* was equal to $\frac{P_x}{P_y} = \frac{2227N}{4454N} = 0.5$.

The optimization cases that follow were performed in the hypothesis that the starting geometry was *(b,h)=(50.4, 50.4) mm*, and with all the numerical assumptions that have been made up to now.

Varying the acting forces in intensity and in their mutual ratio

- If one chooses $P_x = P_y$ = 4454 *N*, the optimal result is:

  $b_{opt} = h_{opt}$ = 82.517 *mm*

  That is to say, to a $\frac{P_x}{P_y}$ ratio equal to1, the routine returns a b_{opt}/h_{opt} ratio equal to 1.

- If $P_x = 8908$ *N* and P_y = 44.54 *N*, the optimal section is the one with:
  b_{opt} = *150.92 mm*, h_{opt} = 25.4 *mm*.
  In this last case, the optimization was limited by the fact that the lowest allowed value for *h* was reached.

Changing the allowed intervals for *b* and *h*:

The lower and upper bounds for the design variables have been, up to now:
25.4 *mm* ≤ *b* ≤ 254 *mm* and
25.4 *mm* ≤ *h* ≤ 508 *mm*;
Such values will be herein changed.

- Let us now choose $P_x = 8908$ *N* and P_y = 44.54 *N* again, but with a different set of allowed intervals for the sizes of *b* and *h*, namely
  25.4 *mm* ≤ *b* ≤ 254 *mm* and
  0 *mm* ≤ *h* ≤ 508 *mm*;

  the optimal section results to be the one with:

  b_{opt} = 25.4 *mm*, h_{opt} = 9.8334 *mm*.
  In this last case, the optimization was limited by the fact that the lowest allowed value for *b* was reached.

- The bounds of the design variables were changed again, keeping the same values of the acting forces:
  25.4 *mm* ≤ *b* ≤ 1270 *mm* and
  0 ≤ *h* ≤ 508 *mm*;

  the optimal section geometry is then given by:
  b_{opt}= 607.98 *mm*, h_{opt} = 3.04 *mm*; $A_{opt} = (b \cdot h)_{opt}$ = 1848.2 mm^2.

  It was found that b_{opt}/h_{opt} = *200*, the same ratio existing for the acting forces:
  P_x / P_y = 8908/445.4 = 200.

  It is important to notice that, in this case, the limit bound(s) were not reached.

- As a further proof of this trend, another different set of forces was chosen:
  $\begin{cases} P_x = 5010N \\ P_y = 17107N \end{cases}$

with
$25.4\ mm \leq b \leq 1270\ mm$ and
$0 \leq h \leq 508\ mm$;

Notice that $P_x / P_y = 0.3295$.
The optimization brought to

$$\begin{cases} b_{opt} = 56.99\ mm \\ h_{opt} = 172.97\ mm \end{cases}$$

and the b_{opt}/h_{opt} ratio is 0.3295, i.e., exactly equal to the ratio between the external acting forces.

Comments

As far as it has been seen during the present investigation, whenever the optimal geometry doesn't involve any limit bounds for the section allowed sizes, the ratio between b_{opt} (the side along *x* axis) and h_{opt} (the side along *y* axis) resulted to be equal to P_x / P_y, i.e. to the ratio between the acting force along *x* and the one along *y*.

4.3.2.1. Verifying the results through Graphical optimization

In the last sections, it was shown that the gradient-based function brought to the exact solution. The goal of the present paragraph is to perform the optimization from a graphical point of view, in order to compare it with the numerical results.

As it is shown in Fig. 4.12, every value of the objective function *f* is associated to a different hyperbole $f = b^* h = A$.

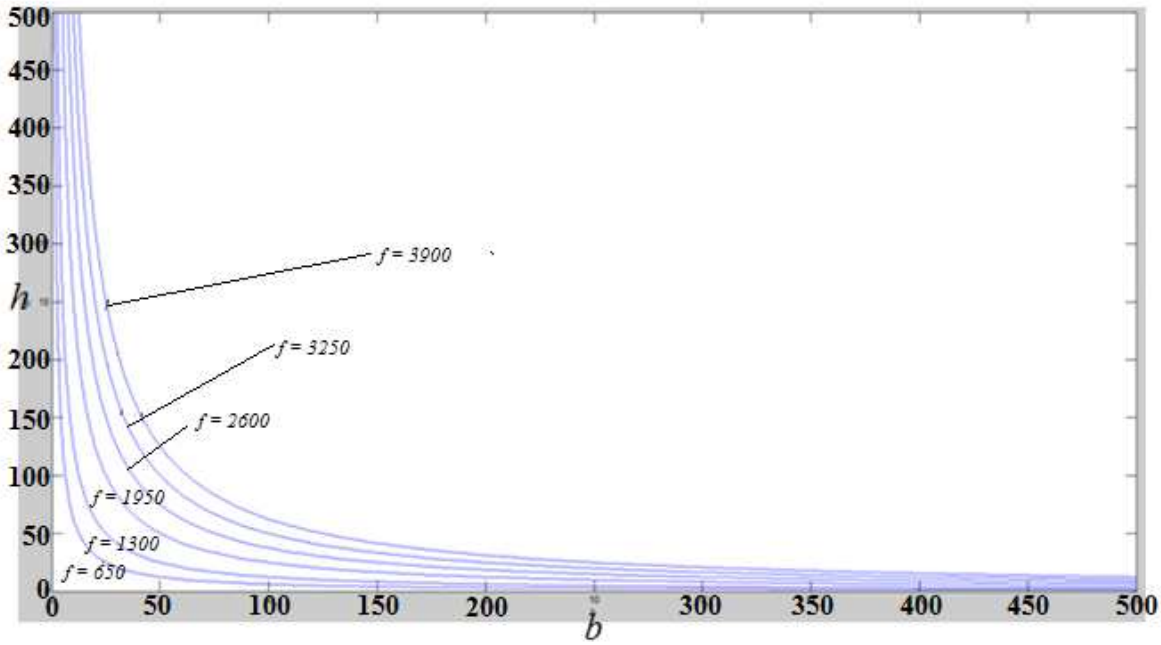

Figure 4.12: several curves of the performance function $b * h = f$, in which every hyperbole has a constant value of *f*.

On the other hand, Fig. 4.13 shows (highlighted in magenta) the limit-state function *g(b,h)=0*.

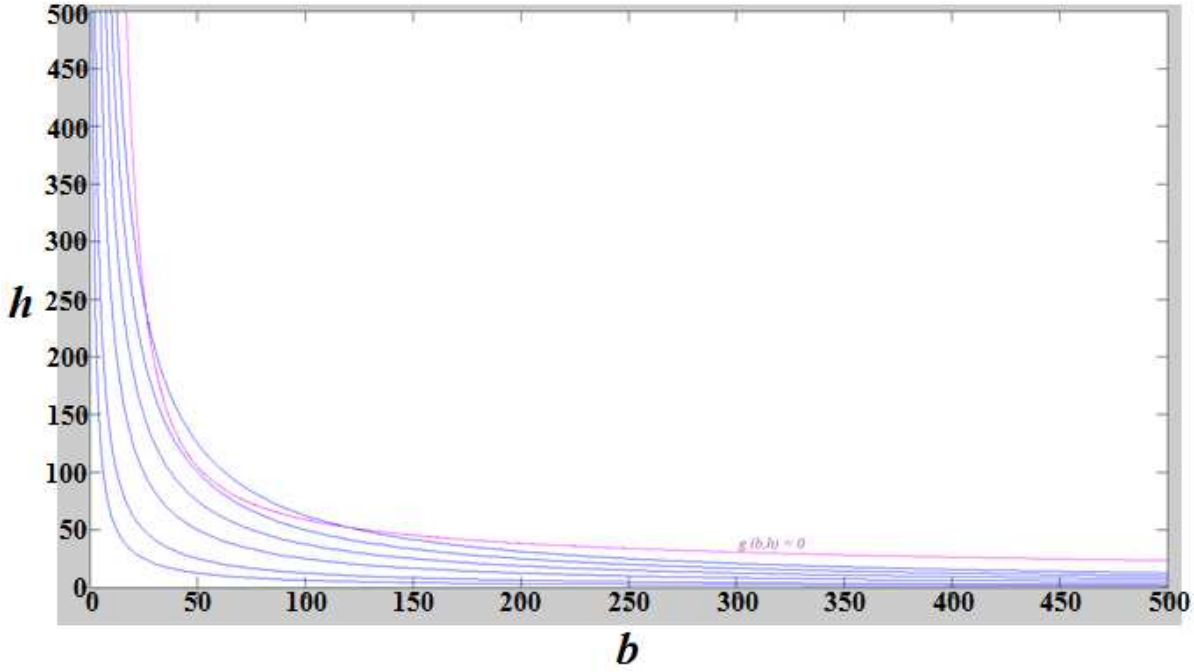

Figure 4.13: limit-state function *g(b,h)=0* (in magenta) and several objective functions (in blue).

Figure 4.13 shows that the performance function curve potentially intersects more than one objective curves.

This means that the limit-state function follows a path that potentially continues to change "altitude", according to every of its particular couple of coordinates *(b,h)*. Therefore, the optimal value for the objective function along the limit-state function is reached at the point having the minimum *f* value, which corresponds also to the tangency point with the connected objective function itself (see Fig. 4.14).

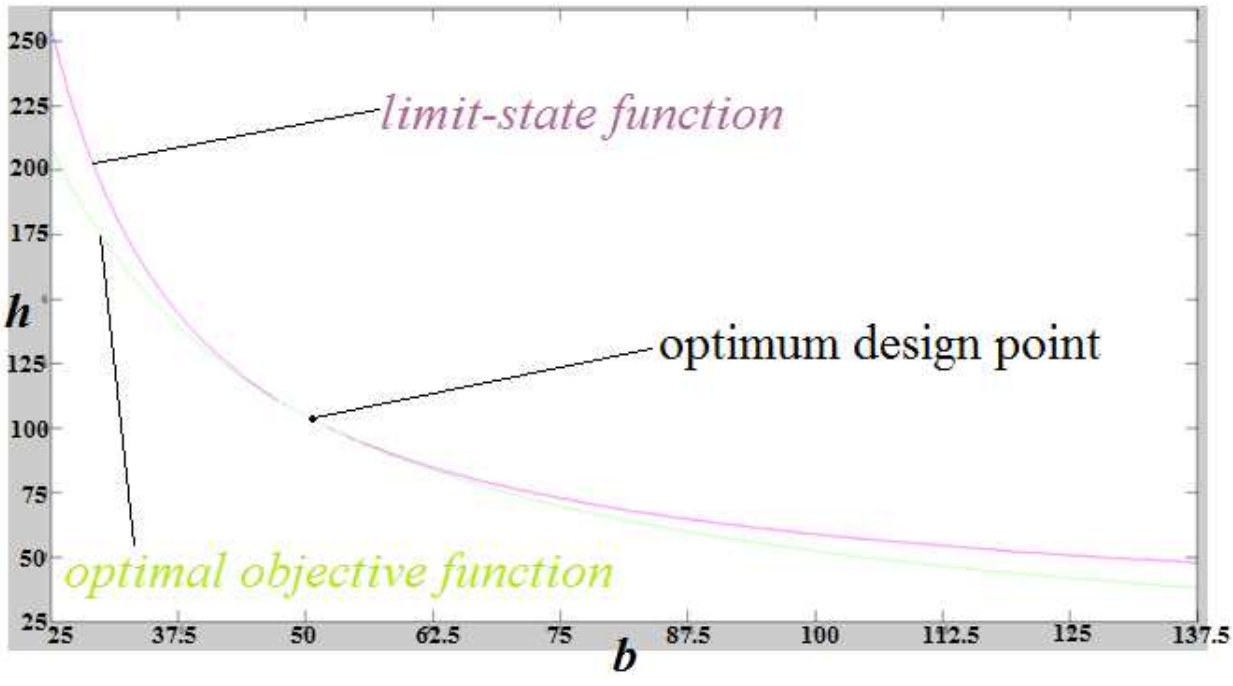

Figure 4.14: The green curve represents the optimal objective function, i.e. the only one that is tangent to the limit-state function (coloured in magenta).

To better understand the separation between the admitted and the forbidden regions, let's have a tridimensional look to the objective function and to the performance function (see Figures 4.15 and 4.16).

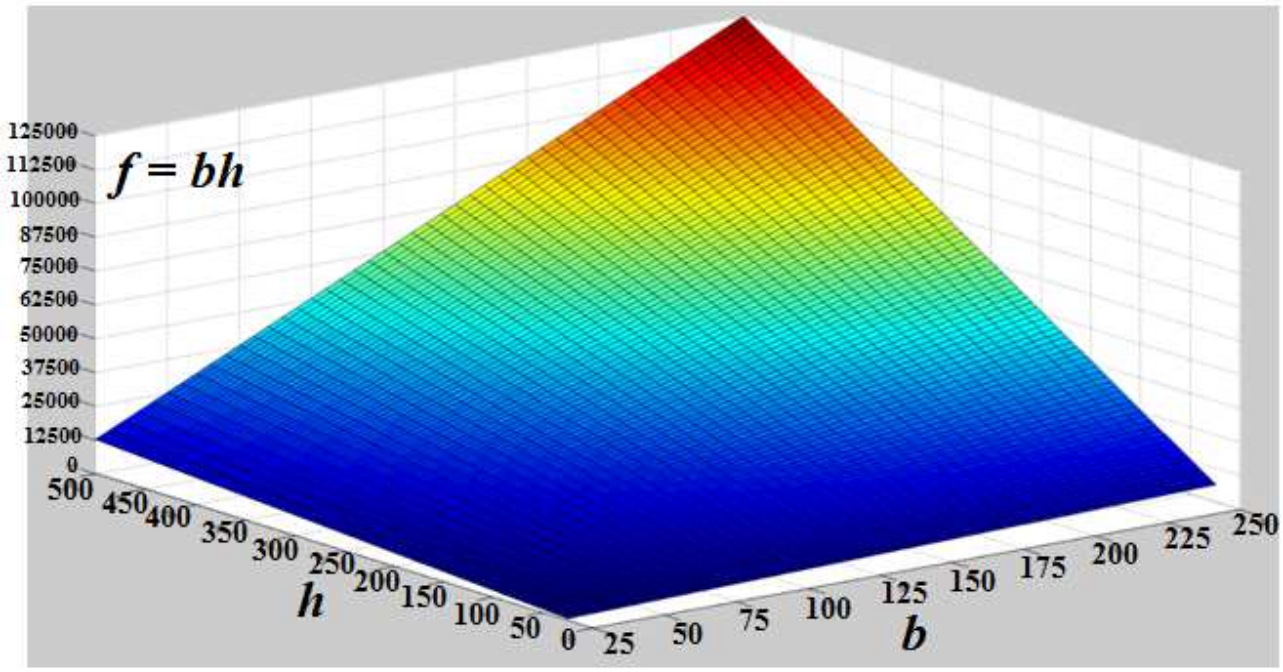

Figure 4.15: The objective function $f = b * h$ increases for increasing values of b and h.

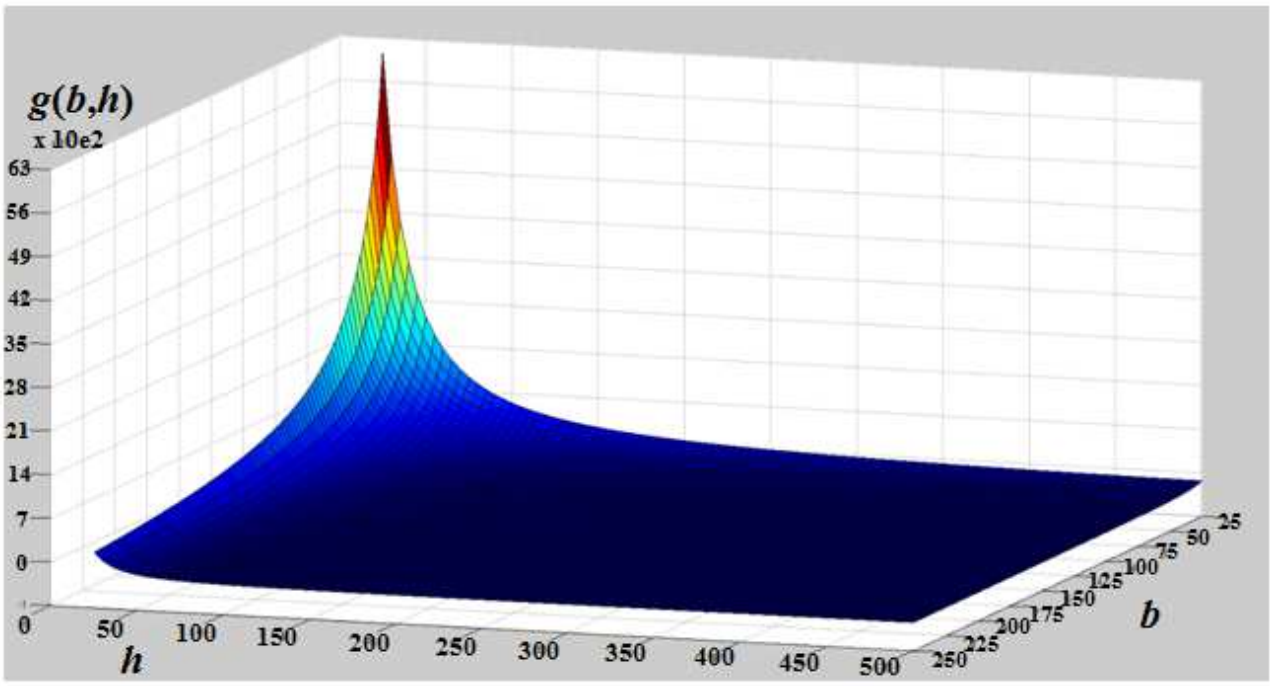

Figure 4.16: The performance function *g(b,h)* sharply increases while getting closer to the origin.

Let us look for the optimal values of *b* and *h*. Considering the expressions for the two curves in figure 4.14:

$$\begin{cases} g(b,h) = S - \dfrac{6*L}{b*h}\left(\dfrac{X}{b} + \dfrac{Y}{h}\right) = 0 \\ f = b*h = const = c \end{cases} \tag{4.7}$$

From the second expression of the system:

$$h = \frac{c}{b} \tag{4.8}$$

And, by inserting such a value in Eq. (4.7), one obtains the expression of the limit-state function as a function of *b* as the only variable:

$$g = S - \frac{6*L}{b*\dfrac{c}{b}}\left(\frac{X}{b} + \frac{Y*b}{c}\right) = 0 \tag{4.9}$$

Then,

$$S*b*c^2 - 6*L*X*c - 6*L*Y*b^2 = 0 \tag{4.10}$$

The equation is now expressed as a second-degree polynomial of the only variable *b*:

$$b^2 - \frac{S*c^2}{6*L*Y}*b + \frac{Xc}{Y} = 0 \tag{4.11}$$

The law to find the two solutions is

$$b_{1,2} = \frac{\dfrac{S*c^2}{6*L*Y} \pm \sqrt{\left(\dfrac{S^2*c^4}{36*L^2*y^2} - \dfrac{4*X*c}{Y}\right)}}{2} \tag{4.12}$$

But, remembering that there is only one solution (tangency), the term $\sqrt{\left(\dfrac{S^2*c^4}{36*L^2*y^2} - \dfrac{4*X*c}{Y}\right)}$ (i.e. the so-called Δ) is necessarily equal to zero. Hence,

$$\Delta = 0 \Rightarrow \sqrt{\left(\frac{S^2*c^4}{36*L^2*y^2} - \frac{4*X*c}{Y}\right)} = 0 \tag{4.13}$$

From the last expression, it is possible to determine the value of $c = f$:

$$c = \sqrt[3]{\frac{144 * L^2 * X * Y}{S^2}} = 5404.07 \tag{4.14}$$

From equations (4.12) and (4.14), it is possible to find that

b_{opt} = *51.981*

And, recalling that $h = \frac{c}{b} = \frac{f}{b}$,

h_{opt}= 103.963 *mm*

These results confirm the validity of the optimal point that was found using the gradient-based method.

Further improving the objective function

The value of the performance function at the optimal point that was found earlier is

g(b,h) = g(51.981 *mm*, 103.962 *mm*) = *0*

Several points along the optimal objective function were chosen in the neighbourhood of the point that was found to be the optimal one (both by the graphical method and by *fmincon*), in order to see if there was any couple of coordinates *(b,h)* having a greater value of the performance function, i.e. farther to the limit condition and therefore "safer".

It was found that, if b = 51.841 *mm*,

$$h = \frac{f_{opt}}{b} = \frac{5404.07}{51.841} = 104.24mm$$

and

*g(b,h)=g(*51.841,104.24*)* = 40.27 > 0

For less than truncation errors, this last point would be safer than the point that was found earlier, i.e. (51.981, 103.962), for which the performance function is zero.

Notice that, in this last case, $\frac{b}{h} = \frac{51{,}841}{104.24} = 0.4973 \neq \frac{1}{2}$

4.4. Conclusions

In the present chapter, an introduction to optimization was made, which, together with reliability assessment, constitutes the basis for the comprehension and the implementation of Reliability-Based Design Optimization, as it will be hereinafter seen. Anyway, for the purposes of this chapter, purely deterministic optimization was examined. In a structural design, the objective of optimization is to find the optimal values of a set of design variables such that a certain (or more than one) performance is maximized, while respecting some predefined feasibility constraints. The most elementary problems, which can be expressed through a very simple mathematical form and which involve a limited number of design variables, can be solved in an analytical or a graphical way. Apart from these rare cases, optimization is carried on via numerical methods, the most popular ones being *gradient-based methods* and *Genetic Algorithms*. A couple of applicative examples have then been examined. In the first one, the objective was to optimize the ratio between the performances and the dimensions of a wing airfoil; to do so, a gradient-based method was used. In this application, such an algorithm proved to be susceptible to the value of the starting point: indeed, convergence to the global optimal solution is attained only if the starting point is located inside a precise subset of the design variable space allowed region. The second applicative example concerns the geometrical sizing of a cantilever beam, in order to minimize its mass while accounting for the constraint on the material yield stress. This time, the gradient-based method converged to the global optimum, and its stability was proved by varying the initial beam geometry and the values of the forces acting on its tip. The exactness of the solution was also proved via graphical optimization, with whom the same optimal point was found. In conclusion, it was verified that gradient-based methods not always converge, and are generally strongly dependent on the choice of the starting point.

Chapter 5

Reliability-Based Design Optimization

5.1. Introduction

In Chapter 4, deterministic optimization was treated; this methodology is used to minimize or maximize an objective function *f*, while maintaining design constraints; however, it doesn't incorporate uncertainties, and thus may result in risky or conservative designs (see Fig. 5.1). *Reliability-Based Design Optimization* (RBDO) is a methodology that considers uncertainty during the design process. Uncertainty is due to the presence of *random parameters*, i.e., those random variables which cannot be controlled by the designer (Du X., 2006). The need to obtain a trade-off between a higher safety and a lower cost is normally satisfied by fixing a minimum required reliability *R*, or a maximum allowed probability of failure p_f for each of the constraints, the latter being expressed through a set of n_p probabilistic performance functions g_i.

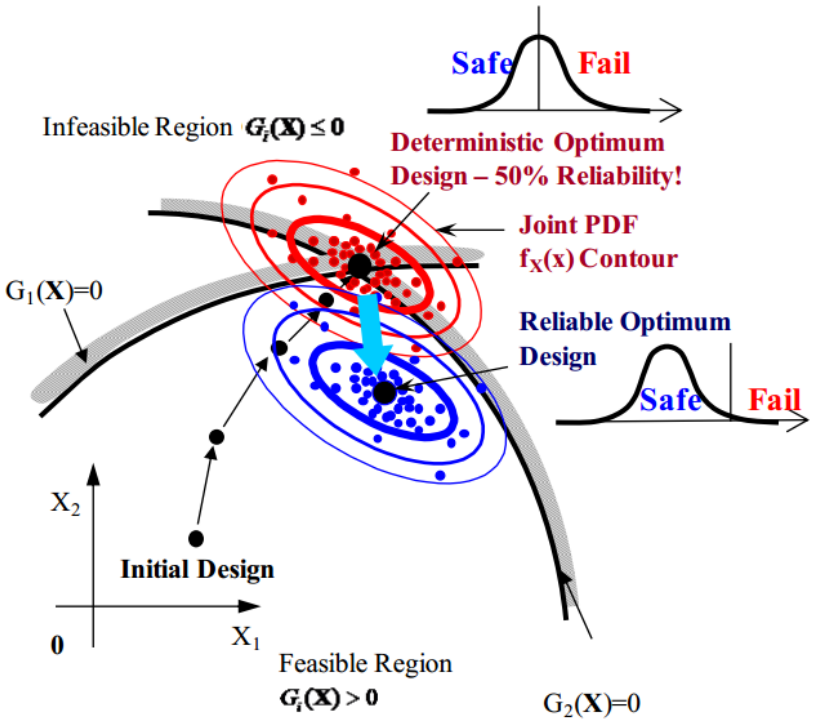

Figure 5.1: comparison between deterministic optimization and Reliability-Based Design Optimization (from R. Haftka, 2010).

The analytical formulation of the problem is

$$\begin{cases} Minimize\ f(\boldsymbol{d}, \boldsymbol{\mu_X}) \\ subject\ to \\ Pr\{g_i(\boldsymbol{d}, \boldsymbol{X}) \leq 0\} \geq R_i,\ i = 1,2,\dots,n_p \\ g_j(\boldsymbol{d}) \leq 0,\ j = 1,2,\dots,n_d \\ d_k^l \leq d_k \leq d_k^u,\ k = 1,2,\dots,n \end{cases} \tag{5.1}$$

where g_i are the probabilistic constraints, R_i are their related required reliabilities, g_j are the deterministic constraints, and $\boldsymbol{\mu_X}$ is the vector of the mean values of random variables $\boldsymbol{X}$; d_k^l and d_k^u are, respectively, the lower and the upper bound for each of the n design variables $\boldsymbol{d} = (d_1, d_2, \dots, d_n)$.

To solve a RBDO problem, a reliability analysis loop is nested into an external optimization loop (see Fig. 5.2). In the outer loop, the optimum search is executed. After every iteration of the optimization algorithm, the inner loop uncertainty analysis is performed to evaluate the design safety, which is normally based either on Monte Carlo Simulation (MCS) or on Reliability Methods (i.e., FORM or SORM). Due to its trade-off between efficiency and accuracy, FORM method is often preferred.

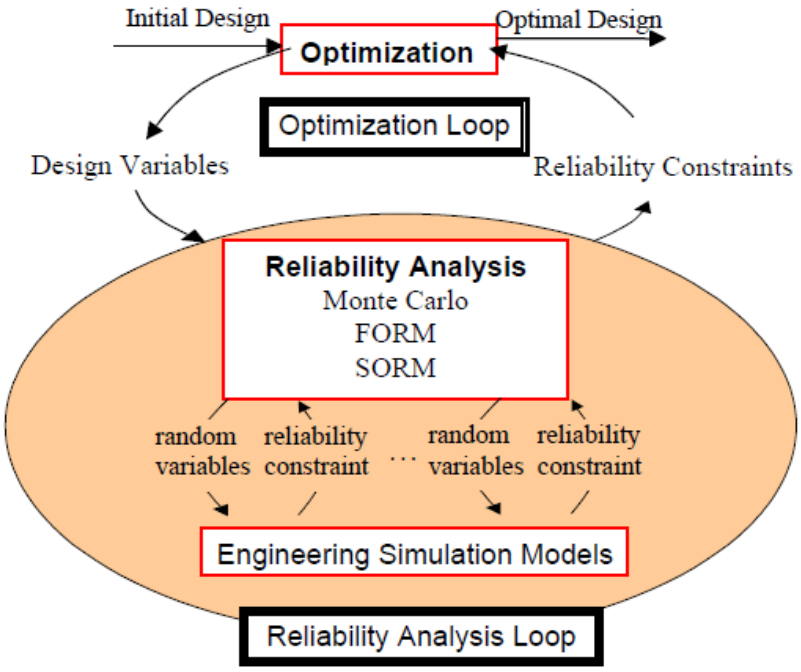

Figure 5.2: General scheme of the double loop-procedure for Reliability-Based Design Optimization (from Du X., 2006).

Equation (5.1) refers to the case of *Direct Reliability-Based Design*; in such a model, the the actual reliability of each reliability constraint is evaluated (Du, 2006), and FORM method is normally used. For every probabilistic constraint, the Most Probable Point is located by using the following model, which is analogous to that of Eq. (3.18):

$$\begin{cases} \min \beta_i = min|U_i| \\ s.t. \\ g_i(\boldsymbol{d}, U_i) = 0 \end{cases} \tag{5.2}$$

in which the coordinate system $\boldsymbol{U}$ refers to the standard normal random variables (namely, after Rosenblatt transformation). The solution of Eq. (5.2) is the MPP $\boldsymbol{u_i^*}$ or, equivalently, the reliability index β_i. The corresponding reliability is given by

$$Pr[g_i(\boldsymbol{d}, \boldsymbol{X}) \leq 0] = \Phi(\beta_i) \tag{5.3}$$

However, the computational efficiency of *Direct Reliability-Based Design* model is limited, mainly due to the necessity to compute the probability of failure for each of the reliability constraints $g_i(\boldsymbol{d}, \boldsymbol{X})$. Moreover, some of the probabilistic constraints may have very high reliabilities, which will never be critical during the optimization process; nevertheless, the evaluations of their reliabilities will unfortunately dominate the computational effort in the RBD process (Du, 2006). Furthermore, direct reliability analysis exposes to the risk of singularity problems.
To work out such an issue, one can set a priori a minimum required reliability, rather than computing it a posteriori: by doing this, the reliability assessment is performed only to the necessary level, i.e., just enough to meet the design requirements. For this purpose, *Inverse Reliability-Based Design* was introduced. In this model, the probabilistic constraints-based formulation is substituted with the concept of *percentile performance function*. Recalling Eq. (3.51) (but reversing the signs, in order to improve the clarity), the percentile value g^{p_f} which corresponds to the target p_f is

$$Pr[g(\boldsymbol{X}) \geq g^{p_f}] = p_f \tag{5.4}$$

or, equivalently,

$$Pr[g(\boldsymbol{X}) \leq g^{R}] = R \tag{5.5}$$

The latter equation means that the probability, for the performance function, to be less or equal to the *R*-percentile performance function g^R is equal to the *target reliability R*, which is equal to the area in magenta in Fig. 5.3.

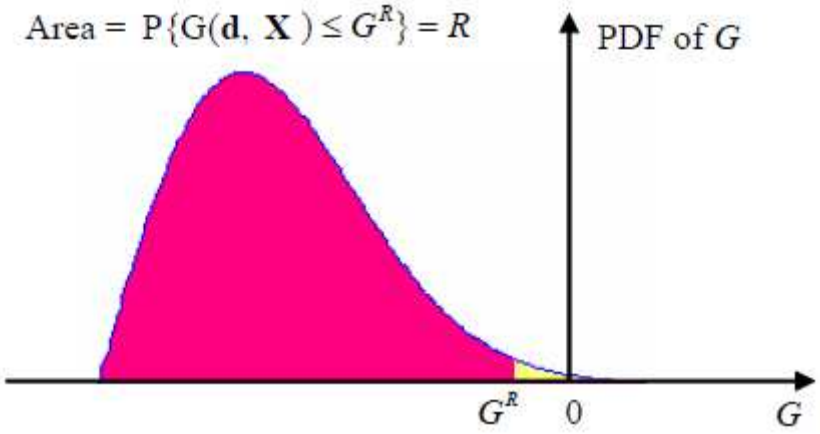

Figure 5.3: graphical expression of an *R*-percentile performance function from Du X., 2006).

In other words, in the Inverse Reliability-Based Design approach, the probabilistic constraints are transformed into *R*-percentile performance functions that have to be satisfied. Therefore, rather than computing the actual reliability $Pr[g_i(\boldsymbol{d}, \boldsymbol{X}) \leq 0]$, the location of g^R will determine whether the probabilistic constraint are satisfied or not. The percentile constraints are expressed as

$$g^R(\boldsymbol{d}, \boldsymbol{X}) \leq 0 \tag{5.6}$$

Another advantage of this procedure is that it allows to avoid the singularity problems that can be met while performing direct reliability analysis through FORM or SORM.

A general RBDO problem implementing inverse reliability analysis can be expressed as:

$$\begin{cases} Minimize\ f(\boldsymbol{d}, \boldsymbol{\mu_X}) \\ subject\ to \\ g_i^{R_i}(\boldsymbol{d}, \boldsymbol{X}) \leq 0,\ i = 1,2,\dots,n_p \\ g_j(\boldsymbol{d}) \leq 0,\ j = 1,2,\dots,n_d \\ d_k^l \leq d_k \leq d_k^u,\ k = 1,2,\dots,n \end{cases} \tag{5.7}$$

where $R_i\ (i = 1,2,\dots,n_p)$ is the target reliability for the *i*-th percentile constraint. The percentile $g_i^{R_i}$ is determined by inverse reliability analysis, and inverse First-Order Reliability Method (iFORM) (Tu *et al.*, 1997) can be used:

$$\begin{cases} find & \boldsymbol{U} \\ min & g_i(\boldsymbol{d}, \boldsymbol{U}) \\ s.t. & \|\boldsymbol{U}\| = \beta_i \end{cases} \tag{5.8}$$

whose solution is the MPP $\boldsymbol{u_i^*}$ which, after its transformation into $\boldsymbol{x_i^*}$ in the original space, can be used to determine the value of the percentile performance function:

$$g_i^{R_i}(\boldsymbol{d}, \boldsymbol{X}) = g_i(\boldsymbol{d}, \boldsymbol{x_i^*}) \tag{5.9}$$

Therefore, the inverse RBDO analytical model of Eq. (5.7) can be expressed as

$$\begin{cases} Minimize\ f(\boldsymbol{d}, \boldsymbol{\mu_X}) \\ subject\ to \\ g_i(\boldsymbol{d}, \boldsymbol{x_i^*}) \leq 0,\ i = 1,2,\dots,n_p \\ g_j(\boldsymbol{d}) \leq 0,\ j = 1,2,\dots,n_d \\ d_k^l \leq d_k \leq d_k^u,\ k = 1,2,\dots,n \end{cases} \tag{5.10}$$

5.2. A simple RBDO algorithm

In order to examine in depth the interaction of the two contrasting goals of maximizing performances and respecting reliability constraints, an elementary Reliability-Based Design algorithm was developed; subsequently, it was applied to a simple RBDO example. The algorithm is described below.

Nomenclature:

f = objective function;

$g(\boldsymbol{X})$ = Performance function (safe if ≥ 0);

$\boldsymbol{X}$ = random variables vector;

$\boldsymbol{\mu_x}$ = vector of the mean values of the random variables;

$\boldsymbol{d}$ = vector of the design variables, which are interval variables, s.t. $d_k^l \leq d_k \leq d_k^u,\ k = 1,2,\dots,n$;

design parameters = set of specific numerical values assumed by the design variables for a particular design configuration;

$R = \phi(\beta)$ = *target reliability* corresponding to the target relaibility index β;

$P_f = \phi(-\beta)$ = *target probabilty of failure*.

The RBDO problem to be solved is the following one:

$$\begin{cases} find\ \boldsymbol{d} \\ s.t. \\ \min f(\boldsymbol{d}, \boldsymbol{X}) \\ Pr[g(\boldsymbol{d}, \boldsymbol{X}) < 0] = P_f \\ \\ d_k^l \leq d_k \leq d_k^u,\ k = 1,2,\dots,n \end{cases} \tag{5.11}$$

Step 1: deterministic optimization:

During the optimization process, the random variables are given a constant value, i.e., the value of their means, namely $\boldsymbol{X} = \boldsymbol{\mu_X}$:

$$\begin{cases} Minimize\ f(\boldsymbol{d}, \boldsymbol{\mu_X}) \\ subject\ to \\ g(\boldsymbol{d}, \boldsymbol{\mu_X}) \leq 0 \\ d_k^l \leq d_k \leq d_k^u,\ \ k = 1,2, \dots, n \end{cases} \tag{5.12}$$

As a result of optimization, the first attempt optimal design parameters are $\boldsymbol{d} = \boldsymbol{d^1}$.

Step 2: inverse reliability analysis:

In the expression of the performance function $g(\boldsymbol{X})$, the new set $\boldsymbol{d^1}$ of the design parameters is used, and the percentile performance function $g^R(\boldsymbol{d^1}, \boldsymbol{X})$ is determined by inverse First-Order Reliability Method (iFORM):

$$\begin{cases} find & \boldsymbol{U} \\ min & g(\boldsymbol{d^1}, \boldsymbol{U}) \\ s.t. & \|\boldsymbol{U}\| = \beta \end{cases} \tag{5.13}$$

whose solution is the MPP $\boldsymbol{u}^*$ which, after its transformation into $\boldsymbol{x_i^*}$ in the original space, gives the value of the percentile performance function:

$$g^R(\boldsymbol{d^1}, \boldsymbol{X}) = g_i(\boldsymbol{d^1}, \boldsymbol{x_i^*}) \tag{5.14}$$

$g^R(\boldsymbol{d^1}, \boldsymbol{X})$ is such that

$$Pr[g(\boldsymbol{d^1}, \boldsymbol{X}) \geq g^R(\boldsymbol{d^1}, \boldsymbol{X})] = R \tag{5.15}$$

Now, let us define a new performance function, such that

$$g'(\boldsymbol{d^1}, \boldsymbol{X}) = g(\boldsymbol{d^1}, \boldsymbol{X}) + g^{\boldsymbol{R}}(\boldsymbol{d^1}, \boldsymbol{X}) \tag{5.16}$$

which equals zero when the target reliability R is reached. Compared to Eq. (3.52), a different norm for the signs is used in Eq. (5.16).

The new performance function $g'(\boldsymbol{d^1}, \boldsymbol{X})$ will be used during the next optimization cycle.

Step 3: deterministic optimization:

Again, as for each determinstic optimization cycle, the random variables are given the value of their means, i.e., $\boldsymbol{X} = \boldsymbol{\mu_X}$:

$$\begin{cases} Minimize\ f(\boldsymbol{d^1}, \boldsymbol{\mu_X}) \\ subject\ to \\ g'(\boldsymbol{d^1}, \boldsymbol{X}) \geq 0 \\ d_k^{1,l} \leq d_k^1 \leq d_k^{1,u},\ \ k = 1,2, \dots, n \end{cases} \tag{5.17}$$

As a result of the optimization loop, the optimal design parameters are updated: $\boldsymbol{d} = \boldsymbol{d^2}$, which satisfy the new constraint function, i.e., $g'(\boldsymbol{d^1}, \boldsymbol{X}) \geq 0$.

Step 4: inverse reliability analysis:

Similarly to step 2, the new values $\boldsymbol{d} = \boldsymbol{d^2}$ of the design parameters are used to update the performance function. By using iFORM:

$$\begin{cases} find & \boldsymbol{U} \\ min & g(\boldsymbol{d^2}, \boldsymbol{U}) \\ s.t. & \|\boldsymbol{U}\| = \beta \end{cases} \tag{5.18}$$

whose solution is the MPP $\boldsymbol{u}^*$ which, after its transformation into $\boldsymbol{x_i^*}$ in the original space, gives the value of the percentile performance function:

$$g^R(\boldsymbol{d^2}, \boldsymbol{X}) = g_i(\boldsymbol{d^2}, \boldsymbol{x_i^*}) \tag{5.19}$$

Now, let us introduce the updated performance function $g''(\boldsymbol{d^2}, \boldsymbol{X})$:

$$g''(\boldsymbol{d^2}, \boldsymbol{X}) = g'(\boldsymbol{d^1}, \boldsymbol{X}) + g^{\boldsymbol{R}}(\boldsymbol{d^2}, \boldsymbol{X}) \tag{5.20}$$

which equals zero when the target reliability *R* is reached.

Next steps:

As for steps 3 and 4, sequential optimization and inverse reliability loops are executed until $\boldsymbol{d^{n+1}} = \boldsymbol{d^n}$ (convergence).

5.2.1. An applicative example

To test the proposed RBDO method, let us consider the simple structure that was analyzed in section 4.3.2 (even though, in that case, only deterministic optimization was carried out). A cantilever beam with homogeneous mass density is stimulated on its tip by a pure bending forces, whose components are P_x and P_y, which are not deterministic, but follow a probabilistic normal distribution. The goal of this design problem is the beam mass minimization while guaranteeing a minimum reliability level to prevent yielding. Let us imagine the beam section being constant and rectangular, with dimensions *b* and *h*. The beam length is fixed. Thus, due to the homogeneous mass density, the objective of optimization is to minimize the cross-sectional area, i.e. *b*h*. Therefore, *b* and *h* will be the design variables which have to lie inside some predefined intervals. On the other hand, a reliability level of 99.87% is required, which corresponds to a reliability index $\beta = 3$, i.e. to a cumulative distribution function $\Phi = 3\sigma$. This constraint is satisfied by respecting the probabilistic constraint function *g* on the maximum allowable stress at the fixed end of the beam.

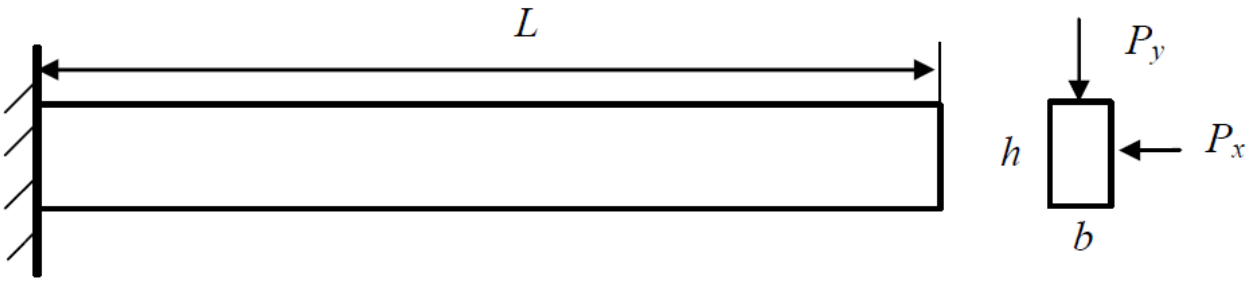

Figure 5.4: cantilever beam subjected to a pure bending force on its tip.

Problem data:

L = 2540 mm;

$b^l = 25.4\,mm \leq b \leq 254\,mm = b^u$;

$h^l = 25.4\,mm \leq h \leq 508\,mm = h^u$;

$\boldsymbol{d} = (b, h)$ = vector of the design variables;

$f = objective\ function = \min b \cdot h$;

$P_x \approx (2227, 445.4)\ N$ (force acting along x direction);

$P_y \approx (4454, 445.4)\ N$; (force acting along y direction);

$\boldsymbol{X} = (P_x, P_y) = (X, Y)$ = vector of the random variables;

μ_x, μ_y= mean values of the random variables;

σ_x, σ_y= standard deviations of the random variables;

β = 3 (required reliability index);

S = 241.3 MPa (yield strength of the material);

The constraint is expressed as the performance function $g(P_x, P_y)$; from a deterministic point of view, this function has to be negative, i.e. the acting stress has not to overtake the yield stress S of the material.

$$g(\boldsymbol{d}, \boldsymbol{X}) = g(P_x, P_y) = \frac{6L}{bh}\left(\frac{P_x}{b} + \frac{P_y}{h}\right) - S \leq 0 \tag{5.21}$$

Before executing inverse reliability analysis, the normal random variables will be transformed into standard normal variables through Rosenblatt transformation; hence, the performance function becomes:

$$g(U_x, U_y) = \frac{6L}{b*h}\left(\frac{\mu_x + \sigma_x * U_x}{b} + \frac{\mu_y + \sigma_y * U_y}{h}\right) - S \leq 0 \tag{5.22}$$

Such a constraint has to be respected with the required 99.87% level of reliability (i.e., β = 3) or, equivalently, with a maximum 0.13% probability of failure.

To summarize, the reliability-based optimization problem is given by:

$$\begin{cases} find\ b, h \\ s.t. \\ \min b \cdot h \\ Pr[g(\boldsymbol{d}, \boldsymbol{X}) > 0] = P_f \\ b^l \leq b \leq b^u \\ h^l \leq h \leq h^u \end{cases} \tag{5.23}$$

The first step consists of performing an optimization cycle through a routine employing the gradient-based method. During the inverse reliability analysis that follows (performed through iFORM method), the most probable point corresponding to the target reliability *R* is found, which will be used to update the *constraint function* that will be employed during the subsequent further optimization cycle. The optimization–inverse reliability analysis sequence continues till convergence is reached. During each deterministic optimization cycle, P_x and P_y will be considered constant and equal to their average values, i.e., μ_x and μ_y. For a greater clarity, P_x and P_y will be henceforth called as *X* and *Y*.

Step 1: deterministic optimization

The gradient-based method is run by using a numerical routine, and the chosen algorithm follows the *interior point method*. A starting point for the optimization process is required, which is set to (*b*,*h*) = (50.4, 50.4) *mm*.

The first optimization cycle provides the following results:

(b_1, h_1) = (52.0055, 104.011) *mm*

Objective function = $f = b \cdot h = 5409.14\ mm^2$

The optimization outputs are the new values of *b* and *h*; their product, *b*h*, which has to be minimized, is the *objective function*, (also called *fitness function* or *obj*). The new values of *b* and *h*, namely, b_1 and h_1, are used to update the *constraint* function *g* that will be used during the *inverse reliability analysis* cycle that follows.

The objective of the inverse reliability analysis cycle is to find out the value of the performance function that corresponds to the desired reliability, i.e., the *percentile function* g^R (in the present example, $g^R = g^{99.87\%}$).

Step 2: inverse Reliability Analysis cycle:

Inverse reliability analysis is executed in order to guarantee the needed 99.87% reliability. For computational reasons, the additive inverse of the performance function will be used during inverse reliability analysis, and it will be indicated as $-g$. Starting from equation (5.21), updating the limit-state function with the new values of b and h that were obtained through optimization, and finally changing the sign in the equation in order to perform inverse Reliability Analysis, one gets:

$$-g(X,Y) = S - \frac{6L}{b_1 h_1}\left(\frac{X}{b_1} + \frac{Y}{h_1}\right) \tag{5.24}$$

After making Rosenblatt transformation:

$$-g(U_x,U_y) = S - \frac{6L}{b_1 h_1}\left(\frac{\mu_x+\sigma_x U_x}{b_1} + \frac{\mu_y+\sigma_y U_y}{h_1}\right) \tag{5.25}$$

And, by inserting the numerical values:

$$-g(U_x,U_y) = 241.3 - 2.82\left(\frac{\mu_x+\sigma_x U_x}{52.0055} + \frac{\mu_y+\sigma_y U_y}{104.011}\right) \tag{5.26}$$

Let us compute ∇g , $\|\nabla g\|$ and $\boldsymbol{a}$, which in this example are constant:

$$\nabla g(U_x,U_y) = \left(\frac{\partial g}{\partial U_x}, \frac{\partial g}{\partial U_y}\right) = (-24.164,-12.082)$$
$$\|\nabla g\| = 27.016 \tag{5.27}$$

$$\boldsymbol{a} = (-0.8945, -0.4472)$$

Starting by $\boldsymbol{u}_o = (0,0)$,

$g(\boldsymbol{u}_0) = -0.794$

$$\boldsymbol{u}_1 = -\beta\boldsymbol{a} = -3\boldsymbol{a} = (2.6835, 1.3417) = \boldsymbol{u}^* = (u_x^*, u_y^*) \tag{5.28}$$

Convergence to the MPP $\boldsymbol{u}^*$ is reached after only one iteration.

By making Rosenblatt Transformation backwise, one gets the values of X and Y that correspond to the limit-state case for a 99.87-percentile reliability.

The corresponding values of X and Y are

$$\begin{cases} x^* = \mu_x + \sigma_x * U_x^* = 2227 + 445.4 * 2.6835 = 3422N = x^{99.87\%} \\ y^* = \mu_y + \sigma_y * U_y^* = 4454 + 445.4 * 1.3417 = 5052N = y^{99.87\%} \end{cases} \quad (5.29)$$

In other words, $(x^*, y^*) = (x^R, y^R) = (x^{99.87\%}, y^{99.87\%})$ is the minimum force which brings to failure in the presence of a 99.87% reliability (i.e., a reliability index $\beta = 3$). As it could be forecast $X^{99.87\%}$ and $Y^{99.87\%}$ are greater than the corresponding mean values (2227 *N* and 4454 *N*, respectively).

By using $(x^*, y^*) = (x^R, y^R)$, the value of the percentile performance function is obtained:

$$g^R(\boldsymbol{d^1}, \boldsymbol{X}) = g_i(\boldsymbol{d^1}, \boldsymbol{x^*}) = g_i(b^1, h^1, x^*, y^*) = -81.39\ MPa = g^{99.87\%} = g^R \quad (5.30)$$

Now, as in Eq. (5.16), let us define the new performance function $g^I(\boldsymbol{d^1}, \boldsymbol{X})$

$$g^I(\boldsymbol{d^1}, \boldsymbol{X}) = g(\boldsymbol{d^1}, \boldsymbol{X}) - g^R(\boldsymbol{d^1}, \boldsymbol{X}) = \frac{6L}{bh}\left(\frac{\mu_x}{b_1} + \frac{\mu_y}{h_1}\right) - 241.3 + 81.39 =$$

$$= \frac{6L}{bh}\left(\frac{\mu_x}{b_1} + \frac{\mu_y}{h_1}\right) - 159.91 \quad (5.31)$$

Compared to Eq. (5.16), a different norm for the signs was used for $g^R(\boldsymbol{d^1}, \boldsymbol{X})$ in the last equation.

Step 3: deterministic optimization:

Compared to the previous optimization cycle, this one differs for the new value of $g^R = g^{99.87\%}$, that in the first optimization was necessarily equal to zero, the value of initialization.

The corresponding expression for the performance function is now given by Eq. (5.31). The second optimization cycle was run by using *fmincon* function, with (b_1, h_1) = (52.0055, 104.011) *mm* as starting values, and with $g^I(\boldsymbol{d^1}, \boldsymbol{X}) = \frac{6L}{bh}\left(\frac{\mu_x}{b_1} + \frac{\mu_y}{h_1}\right) - 159.91$ as updated limit-state function.

This further optimization gives the following output values for the design parameters:

(b_2, h_2) = (59.568, 119.136) *mm*, and

$f = obj = b_2 \cdot h_2 = 7096.7\ mm^2$.

Next steps:

The optimization-reliability assessment sequence is performed repeatedly until the following criteria are satisfied:

$\left|\frac{b_{n+1} - b_n}{b_{n+1}}\right| < 10^{-4}$, and (5.32)

$$\left|\frac{h_{n+1}-h_n}{h_{n+1}}\right| < 10^{-4} \tag{5.33}$$

These criteria result to be satisfied after the 11^{th} iteration, and the resulting geometry is

$b = 57.31\ mm;$

$h = 114.61\ mm.$

Hence, the objective function (i.e., the cross-sectional area) is

$f = obj = b \cdot h = 6568.3\ mm^2.$

Assessing the reliability with FORM and MCS

In order to verify whether the output of the last optimization cycle respects the reliability requirement of β = 3 (and, hence, R = 0.9987), a direct reliability analysis cycle is performed with First Order Reliability Method (FORM). It is important to remember that the new performance function, i.e. $-g^I = -\left(g(\underline{X}) - g^R\right)$, equals zero when reliability R is 99.87%. If (U_x, U_y) converges to (0,0), this requirement will be satisfied.

Indeed, if $(U_x, U_y) = (0,0)$, then $\beta^I = \left\|(U_x, U_y)\right\| = 0$; $\beta^I = \sigma = 0$ corresponds to the mean value, μ (see figure 7).

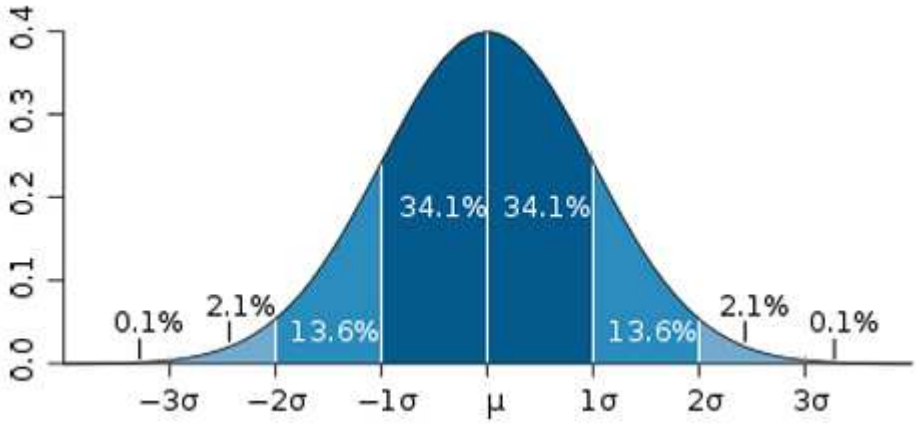

Figure 5.5: standard normal distribution.

Performing the reliability analysis, FORM method effectively converges at $(U_x, U_y) = (0,0)$: thus, convergence is reached.

To confirm the dependability of the results, the reliability of the structure was computed via Monte Carlo Simulation (MCS) too. After 10^6 iterations, the reliability-based design outputs resulted to be verified, with an error of 0.48% on the desired 99.87% reliability.

Comments

The outputs of the RBDO method were compared to the geometrical parameters relative to both the deterministic optimization and the initial configuration, and are reported in Table 5.1. Even though the reliable optimum would appear a bit less high performance than the deterministic optimal solution, the latter does not have the desired level of reliability, which, by definition, is equal to 50%.

	$\boldsymbol{b}$	$\boldsymbol{h}$	$\boldsymbol{f = b \cdot h}$	**Reliability**
Initial configuration	$50.80\ mm$	$50.80\ mm$	$2581\ mm^2$	$<< 50\%$
After deterministic optimization	$52.006\ mm$	$104.011\ mm$	$5409\ mm^2$	50%
After probabilistic optimization	$57.31\ mm$	$114.61\ mm$	$6568.3\ mm^2$	99.87%

Table 5.1: design parameters (*b* and *h*) and objective function *f* related to the initial configuration, the deterministic optimization (see chapter 4) and probabilistic optimization.

The utilization of different solving algorithms (i.e. *trust-region reflective*, *active-set* or *sequential-quadratic programming*) does not change the outputs of the optimization cycles.

About the reciprocal correlation between the two section edges *b* and *h*, the reason for the fixed *b/h* ratio (equal to 2) was explained from a physical point of view. While performing RBDO, a *numerical* reason for the constancy of this ratio can be highlighted: it is due to the constancy of ∇g, $\|\nabla g\|$ and $\boldsymbol{a}$.

5.3. Reliability Index Approach and Performance Measure Approach

To solve complex RBDO problems, it is better to resort to some of the best-established methods, which supply an high level of both computational efficiency and reliability. Two main approaches are used to carry out RBDO: Reliability Index Approach (RIA) and Performance Measure Approach (PMA) (see Fig. 5.6), which are often based on First Order Reliability Method (FORM). The reliability index β associated with the limit state function g_i is defined as the distance from the origin to the most probable point (MPP) of the failure surface in the standard normal space (see Fig. 5.6) (Frangopol D.M. et al., 2014). While RIA employs direct reliability analysis for assessing the probability of failure, PMA is based on inverse reliability analysis.

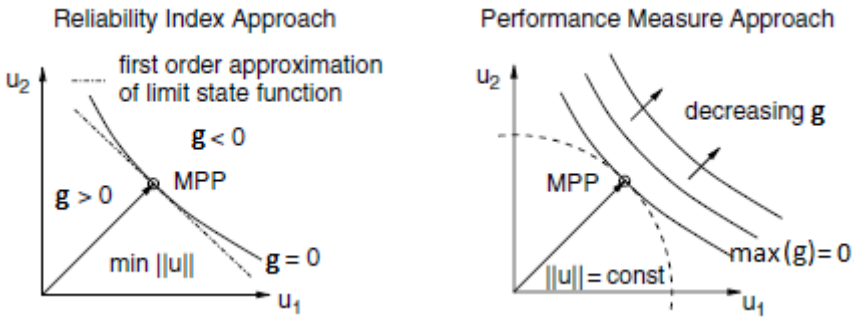

Figure 5.6: Comparison between Reliability Index Approach and Performance Measure Approach.

The RIA method computes the probability of failure by the reliability index; it aims to minimize $\|u\| = \beta$, i.e. to find the reliability index which corresponds to $g_i(\boldsymbol{X}) = 0$ (i.e., the failure surface). Being $\boldsymbol{u}$ = $\boldsymbol{u}[\boldsymbol{d}(\boldsymbol{X})]$ the vector of the design variables (which are function of the random variables), the RBDO problem (5.1) using RIA can be defined as

$$\begin{cases} Minimize\ f(\boldsymbol{d}, \boldsymbol{\mu_X}) \\ subject\ to \\ \beta_{m,i} - \beta_i \leq 0,\ i = 1,2,\dots,n_p \\ g_j(\boldsymbol{d}) \leq 0,\ j = 1,2,\dots,n_d \\ d_k^l \leq d_k \leq d_k^u,\ \ k = 1,2,\dots,n \end{cases} \tag{5.34}$$

where $\beta_{m,i}$ is the minimum required reliability index for the *i*-th *probabilistic constraint*, and $g_j(\boldsymbol{d})$ is the *j*-th *deterministic constraint*.
Anyway, it can not be guaranteed that the RIA optimization problem has a solution for any given design during the design-optimization process (Frangopol D.M. et al., 2005). Indeed, in some cases there may be no solution $\boldsymbol{u}$ such that $g_i = 0$ (i.e, on the failure surface).

A very efficient alternative to RIA for performing RBDO is the Performance Measure Approach (PMA). For a given target reliability index β_t, the maximum value for the limit state function is computed by solving the following optimization problem in the standard normal space $\boldsymbol{u}$:

$$\begin{cases} \max g_i(\boldsymbol{u}) \\ s.t. \\ (\boldsymbol{u}^T\boldsymbol{u})^{\frac{1}{2}} - \beta_t = 0 \end{cases} \tag{5.35}$$

The value of the limit state function at the optimum of formulation (5.35) represents the worst possible performance for a *required reliability index* β_t (Frangopol D.M. et al., 2005).Compared to the RIA approach, the constraint in eq. (5.35) can always be satisfied.

A general RBDO problem implementing PMA is given by

$$\begin{cases} find\ \boldsymbol{d} \\ s.t.\ Min\ f(\boldsymbol{d};\boldsymbol{\mu_X}) \\ g_i^{P_{f,i}}(\boldsymbol{d};\boldsymbol{X}) \le 0,\ \ i = 1,2,\dots,n_p \\ g_j(\boldsymbol{d}) \le 0,\ j = 1,2,\dots,n_d \\ d_k^L \le d_k \le d_k^U,\ k = 1,2,\dots,n \end{cases} \tag{5.36}$$

where $g_i^{P_{f,i}}$ is the $P_{f,i}$-th percentile value for the *i*-th performance function g_i, i.e.

$$P\left[g_i^{P_{f,i}}(\boldsymbol{d},\boldsymbol{X}) \ge 0\right] = P_{f,i}$$

in which $P_{f,i}$ is the corresponding target probability of failure. The percentile $g_i^{P_{f,i}}$ can be determined by inverse reliability analysis, and inverse First-Order Reliability Method (iFORM) (Tu et al., 1997) is often used.

PMA is numerically more efficient and stable than RIA.

5.4. Conclusions

In this chapter, the theoretical basics of Reliability-Based Design Optimization (RBDO) were presented. The aim of RBDO is to maximize a given performance (optimization) while guaranteeing a minimum, predefined, level of reliability. To manage such conflicting goals, one has to deal with an external optimization loop and an internal reliability assessment loop. The achievement of the desired safety level in reliability-based design can be pursued via two alternative ways, namely, direct reliability analysis and inverse reliability analysis. The first case is referred as *Direct Reliability-Based Design*, and an algorithm which employs such a methodology is the *Reliability Index Approach* (RIA). On the other hand, the second case is called *Inverse Reliability-Based Design*, and is based on setting a minimum, predefined reliability level; such a methodology is employed by the *Performance Measure Approach* (PMA) algorithm. Inverse Reliability-Based Design has generally proved to be more stable and less computational demanding than Direct Reliability-Based Design. An elementary Inverse Reliability-Based Design algorithm was developed, in which optimization and reliability analysis loops are executed sequentially, and the latter is performed via *inverse First Order Reliability Method* (iFORM). This algorithm was applied to the design of a cantilever beam which is subject to perpendicular forces (subject to gaussian distribution) acting on its tip. The objective was to minimize the beam mass, while respecting the probabilistic constraint on the maximum acting stress with a 99.87% reliability, which corresponds to a reliability index β = 3. The RBDO outputs were the geometrical dimensions of the structure which fulfill the problem requirements; to confirm the reliability of such a configuration, MCS was used, which verified the results, with an error of 0.48% on the required reliability.

Chapter 6

RBDO of aeronautical structures

6.1. Introduction

In chapter 5, a theoretical introduction to Reliability-Based Design Optimization was made, with a particular emphasis from an analytical and numerical point of view. In the present chapter, the stress will be on the particular kind of application; the systems that will be presented are concerned with aeronautic structural applications. To begin with, the probabilistic structural design of a wing airfoil (considered as a part of a rectangular wing) was made, with the aim of minimizing the wing mass and preventing aeroelastic instabilities; In order to combine both the simultaneous needs for optimizing the structure and attaining the desired levels of reliability on the probabilistic constraints, the airfoil structural design is performed via a double-loop RBDO algorithm. Here, the reliability assessment is performed by inverse reliability analysis (inner loop), which is nested into the optimization process (outer loop). The probabilistic optimization is then extended to a three-dimensional case involving a rectangular wing, in which the probabilistic constraints concern both the wingtip displacement and the maximum allowable stress (at the wing root); in this application, Genetic Algorithms (GA) will be used for performing the optimization. Subsequently, the reliability-based design will be performed on the main shear web of a tapered wing, which is subject to an elliptical lift distribution. The spirit of these simulations is to come to an ever increasingly realistic approach on the probabilistic design of a wing.

6.2. Probabilistic optimization based on elastic axis [1]

In the present paper, a probabilistic optimization approach to the structural design of an airfoil is described. Such an activity is to be considered as the first step towards the structural design of a high aspect ratio, flexible wing. The structure modeling of the latter is based on the work done by Cesnik and Brown (2002) and Brown (2003), in which the wing is analyzed as a one-dimensional beam experiencing three-dimensional bending and twisting deformations, whereas the extensional and shear deformations are considered as negligible (see Appendix D). In order to highlight the forces that originate from random gusts, the theory of Peters *et al.* (1994) and Peters *et al.* (1995) will be followed when the analysis will be extended to the three-dimensional case. To consider the present application, the deterministic optimization scheme introduced by Huo *et al.* (2013) is described in Appendix E, which stresses the importance of the elastic axis position in the aeroelastic stability of a wing; this is valid also for a two-dimensional case. After having verified that the divergence instability is more likely to occur for high values of the distance between the aerodynamic center and the elastic axis, such a distance was considered by Huo *et al.* (2013),

[1] Partly based on: Coccon, Menegozzo and Galvanetto, 4th Royal Aeronautical Society Aircraft Structural Design Conference, Conf. Proc., 7th-9th October, 2014, Belfast, Northern Ireland.

together with the wing mass, to define the design objective function which has to be minimized. This work inspired the definition of the objective function in the study that is proposed in the present section, in which a reliability assessment is integrated inside the optimization process. The reliability-based design is carried out by means of a Performance Measure Approach (PMA) (Frangopol *et al.*, 2005, and Tu *et al.*, 1999), which uses inverse First Order Reliability Method (iFORM) to evaluate the probabilistic constraints on the maximum allowable strain and stress over the wing span. To solve this kind of problems, the use of sampling-based methods (e.g., Monte Carlo Simulation) is not suitable, because they require a very high computational effort. Conversely, the proposed algorithm represents a good compromise between precision requirements and computational costs. Even though the development of this optimization procedure is still in progress, some preliminary results are presented, limited to the design of a single airfoil.

6.2.1. RBDO of a wing airfoil

The goal of this probabilistic design is to minimize its cross-sectional area, together with the distance between the aerodynamic center and the shear center. The thicknesses of the shear webs and their position along the chord are considered as design variables. The constraint functions concern the minimum allowable values for bending stiffness and twisting stiffness, and the target reliability index β is set to one, which corresponds to a target probability of failure of 15.87%.
As it was proved by Huo *et al.* (2013, see Appendix E), the divergence dynamic pressure q_D on a wing is expressed as

$$q_D = \frac{k_\theta}{eS(\partial C_L/\partial \alpha)} \tag{6.1}$$

where k_θ is the twist elastic coefficient, e is the distance between the elastic axis (EA) and the aerodynamic center (AC), S is the wing surface area, C_L is the lift coefficient, and α is the airfoil angle of attack, which is the sum of the initial angle of attack, α_0, and the twist angle, θ. From Eq. (6.1), one deduces that, for increasing values of e, divergence instability is more likely to occur. Hence, the location of the elastic axis has a direct impact on the wing divergence velocity.

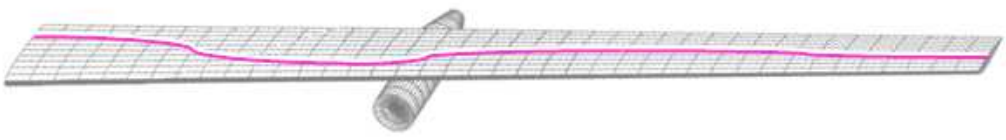

Figure 6.1: optimization design based on elastic axis.

In their work, Huo *et al.* (2013) set the wing mass and the distance between the elastic axis and the aerodynamic center as the two objective functions, which define the following global fitness function f:

$$f = \frac{W_1 M}{M_{max}} + \frac{W_2 e}{c} \tag{6.2}$$

where M is the wing mass after optimization, M_{max} is the maximum wing mass in the design variable interval, c is the cross section chord, whereas W_1 and W_2 are the weight coefficients. The deterministic optimization process described above can be extended to a RBDO analysis, where the fitness function in Eq. (6.2) is minimized while considering the uncertainties introduced by the randomness on the material properties as well as on the aerodynamic loads (random gusts). In the present section, a reliability-based methodology is proposed for the optimization of the high-aspect ratio wing model of Appendix D, and some preliminary results are presented, limited to a wing section, and considering the material properties only as the random variables.

The structure of the wing cross-section is sketched as a thin walled structure with a single cell closed section, composed by two horizontal skins and two vertical shear webs (see Fig. 6.2).

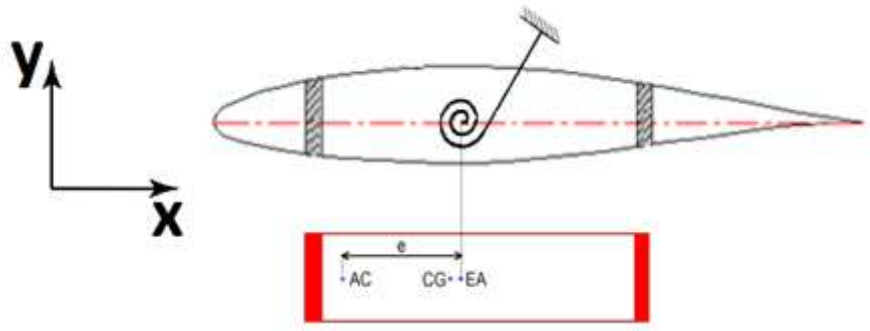

Figure 6.2: Simplified structural model of the wing cross section (from Coccon, Menegozzo and Galvanetto, 2014).

For the sake of simplicity, the material properties are assumed to be uniform over the section (from Coccon, Menegozzo and Galvanetto, 2014) and the wing is hypothesized to be rectangular. Moreover, it is assumed that the aerodynamic center, AC, lies on the vertical axis of the left shear web (even if, in Fig. 6.2, AC is not exactly positioned in that location, for the sake of clarity) and is horizontally aligned with the center of gravity, CG, and the elastic axis, EA (see Fig. 6.2).

The physical characteristics to be minimized are the wing cross sectional area (which is representative of the wing mass) and the distance between the AC and EA, here indicated with A and e, respectively. The objective function expression is analogous to Eq. (6.2), and the weight coefficients are chosen such that $W_1 = W_2 = 0.5$:

$$f = 0.5\left(\frac{A}{A_0}\right) + 0.5\left(\frac{e}{e_0}\right) \tag{6.3}$$

where A_0 and e_0 are the values of A and e before optimization. As it can be noticed, the numerical value of the objective function f is initially equal to 1, and it decreases after the optimization process. However, the presence of reliability constraints could limit such a decrement. Three design

variables are considered, i.e. the thicknesses of the two shear webs, t_2 and t_3, and their mutual distance, *l*.

The thickness t_1 of the (horizontal) skin, on the other hand, has a constant value of 2 *mm*. The starting configuration is reported in Table 6.1.

Table 6.1: Initial configuration and bounds of the wing cross section design variables (from Coccon, Menegozzo and Galvanetto, 2014).

Parameters	Value [*mm*]	Bounds [*mm*]
t_2	*8*	*5-15*
t_3	*15*	*10-25*
l	*500*	*350-600*

In this model, the uncertainty is due to the incomplete knowledge of the material properties: the Young modulus, *E*, and the shear modulus, *G*, are assumed to follow a normal distribution with mean values μ_E = *71700 MPa*, μ_G = *26900 MPa* (Al 7075-T6) and a standard deviation equal to 10% of the mean values. It should be noticed that the values of *A* and *e* are not influenced by the random variables *E* and *G*, therefore the objective function only depends on the design variables: $f = f(t_2, t_3, l)$.

However, the random variables *E* and *G* are introduced in the constraints, which establish the minimum required values for the section bending and twisting stiffnesses, i.e., $K_{B,min}$ = *120 N/mm* and $K_{T,min}$ = *1.6x10^6 N/mm*. The section is located at a distance $L = 3000\ mm$ from the wing root.

The expressions for the bending and twisting stiffness are, respectively:

$$K_B = \frac{3EJ_x}{L^3}$$

$$K_T = \frac{4A^2G}{\left[L \cdot \left(\frac{2H}{t_3} + \frac{2H}{t_2} + \frac{2B}{t_1}\right)\right]}$$

where J_x is the section moment of inertia with respect to the *x* axis (see Fig. 6.2), which is function of the cross-section geometric features.

The corresponding performance functions are defined by the difference

$$g_i(t_2, t_3, l; E, G) = K_{i,min} - K_i(t_2, t_3, l; E, G), \quad i = \{B, T\} \tag{6.4}$$

where *B* = *bending* and *T* = *twisting*.

With regard to the PMA scheme of Eq. (5.34), the constraint equations are based on the $P_{f,i}$-th percentile, $g_i^{P_{f,i}}$, of the performance function g_i. For both these constraints, a required reliability index $\beta = 1$ is set, that corresponds to a target probability of failure $P_f = \Phi(-\beta_i) = 15.87\%$.

The mathematical model of the present RBDO implementation is given by

$$\begin{cases} find & t_2, t_3, l \\ min & f(t_2, t_3, l) \\ s.t. & g_i^{P_f}(t_2, t_3, l; E, G) \geq 0\,, \quad i = \{B, T\} \\ & t_2^L \leq t_2 \leq t_2^U \\ & t_3^L \leq t_3 \leq t_3^U \\ & l^L \leq l \leq l^U \end{cases} \tag{6.5}$$

6.2.2. Analysis of the results

Along with the implementation of such a RBDO problem, the equivalent deterministic problem was also solved, which was obtained from Eq. (6.5), by replacing the probabilistic constraints $g_i^{P_f}(t_2, t_3, l; E, G) \geq 0$ with deterministic performance functions, i.e. $g_i(t_2, t_3, l; \mu_E, \mu_G) \geq 0$. The results of both these approaches are reported in Table 6.2.

Table 6.2: Comparison between the deterministic optimization design and the proposed RBDO approach (from Coccon, Menegozzo and Galvanetto, 2014).

Parameters	Initial configuration	After deterministic optimisation	After the proposed RBDO
To be minimised			
f (objective function)	1.000	0.7632	0.9272
$A\,[\boldsymbol{mm^2}]$	5450	4987	5440
$e\,[\boldsymbol{mm}]$	217.0	132.6	185.8
Related to the probabilistic constraints			
$\boldsymbol{K_B}[\boldsymbol{N/mm}]$	141.2	120.0	141.0
$\boldsymbol{K_T}[\boldsymbol{N/mm}]$	$\boldsymbol{1.91 \times 10^6}$	$\boldsymbol{1.95 \times 10^6}$	$\boldsymbol{1.84 \times 10^6}$
Design variables			
$\boldsymbol{t_2}[\boldsymbol{mm}]$	8.0	5.0	5.0
$\boldsymbol{t_3}[\boldsymbol{mm}]$	15	18.1	17.9
$\boldsymbol{l}[\boldsymbol{mm}]$	500.0	380.8	500.0

As shown in Table 6.2, the deterministic approach provides a better optimization, thus resulting in a lower value of the performance function f : indeed, both the cross-sectional area (A) and the distance between the aerodynamic center and the elastic axis (e) are smaller than those obtained by

RBDO. The main effect of such a difference on the two resulting designs is that deterministic optimization produces a definitely shorter distance l between the shear webs. Although the deterministic design looks more performant, it does not meet the reliability requirements on the minimum bending stiffness. This fact was demonstrated by carrying out a series of crude Monte Carlo Simulation (MCS) analyses, which assessed the reliabilities of both the designs. Such results are reported in Table 6.3, which shows the probabilities of failure and the corresponding reliability indexes of the constraint functions for bending and twisting stiffness. Only the reliability-based design guarantees a probability of failure $P_f < 15.87\%$ (or equivalently, a reliability index $\beta > 1$) for both the constraints, whereas the probability for the deterministic design to have a bending stiffness lower than *120 N/mm* is equal to *50.0%*.

Table 6.3: probabilities of failure for the deterministic and the reliability-based design, assessed via MCS method (from Coccon, Menegozzo and Galvanetto, 2014).

Probabilistic constraints	After deterministic optimisation		After the proposed RBDO	
	p_f	β	p_f	β
$K_{B,min} - K_B$	50.0%	0.0000	6.8%	1.4909
$K_{T,min} - K_T$	3.6%	1.8384	9.8%	1.2930

6.3. Analysis of a three-dimensional, rectangular wing

Let us consider a RBDO problem, in which a high aspect ratio (AR), rectangular wing is involved, the goal being its mass minimization.

In a first approximation, the wing cross-section is considered to be constant over the whole length. The wing can be schematized as a thin-walled, cantilever beam with rectangular section, as depicted in Figure 6.3.

To act in favour of safety, the lift was considered as concentrated at the wingtip. The acting drag, on the other hand, was considered as negligible.

The constraints concern the maximum allowable displacement and the maximum acting stress.

Two cross sections were taken into account, corresponding to the following locations:

- the root, where the maximum Von Mises stress is reached;

- the wingtip, which corresponds to the maximum vertical deflection.

As for the uncertainty term, the vertical force F (lift) and the Young modulus E were chosen as probabilistic variables. Due to the absence of drag, the thickness t of the front and the rear shear

web was considered to be the same, and it was considered as an interval design variable. The other two design variables are the shear webs height, *H*, and their distance, *B*.

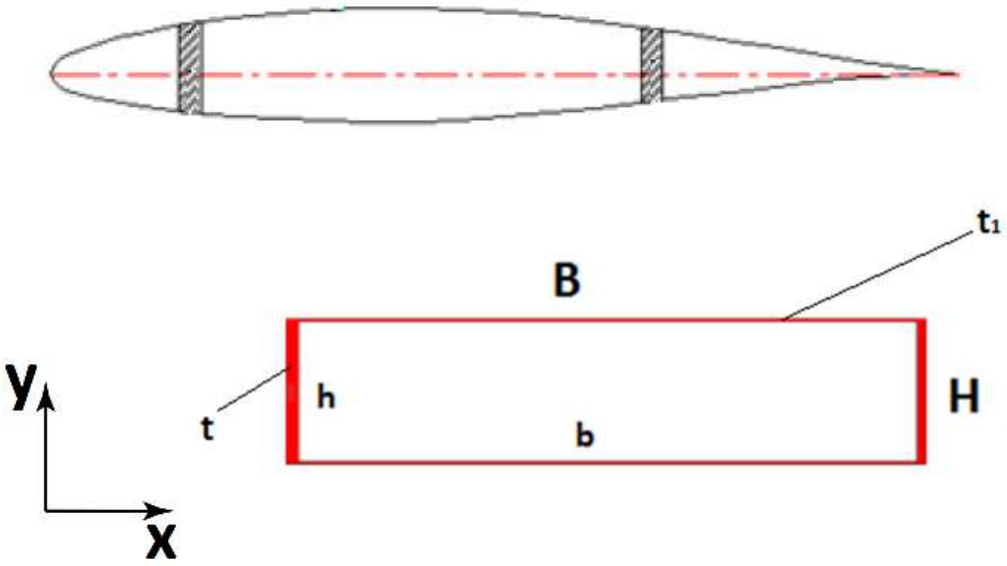

Figure 6.3: the wing cross-section and its schematization.

The Al7075-T6 aluminium alloy was chosen as material.

Problem data:

B = external distance between the two shear webs;

$t_1 = 2$ mm (thickness of the horizontal skins);

H = shear webs height, or external distance between the two horizontal skins;

L = 4000 mm (wing length);

$\rho = 2810 \frac{kg}{m^3}$ (Material: Al7075-T6);

t = thickness of each of the two shear webs;

b = B-2**t* = internal distance between the two shear webs.

h = H - 2*t_1: internal distance between the two horizontal skins;

Design variables:

$$[t_{min}, t_{max}] = [0.1, 20]\ mm$$

$$[H_{min}, H_{max}] = [100, 200]\ mm$$

$$[B_{min}, B_{max}] = [300, 700]\ mm$$

Random variables:

F = N (1000, 100) N (lift);

E = (71700, 7170) MPa;

Now, let us consider the 99.87-percentile most critical value for the acting force *F*, which corresponds to its mean value plus three standard deviations. On the other hand, the 99.87-percentile most critical value for the Young's modulus *E* corresponds to its mean value minus three standard deviations. Then, the worst values for both *F* and *E* are chosen, in order to consider the worst case, i.e.,

- $F = \mu_F + 3 * \sigma_F$ = 2600 N;
- $E = \mu_E - 3 * \sigma_E$ = 50190 MPa;

that is, both *F* and *E* assume the 99.87-percentile most critical value.

Thus, the probabilistic problem can be treated as deterministic.

Analytical model

The minimum ratio between the semi-wing lenght *L* and the "chord" *B* is

$$\frac{L}{B_{max}} = \frac{4\ m}{0.7\ m} \cong 5.71 > 5$$

Therefore, the wing can be treated as a slender beam.

The equation of the beam vertical deflection is

$$\delta = \frac{FL^3}{3EI} = \frac{4 * FL^3}{E * (BH^3 - bh^3)}$$

Let us establish that the maximum allowable beam deflection is δ_{lim}= 100 mm. Therefore, the first constraint is

$$\delta - \delta_{lim} \leq 0 \rightarrow \frac{4*FL^3}{E*(BH^3-bh^3)} - \delta_{lim} \leq 0 \qquad (6.6)$$

The mass of the semi-wing is given by

$$m = \rho L(BH - bh) = \rho L[BH - (B - 2t)h] \tag{6.7}$$

Let us now determine the axial stress at the constraint.

The section moment of inertia with respect to x direction is

$$I_{XX} = \frac{1}{12}[BH^3 - bh^3] = \frac{1}{12}[BH^3 - (B - 2t) * h^3]$$

$$W_{XX} = \frac{I_{XX}}{\left({}^{H}/_{2}\right)} = \frac{1}{6H}[BH^3 - (B - 2t) * h^3]$$

Hence,

$$\sigma_{ROOT} = \frac{M_X}{W_{XX}} = \frac{F * L}{W_{XX}} = \frac{6 * F * L * H}{[BH^3 - (B - 2t) * h^3]}$$

Let us fix a limit value for the axial stress σ_{lim}= 100 MPa (even though it is well lower than the yield stress of the material). Therefore, the second constraint is

$$\sigma_{ROOT} - \sigma_{lim} \leq 0 \rightarrow \frac{6*F*L*H}{[BH^3-(B-2t)*h^3]} - \sigma_{lim} \leq 0 \tag{6.8}$$

The formulation for this kind of problem is the following:

$$\begin{cases} find\ (t, B, H) \\ s.t. \\ \min(m) \\ g_1(t, B, H) \leq 0 \\ g_2(t, B, H) \leq 0 \\ t^l \leq t \leq t^u \\ B^l \leq B \leq B^u \\ H^l \leq H \leq H^u \\ F = \mu_F + 3 * \sigma_F \\ E = \mu_E - 3 * \sigma_E \end{cases} \tag{6.9}$$

6.3.1. Genetic Algorithm-based optimization using the most critical values of the random variables

A GA-based optimization algorithm has then been applied to solve the problem that was set up in Eq. (6.9).

This kind of GA doesn't require a starting point. This fact reduces the risk of convergence to local (and not global) or false maxima, which, on the other hand, often occurs when gradient-based algorithms are used, due to their dependency on the starting point.

The optimization algorithm gives:

t = 0.1006 mm;

H = 189.93 mm;

B = 649.20 mm;

The related objective function is:

m = 29.61 kg.

6.3.1.1. Simplifying the performance function with Response surface Methodology

Now, the next thing to do is to reduce the computational effort by simplifying and linearizing the formulation of the two constraint functions (6.6) and (6.8), through the use of surrogate models, which are supplied by Response Surface Methodology (RSM, see Appendix F). Such a simplification is not essential in this example, since the constraint functions are elementary as they are, but it is very useful when one is dealing with complex problems or with Finite Element Modeling (FEM).

The original performance functions are now substituted with the surrogate models.

In order to achieve a greater clarity, the interval variables are renamed as follows:

$$X_1 = t, \qquad X_2 = H, \qquad X_3 = B$$

First performance function surrogate model

As for the first constraint, it involves each of these three variables. Therefore, the surrogate expression for performance function g_1 can be stated in the following form:

$$Y_1^{exp} = \beta_0 + \beta_1 * X_1' + \beta_2 * X_2' + \beta_3 * X_3' \tag{6.10}$$

where

$$X_i' = \frac{2(X_i - X_{i,min})}{X_{i,max} - X_{i,min}} - 1 \tag{6.11}$$

Only the extreme values of each of the interval variables will be here considered.

As for the first surrogate performance function, the DOE matrix is

Table 6.4: DOE matrix related to g_1.

Experiment no.	X_1'	X_2'	X_3'	Y_i^{EXP}
1	-1	-1	-1	381.56 mm
2	-1	-1	+1	164.00 mm
3	-1	+1	-1	92.97 mm
4	-1	+1	+1	40.09 mm
5	+1	-1	-1	189.54 mm
6	+1	-1	+1	114.25 mm
7	+1	+1	-1	29.98 mm
8	+1	+1	+1	21.03 mm

Now, let us determine the values of the β_i coefficients:

$$\beta_0 = \frac{1}{8}\sum_{1}^{8} Y^{exp,i} = 129.18$$

$$P_{1+} = \frac{1}{4}(Y_5^{EXP} + Y_6^{EXP} + Y_7^{EXP} + Y_8^{EXP}) = 88.7$$

$$P_{1-} = \frac{1}{4}(Y_1^{EXP} + Y_2^{EXP} + Y_3^{EXP} + Y_4^{EXP}) = 169.66$$

$$E_1 = P_{1+} - P_{1-} = -80.96$$

$$\beta_1 = \frac{E_1}{2} = -40.48$$

$$P_{2+} = \frac{1}{4}(Y_3^{EXP} + Y_4^{EXP} + Y_7^{EXP} + Y_8^{EXP}) = 46.02$$

$$P_{2-} = \frac{1}{4}(Y_1^{EXP} + Y_2^{EXP} + Y_5^{EXP} + Y_6^{EXP}) = 212.34$$

$$E_2 = P_{2+} - P_{2-} = -166.32$$

$$\beta_2 = \frac{E_2}{2} = -83.16$$

$$P_{3+} = \frac{1}{4}(Y_2^{EXP} + Y_4^{EXP} + Y_6^{EXP} + Y_8^{EXP}) = 84.84$$

$$P_{3-} = \frac{1}{4}(Y_1^{EXP} + Y_3^{EXP} + Y_5^{EXP} + Y_7^{EXP}) = 173.51$$

$$E_3 = P_{3+} - P_{3-} = -88.67$$

$$\beta_3 = \frac{E_3}{2} = -44.34$$

Therefore, the surrogate expression of the first performance function is

$$Y^1 = 129.18 - 40.48 * X_1' - 83.16 * X_2' - 44.34 * X_3' \quad (6.12)$$

Then, after substituting X_i' with X_i,

$$Y^1 = 530.44 - 4.068 * X_1 - 1.663 * X_2 - 0.2218 * X_3 \quad (6.13)$$

Second performance function surrogate model:

Now, let us consider the second performance function (eq.(4)).

Here, each of the three interval variables appear, too (i.e., $X_1 = t,\ X_2 = H$ and $X_3 = B$).

The surrogate performance function can be expressed in the following form:

$$Y_2^{exp} = \beta_0 + \beta_1 * X_1' + \beta_2 * X_2' + \beta_3 * X_3' \quad (6.14)$$

where

$$X_i' = \frac{2(X_i - X_{i,min})}{X_{i,max} - X_{i,min}} - 1 \quad (6.15)$$

In this case, the DOE matrix is

Table 6.5: DOE matrix related to g_2.

Experiment no.	X_1'	X_2'	X_3'	Y_i^{exp}
1	-1	-1	-1	179.54 MPa
2	-1	-1	+1	77.17 MPa
3	-1	+1	-1	87.49 MPa
4	-1	+1	+1	37.72 MPa
5	+1	-1	-1	89.18 MPa
6	+1	-1	+1	53.76 MPa
7	+1	+1	-1	28.21 MPa
8	+1	+1	+1	19.79 MPa

Now, let us determine the values of the β_i coefficients:

$$\beta_0 = \frac{1}{8}\sum_{1}^{8} Y^{exp,i} = 71.61$$

$$P_{1+} = \frac{1}{4}(Y_5^{EXP} + Y_6^{EXP} + Y_7^{EXP} + Y_8^{EXP}) = 47.74$$

$$P_{1-} = \frac{1}{4}(Y_1^{EXP} + Y_2^{EXP} + Y_3^{EXP} + Y_4^{EXP}) = 95.48$$

$$E_1 = P_{1+} - P_{1-} = -47.74$$

$$\beta_1 = \frac{E_1}{2} = -23.87$$

$$P_{2+} = \frac{1}{4}(Y_3^{EXP} + Y_4^{EXP} + Y_7^{EXP} + Y_8^{EXP}) = 43.30$$

$$P_{2-} = \frac{1}{4}(Y_1^{EXP} + Y_2^{EXP} + Y_5^{EXP} + Y_6^{EXP}) = 99.91$$

$$E_2 = P_{2+} - P_{2-} = -56.61$$

$$\beta_2 = \frac{E_2}{2} = -28.31$$

$$P_{3+} = \frac{1}{4}(Y_2^{EXP} + Y_4^{EXP} + Y_6^{EXP} + Y_8^{EXP}) = 47.11$$

$$P_{3-} = \frac{1}{4}(Y_1^{EXP} + Y_3^{EXP} + Y_5^{EXP} + Y_7^{EXP}) = 96.11$$

$$E_3 = P_{3+} - P_{3-} = -49$$

$$\beta_3 = \frac{E_3}{2} = -24.5$$

Therefore, the surrogate expression of the second performance function is

$$Y^2 = 71.61 - 23.87 * X_1' - 28.31 * X_2' - 24.5 * X_3' \quad (6.16)$$

Then, after substituting X_i' with X_i,

$$Y^2 = 241.9 - 2.399 * X_1 - 0.5662 * X_2 - 0.1225 * X_3 \quad (6.17)$$

Hence, the reliability-based optimization problem (6.9) becomes

$$\begin{cases} find\ (t, B, H) \\ s.t. \\ \min(m) \\ Y^1(t, B, H) \leq 0 \\ Y^2(t, B, H) \leq 0 \\ t^l \leq t \leq t^u \\ B^l \leq B \leq B^u \\ H^l \leq H \leq H^u \\ F = \mu_F + 3 * \sigma_F \\ E = \mu_E - 3 * \sigma_E \end{cases} \quad (6.18)$$

The optimization outputs were the following:

Design variables:

t = 0.1138 mm;

H = 191.38 mm;

B = 651.36 mm;

objective function:

m = 29.76 kg.

Comparison of the results attained with and without RSM

Let us now compare the outputs from the optimization that was carried on with the original constraint functions with the results that were achieved by using RSM.

Table 6.6: results of probabilistic design with GA: comparison between the results obtained by using the original performance functions and those obtained by using their surrogate models.

Algorithm	GA	GA with RSM
t	*0.1006 mm*	*0.1138 mm*
H	*189.93 mm*	*191.38 mm*
B	*649.20 mm*	*651.36 mm*
Mass *m* (objective function)	*29.61 kg*	*29.76 kg*

As it can be seen, the RSM-based model brings to a final result which is very close to the one obtained by using the original performance function; therefore, the surrogate model proved to be able to mimic the original constraint with a satisfactory level of precision; the fact that the mass is slightly greater is in favour of safety. The results that were obtained are relative to the case in which the random variables assume their 99.87-percentile most critical value.

Reliability assessment

The reliability can now be computed via Monte Carlo Simulation (MCS). For this case, the probability of failure p_f after 10^6 iterations is

$$p_f = 0.0059$$

i.e., 0.59 %. If this result doesn't meet the desired value, the RBDO process can be repeated iteratively by varying the intervals of the design variables, until the target reliability is reached.

6.4. Reliability-Based Design of a shear web

6.4.1. Introduction

Now, let us make the wing RBDO problem more realistic; this can be done by considering an ultralight aircraft experiencing a realistic distribution of fluidodynamic forces. A four seat, ultralight aircraft travelling at a cruise speed was considered, whose slightly tapered wings experience a quasi-elliptical lift distribution; such a distribution can be approximated, with a good level of precision, by using the Prandtl's lifting line theory; indeed, such a formulation can be applied not only to rectangular wings, but also to tapered wings. according to this approach, the lift acting on a wing of length *b* has a distribution like that depicted in Fig. 6.4.

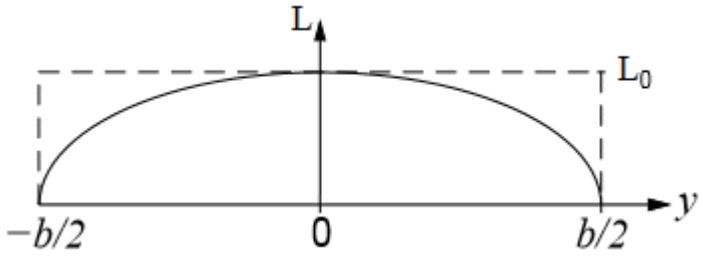

Figure 6.4: elliptical lift distribution (from M. Drela, 2009).

Let us consider a rectangular (or An elliptical spanwise circulation distribution (see Fig. 6.5) is expressed as

$$\Gamma(y) = \Gamma_0\sqrt{\left[1-\left(\frac{2y}{b}\right)^2\right]} \tag{6.19}$$

where y is the direction along the wingspan and Γ_0 is the circulation at the wing center, i.e., at $y = 0$, and b is the wingspan length.

The corresponding lift distribution per unit length is given by

$$L'(y) = \rho V_\infty \Gamma(y) \tag{6.20}$$

where ρ is the air density, and V_∞ is the free stream velocity .

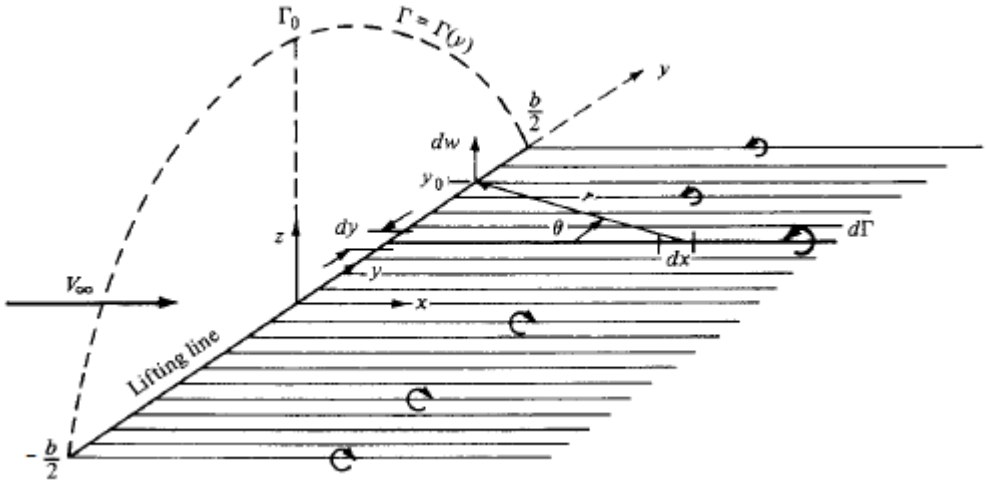

Figure 6.5: spanwise lift distribution on a lifting line (from Anderson, 2001).

Hence, the total lift acting on the wing is given by substituting Eq.(6.19) inside Eq. (6.20) and by integrating the lift per unit length $L'(y)$ along the wingspan:

$$L = \int_{-\frac{b}{2}}^{\frac{b}{2}} L'(y)dy = \int_{-\frac{b}{2}}^{\frac{b}{2}} \rho V_\infty \Gamma_0\sqrt{\left[1-\left(\frac{2y}{b}\right)^2\right]}\,dy = \frac{\pi}{4}\rho V_\infty \Gamma_0 b \tag{6.21}$$

(Drela, 2009).

Knowing that, from Eq. (6.21),

$$\Gamma_0 = \frac{4L}{\rho V_\infty b \pi}, \tag{6.22}$$

from (6.21) and (6.22), one deduces the following expression for the lift distribution:

$$L'(y) = \frac{4L}{b\pi}\sqrt{\left[1 - \left(\frac{2y}{b}\right)^2\right]} \tag{6.23}$$

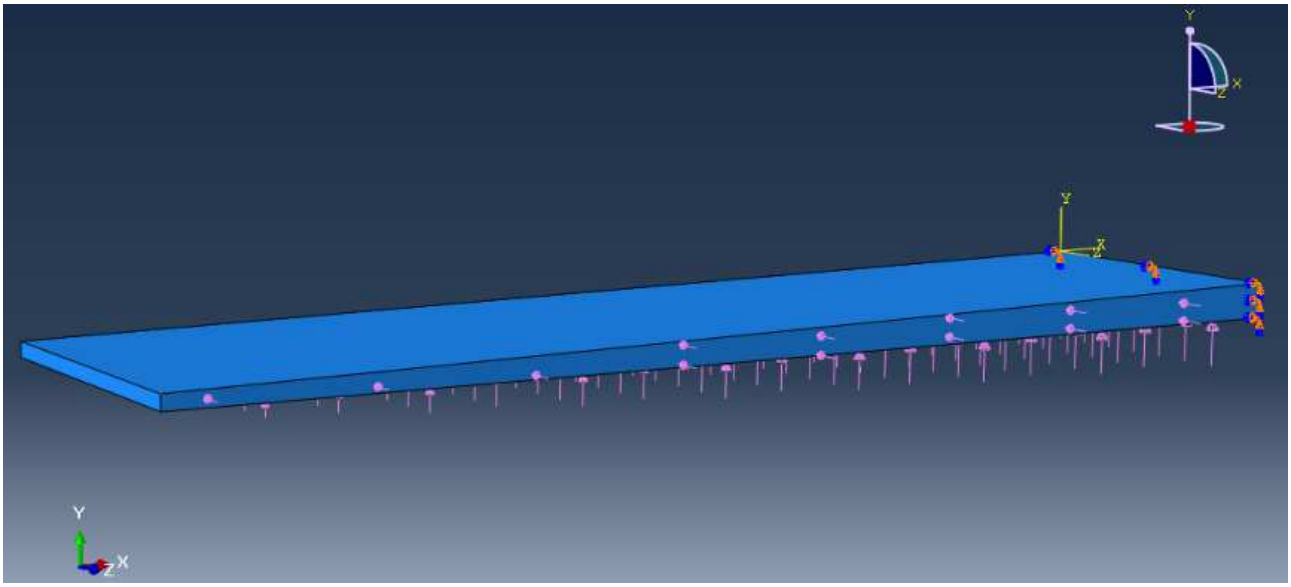

Figure 6.6: simulation of the elliptical lift distribution on a simple wing model.

Let us consider an ultralight aircraft having a maximum allowable takeoff weight of 1500 kg, which is travelling at its maximum cruise speed of 191 knots (i.e., 98.25 m/s); this plane has two slightly tapered (trapezoidal) wings, with a total wingspan of 11.00 m. Let us now hypothesize that this mass is almost all borne by the two wings (i.e., 2·700 kg), whereas only a lesser part is borne by the fuselage (100 kg).

During the cruise phase, the necessary lift that is required to the aircraft is

$$L_{TOT} = m_{TOT} g = 1500kg \cdot 9.81 \frac{m}{s^2} = 14715\ N \tag{6.24}$$

whereas each of the two wings will produce a lift amount which is equal to

$$L_{WING} = m_{WING} g = 700kg \cdot 9.81 \frac{m}{s^2} = 6867\ N \tag{6.25}$$

The lift force acting on the wing is supposed to be born entirely by the main shear web (see Fig. 6.7), which has a tapered shape; the cross-sectional dimensions (which are depicted in Fig. 6.8) are chosen as design variables:

- t_c, the thickness along the direction of the chord, which is constant along the wingspan;
- t_R, the "height" of the cross section at the wing root;
- t_T, the "height" of the cross section at the wing tip.

The design objective is to determine the shear web dimensions such that its mass is minimized, while respecting the constraint on the maximum wingtip allowed deflection (100 mm). Such a constraint is probabilistic, since some of the quantities concerned with the problem follow a normal distribution:

- the drag per unit surface, i.e., D/A_L, where L is the projection of the wing surface on the free stream direction z;
- the lift per unit surface, i.e., $L'/c(X)$, where $c(X)$ is the chord length, which assumes a different value at each position along the wingspan;
- the Young modulus of the aluminium alloy (Al7075-T6) which the shear web is composed of.

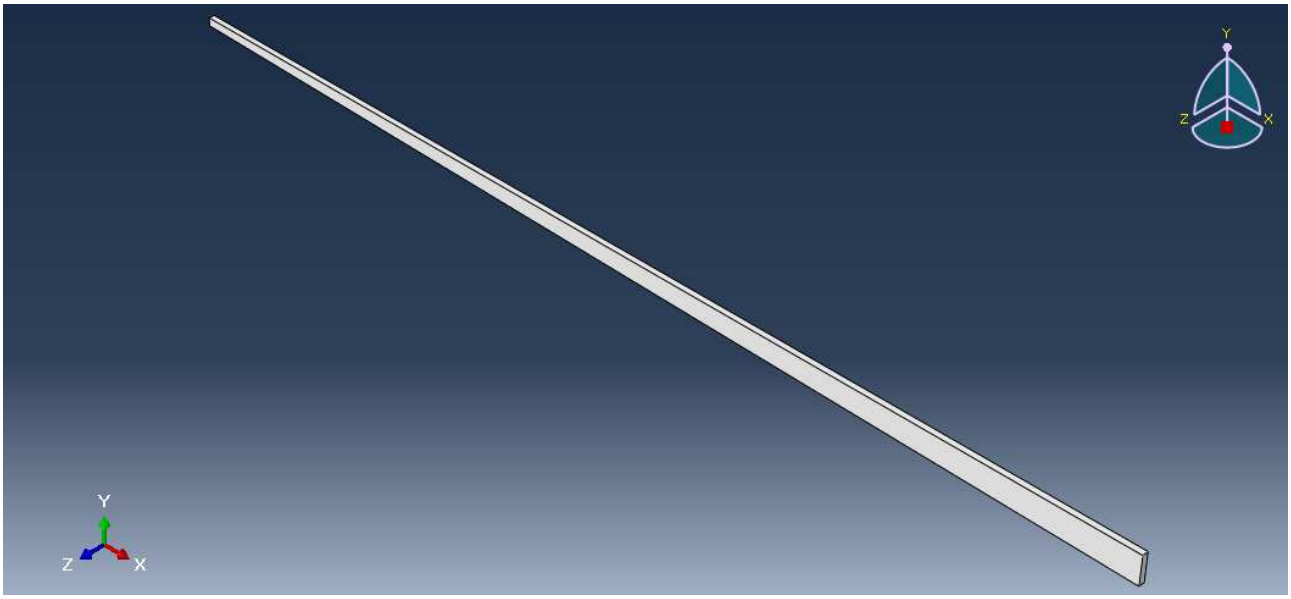

Figure 6.7: schematization of the main shear web.

Figure 6.8: shear web cross-sectional dimensions at the wing root (right) and at the wing tip (left).

6.4.2. Problem data

$\rho_{Al} = 2810\ kg/m^3$; mass density of the shear web material (Al7075-T6);

$\delta_{lim} = 100\ mm$; maximum allowed wingtip deflection;

Random variables:

$L = \mathrm{N}(6867{,}686.7)[N]$; normal distribution for the lift force which is born by a single wing;

$$=> \frac{L'}{c(X)} = \mathrm{N}\left(1300.19\sqrt{\left\{1-\left[\frac{2(\mathrm{X}-0.5)}{11}\right]^2\right\}}, 130.019\sqrt{\left\{1-\left[\frac{2(\mathrm{X}-0.5)}{11}\right]^2\right\}}\right)\left[\frac{N}{m^2}\right]; \quad (6.26)$$

$$D = \mathrm{N}(84.43{,}8.443)[N] \; => \frac{D}{A_L} = \mathrm{N}(160.82{,}8.041)\left[\frac{N}{m^2}\right]; \quad (6.27)$$

$$E = \mathrm{N}(71.7 \cdot 10^9, 7.17 \cdot 10^9)\left[\frac{N}{m^2}\right]; \quad (6.28)$$

Interval variables:

$t_R = [100, 160][mm]$;

$t_T = [40, 80][mm]$; (6.29)

$t_c = [20, 30][mm]$;

6.4.3. Setting of the problem and results

Now, let us consider the 99.87-percentile most critical value for the lift and drag, which corresponds to its mean value plus three standard deviations. On the other hand, the 99.87-percentile most critical value for the Young's modulus E corresponds to its mean value minus three standard deviations. Then, the worst values for $L'/c(X)$, D/A_L and E are chosen, in order to consider the worst case, i.e.,

- $\left.\frac{L'}{c}\right|_{3\sigma} = \mu_{\frac{L'}{c(X)}} + 3 * \sigma_{\frac{L'}{c(X)}} = \sqrt{\left\{1-\left[\frac{2(\mathrm{X}-0.5)}{11}\right]^2\right\}} \cdot (1300.19 + 3 \cdot 130.019) = 1690.25\sqrt{\left\{1-\left[\frac{2(\mathrm{X}-0.5)}{11}\right]^2\right\}}\left[\frac{N}{m^2}\right]$;
- $\left.\frac{D}{A_L}\right|_{3\sigma} = \mu_{\frac{D}{A_L}} + 3 * \sigma_{\frac{D}{A_L}} = 160.82 + 3 \cdot 8.041 = 184.94\left[\frac{N}{m^2}\right]$;
- $E_{3\sigma} = 71.7 \cdot 10^9 - 3 \cdot 7.17 \cdot 10^9 = 50.19 \cdot 10^9\left[\frac{N}{m^2}\right]$. (6.30)

that is, all these probabilistic quantities assume their 99.87-percentile most critical value.

Performance function:

To set up the problem, a mathematical expression for the performance function is needed, which describes the deflection of the tapered shear web caused by the distributed forces (see Fig. 6.9). As an analytical expression is not easy to be derived, this will be substituted by a surrogate model, which describes the system behavior with a high level of accuracy. To do so, RSM is used, in which

t_R, t_T, t_c are used as design variables for building the expression for the *surrogate constraint function Y*.

In order to achieve a greater clarity, the interval variables are renamed as follows:

$$X_1 = t_R,\ X_2 = t_T,\ X_3 = t_c \tag{6.31}$$

Only the extreme values of each of the interval variables will be here considered; for each combination of their values, a FEM simulation was run, and the *response variable* Y_i^{EXP} (i.e., the tip deflection, see Fig. 6.10) was recorded (see Tab. 6.7). During the FEM simulations, a mesh composed by hexaedral elements was used, with a size of 5 mm.

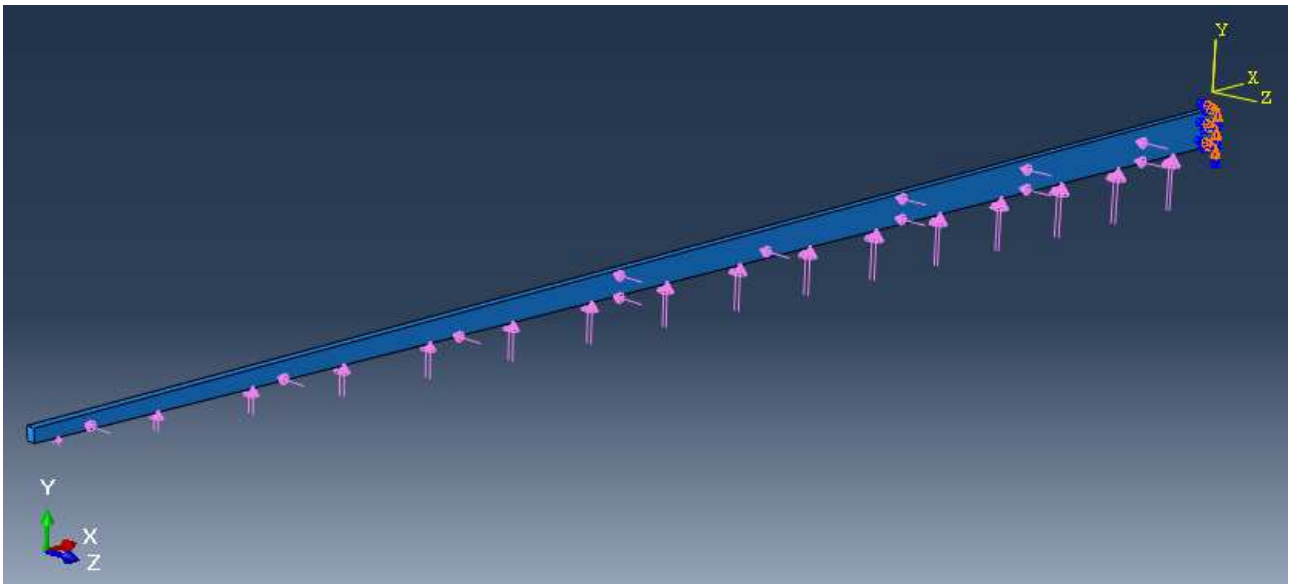

Figure 6.9: the elliptical lift distribution and the aerodynamic drag are assumed to be born by the main shear web.

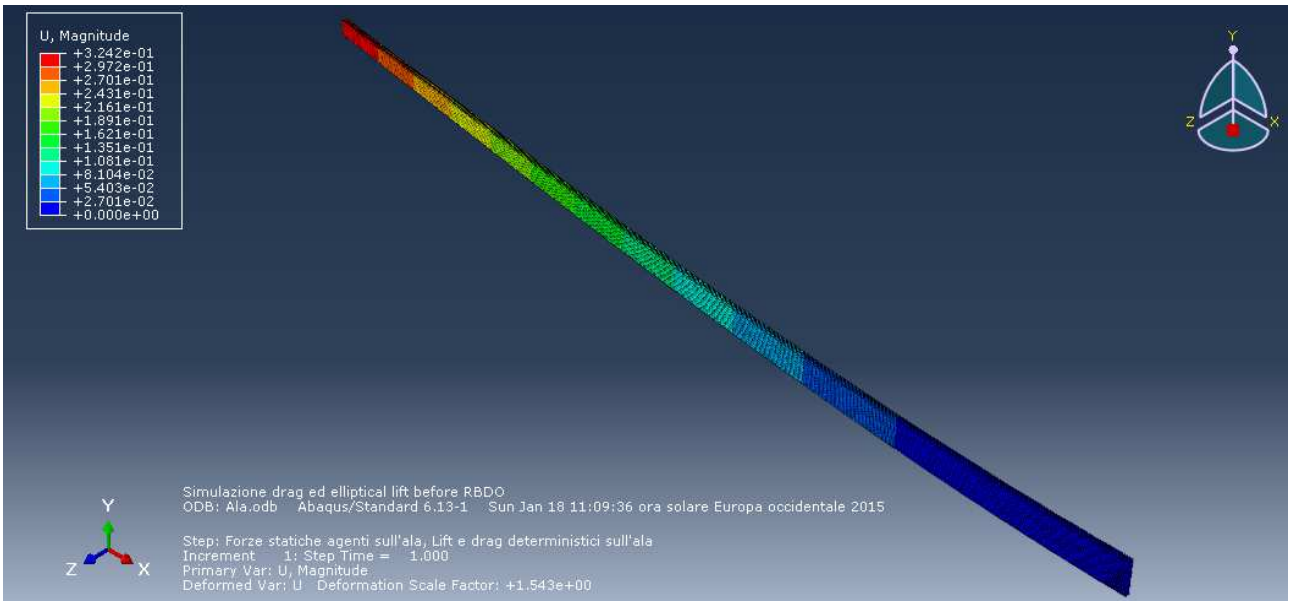

Figure 6.10: wing deformation relative to experiment no. 7 (see Tab. 6.7).

Performance function surrogate model

The constraint involves each of the three design variables. Therefore, the surrogate expression for performance function g_1 can be stated in the following form:

$$Y_1^{exp} = \beta_0 + \beta_1 * X_1' + \beta_2 * X_2' + \beta_3 * X_3' \tag{6.32}$$

where

$$X_i' = \frac{2(X_i - X_{i,min})}{X_{i,max} - X_{i,min}} - 1 \tag{6.33}$$

As for the surrogate performance function, the DOE matrix is reported below.

Table 6.7: DOE matrix related to g_1 (mesh size = 5 mm).

Experiment no.	$\boldsymbol{X_1'(t_R)}$	$\boldsymbol{X_2'(t_T)}$	$\boldsymbol{X_3'(t_c)}$	$\boldsymbol{Y_i^{EXP}}$
1	-1	-1	-1	295.6 mm
2	-1	-1	+1	88.89 mm
3	-1	+1	-1	408.9 mm
4	-1	+1	+1	118.6 mm
5	+1	-1	-1	245.2 mm
6	+1	-1	+1	70.57 mm
7	+1	+1	-1	324.2 mm
8	+1	+1	+1	92.9 mm

Now, let us determine the values of the β_i coefficients:

$$\beta_0 = \frac{1}{8}\sum_{1}^{8} Y^{exp,i} = 205.61$$

$$P_{1+} = \frac{1}{4}(Y_5^{EXP} + Y_6^{EXP} + Y_7^{EXP} + Y_8^{EXP}) = 183.22$$

$$P_{1-} = \frac{1}{4}(Y_1^{EXP} + Y_2^{EXP} + Y_3^{EXP} + Y_4^{EXP}) = 228.00$$

$$E_1 = P_{1+} - P_{1-} = -44.78$$

$$\beta_1 = \frac{E_1}{2} = -22.39$$

$$P_{2+} = \frac{1}{4}(Y_3^{EXP} + Y_4^{EXP} + Y_7^{EXP} + Y_8^{EXP}) = 236.15$$

$$P_{2-} = \frac{1}{4}(Y_1^{EXP} + Y_2^{EXP} + Y_5^{EXP} + Y_6^{EXP}) = 175.07$$

$$E_2 = P_{2+} - P_{2-} = 61.08$$

$$\beta_2 = \frac{E_2}{2} = 30.54$$

$$P_{3+} = \frac{1}{4}(Y_2^{EXP} + Y_4^{EXP} + Y_6^{EXP} + Y_8^{EXP}) = 92.74$$

$$P_{3-} = \frac{1}{4}(Y_1^{EXP} + Y_3^{EXP} + Y_5^{EXP} + Y_7^{EXP}) = 318.48$$

$$E_3 = P_{3+} - P_{3-} = -225.74$$

$$\beta_3 = \frac{E_3}{2} = -112.87$$

Therefore, the surrogate expression of the performance function is

$$Y^1 = 205.61 - 22.39 * X_1' + 30.54 * X_2' - 112.87 * X_3' \quad (6.34)$$

Then, after substituting X_i' with X_i, one obtains the surrogate performance function:

$$Y^1 = 775.41 - 0.746 * X_1 + 1.528 * X_2 - 22.58 * X_3 \quad (6.35)$$

Hence, the RBDO problem can be put in the following form:

$$\begin{cases} find\ (t_R, t_T, t_c) \\ s.t. \\ \min(m) \\ Y(t_R, t_T, t_c) \le 0 \\ t_R^l \le t_R \le t_R^u \\ t_T^l \le t_T \le t_T^u \\ t_c^l \le t_c \le t_c^u \\ \frac{L'}{c(X)} = \mu_{\frac{L'}{c(X)}} + 3 * \sigma_{\frac{L'}{c(X)}} \\ \frac{D}{A_L} = \mu_{\frac{D}{A_L}} + 3 * \sigma_{\frac{D}{A_L}} \\ E = \mu_E - 3 * \sigma_E \end{cases} \quad (6.36)$$

Such a problem is solved via a commercial routine employing a genetic algorithm.

As for the optimization outputs, the following optimal design parameters $(t_R, t_T, t_c)_{opt}$ that were found through the GA-based RBDO are:

$t_{R,opt}$ *= 133.35 mm;*

$t_{T,opt}$ *= 40.00 mm;* (6.37)

$t_{c,opt}$ *= 28.21 mm;*

objective function:

m_{opt} *= 34.36 kg.*

Reliability assessment

Now, let us set up the reliability analysis to determine a posteriori the probability of failure of the resulting configuration; to do so, let us consider the resulting design parameters as fixed values, and let us build the surrogate model Y_2 for the constraint as a function of the random variables. Therefore, the random variables will now be used as the interval variables for Response Surface Methodology.

$$\frac{L'}{c} = \left[\mu_{\frac{L'}{c(X)}} - 3 * \sigma_{\frac{L'}{c(X)}}, \mu_{\frac{L'}{c(X)}} + 3 * \sigma_{\frac{L'}{c(X)}}\right] =$$

$$\left[909.96\sqrt{\left\{1 - \left[\frac{2(\mathrm{X}-0.5)}{11}\right]^2\right\}}, 1690.25\sqrt{\left\{1 - \left[\frac{2(\mathrm{X}-0.5)}{11}\right]^2\right\}}\right]\left[\frac{N}{m^2}\right] \quad (6.38)$$

$$\frac{D}{A_L} = \left[\mu_{\frac{D}{A_L}} - 3 * \sigma_{\frac{D}{A_L}},\ \mu_{\frac{D}{A_L}} + 3 * \sigma_{\frac{D}{A_L}}\right] = [136.70, 184.94]\left[\frac{N}{m^2}\right] \quad (6.39)$$

$$E = [\mu_E - 3 * \sigma_E,\ \mu_E + 3 * \sigma_E] = [50.19 \cdot 10^9, 93.21 \cdot 10^9]\left[\frac{N}{m^2}\right] \quad (6.40)$$

The interval variables are renamed as follows:

$$X_1 = \frac{L'}{c},\ X_2 = \frac{D}{A_L},\ X_3 = E \quad (6.41)$$

which haven't to be confused with X, i.e., the direction of the wingspan (see Fig. 6.9 and 6.10). X_1 represents the amplitude of L'/c, which varies locally as a function of the position along the wingspan.

Performance function surrogate model

As for the constraint, it involves each of these three design variables. Therefore, the surrogate expression Y_2 (expressed as a function of the random variables) for the performance function can be stated in the following form:

$$Y_2 = \beta_0 + \beta_1 * X_1' + \beta_2 * X_2' + \beta_3 * X_3' \quad (6.42)$$

where

$$X_i' = \frac{2(X_i - X_{i,min})}{X_{i,max} - X_{i,min}} - 1 \quad (6.43)$$

Only the extreme values of each of the interval variables will be here considered.

As for the first surrogate performance function, the DOE matrix is

Table 6.8: DOE matrix related to g_2 (mesh size = 5 mm).

Experiment no.	$X_1'\left(\frac{L'}{c}\right)$	$X_2'\left(\frac{D}{A_L}\right)$	$X_3'(E)$	Y_i^{EXP}
1	-1	-1	-1	66.97 mm
2	-1	-1	+1	36.06 mm
3	-1	+1	-1	90.37 mm
4	-1	+1	+1	48.66 mm
5	+1	-1	-1	67.93 mm
6	+1	-1	+1	36.58 mm
7	+1	+1	-1	91.08 mm
8	+1	+1	+1	49.04 mm

Now, let us determine the values of the β_i coefficients:

$$\beta_0 = \frac{1}{8}\sum_{1}^{8} Y^{exp,i} = 60.84$$

$$P_{1+} = \frac{1}{4}(Y_5^{EXP} + Y_6^{EXP} + Y_7^{EXP} + Y_8^{EXP}) = 61.16$$

$$P_{1-} = \frac{1}{4}(Y_1^{EXP} + Y_2^{EXP} + Y_3^{EXP} + Y_4^{EXP}) = 60.52$$

$$E_1 = P_{1+} - P_{1-} = 0.64$$

$$\beta_1 = \frac{E_1}{2} = 0.32$$

$$P_{2+} = \frac{1}{4}(Y_3^{EXP} + Y_4^{EXP} + Y_7^{EXP} + Y_8^{EXP}) = 69.79$$

$$P_{2-} = \frac{1}{4}(Y_1^{EXP} + Y_2^{EXP} + Y_5^{EXP} + Y_6^{EXP}) = 51.89$$

$$E_2 = P_{2+} - P_{2-} = 17.9$$

$$\beta_2 = \frac{E_2}{2} = 8.95$$

$$P_{3+} = \frac{1}{4}(Y_2^{EXP} + Y_4^{EXP} + Y_6^{EXP} + Y_8^{EXP}) = 42.59$$

$$P_{3-} = \frac{1}{4}(Y_1^{EXP} + Y_3^{EXP} + Y_5^{EXP} + Y_7^{EXP}) = 79.09$$

$$E_3 = P_{3+} - P_{3-} = -36.5$$

$$\beta_3 = \frac{E_3}{2} = -18.25$$

Therefore, the surrogate expression of the performance function is

$$Y^2 = 60.84 + 0.32 * X_1' + 8.95 * X_2' - 18.25 * X_3' \quad (6.44)$$

Then, after substituting X_i' with X_i,

$$Y^2 = 60.95 + 0.0008202 * X_1 + 0.371 * X_2 - 0.8484 * 10^{-9} * X_3 \quad (6.45)$$

Now, the probability of failure can be assessed via Monte Carlo Simulation (MCS), by random sampling on the probabilistic variables according to their distribution. The probability of failure after 10^6 iterations results to be

$$p_f = 0.0089$$

i.e., 0.89 %. If this result doesn't meet the desired value, this RBDO process can be repeated iteratively by varying the allowed intervals of the design variables (i.e., the shear web cross-sectional dimensions), until the target reliability is reached.

6.5. Conclusions

In the present chapter, an efficient approach for the reliability-based design optimization of an airfoil structure is presented. The uncertainties affecting the system are due to the randomness in the material properties. An elastic axis-based RBDO technique is proposed, whose design objectives are mass minimization as well as the achievement of aeroelastic stability; at the same time, the prearranged levels of reliability in satisfying the constraints must be guaranteed. Here, the design variables are the thicknesses of the shear webs and their position along the chord: their final values are those that minimize the wing cross-sectional area and the distance between the elastic axis and the aerodynamic center. The probabilistic constraints define the minimum required values for the bending and torsional stiffness of the section. The overall RBDO problem is solved through a Performance Measure Approach which employs inverse first-order reliability analysis for evaluating the probabilistic constraints. Along with the reliability-based design, the same problem was solved through deterministic optimization too. The comparation of the results from these two methods highlights that the RBDO-based approach allows to minimize the objective function while meeting all the established reliability requirements. Subsequently, a rectangular wing was analyzed, in which the design goal was to find the geometrical features such that the wing mass is minimized, while respecting the probabilistic constraints on the maximum allowed stress at the wing root and the maximum allowed wingtip deflection. The RBDO approach is based on the use of a genetic algorithm, in which the random variables are given a value corresponding to the *99.87*-percentile most critical case; then, the system reliability is computed via MCS; if the probability of failure doesn't meet the desired value, the RBDO loop can be repeated, after having varied the allowed

intervals for the design variables, until the target reliability is found. Finally, the main shear web of an ultralight aircraft was studied, which experiences a set of forces due to drag and elliptical lift distribution. Furthermore, the set-up for its reliability-based design was arranged. The objective of the simulation was to determine the shear web dimensions (of its cross-section at different positions) such that its mass is minimized, while respecting the probabilistic constraints on the maximum tip deflection. Due to the difficulty to derive an analytical model for this system, the performance function was derived through applying Response Surface Methodology on a FEM model of the structure. Once the expression for the probabilistic constraint was obtained, the optimum design parameters were computed. Then, in order to be able to determine the design reliability, RSM was used again to derive a surrogate model based on the random variables. The structural reliability is then computed by using MCS. The described process can be performed iteratively, until the desired probability of failure is obtained.

Chapter 7

Conclusions and recommendations for future work

7.1. Conclusions

The need for enhancing reliability, together with the ever increasing demand for improved performances, are among the prevailing objectives in all the engineering fields. This is particularly true in aerospace applications, where the contemporary needs to reduce costs and enhancing safety look like as contradictory. Therefore, in the last years, a new field of study was developed, which aims to balance these contrasting needs; this new branch is called Reliability-Based Design Optimization (RBDO).

The main goal of the present work was to develop a RBDO methodology which is devoted to the structural aerospace design.

The road map that was followed during this thesis starts from the theoretical basics of both reliability analysis and deterministic optimization, and then merges these two subjects together, by focusing on probabilistic design. Chapter 1 is mainly introductory, whereas Chapter 2 aims to supply the prerequisites for the comprehension of reliability assessment methodologies. To begin with, the concept of uncertainty modeling is presented, which serves to provide a mathematical quantification of uncertainty. Therefore, a brief introduction to the fundamentals of probability theory and statistics was made, through which the uncertainty can be expressed as a random variable with its probability distribution. The latter functions as the input to uncertainty analysis; hence, the central concepts of performance function and probability of failure were introduced. Chapter 3 deals with the principal methods for determining the reliability of a system: Monte Carlo Simulation (MCS), First and Second Order Reliability Methods (FORM and SORM), and First Order Second Moment method (FOSM). These methods were then applied to some structural cases; MCS proved to be the most accurate, but also the most time-consuming; FORM, on the other hand, provided the best compromise between accuracy and computational burden. Also, inverse reliability analysis was introduced, which is very suitable for performing the reliability assessment loops in RBDO. Chapter 4 serves to introduce optimization, which aims to satisfy the need of finding those design variables that maximize (or minimize) a certain performance, while complying with some feasibility requirements. Optimization can be performed in different ways: for the most elementary cases, one can come to the theoretically exact solution by using the analytical method [which employs the *Karush-Kuhn-Tucker (KKT) conditions*] or the *graphical method*; anyway, in order to manage engineering applications, numerical methods are normally used. *Genetic algorithms (GA)* and *gradient-based numerical methods* are among the most widely employed. In the latter ones, at every iteration, the optimizer evaluates the objective function, the constraint functions and their derivatives and, based on their values, a search direction is generated, along which the objective function will be likely to descend with the specified step size; the process continues until convergence is reached. These methods are normally very accurate, but sometimes can converge to local minima rather than to the global minimum. Conversely, GA are not dependent on the starting point; this kind of algorithm mimics the process of natural selection, in which each of the possible model configurations is represented as a string of numbers (like chromosomes in nature). The

various strings undergo a process of breeding through some mechanisms like *crossover* and *mutation* (which are borrowed from Biology), until the optimal solution has been found. Two examples were analyzed and solved via a gradient-based numerical method, and one of them was also verified through the graphical method.
Chapter 5 aims to introduce the reader to the concept of Reliability-Based Design Optimization (RBDO). In a RBDO problem, a reliability assessment loop is nested into an optimization loop; the two coupled loops are performed repeatedly, until convergence is reached. In many practical applications, it is more useful to implement *inverse reliability analysis* in the inner loop, so as to set the desired level of reliability, rather than computing a posteriori the probability of failure. Then, a very simple RBDO algorithm that was developed is presented; subsequently, it was successfully applied to the probabilistic design of a cantilever beam; the reliability of the resulting geometrical configuration was then verified via MCS. Finally, two of the best-established RBDO algorithms were introduced: Reliability Index Approach (RIA) and Performance Measure Approach (PMA); RIA employs direct reliability analysis for assessing the probability of failure, whereas PMA is based on inverse reliability analysis, which is executed by using *inverse FORM (iFORM)*.
Eventually, Chapter 6 is devoted to the reliability-based design of some aeronautical structures, and aims to describe RBDO cases with an increasing level of lifelikeness. At first, a two-dimensional case was considered, consisting in the cross-section of a rectangular wing. In addition to the minimization of the cross-sectional area, another objective was the minimization of the distance between the aerodynamic center and the elastic axis, in order to prevent aeroelastic instabilities. The structure was subject to probabilistic constraints on the minimum required bending and torsional stiffness of the wing section, where the uncertainty term concerned the material properties, which were subject to a normal distribution. The simulations were carried on through a RBDO algorithm employing PMA. The reliability of the resulting geometry was then successfully verified via MCS. Subsequently, a three-dimensional, rectangular wing was analyzed: the design objective was to minimize the mass, while respecting the probabilistic constraints on the maximum tip displacement and on the maximum axial stress. A genetic algorithm was used for optimization, and Response Surface Methodology (RSM) was used to simplify the performance functions. Two simulations were carried on: one by using the original performance function, and the other one by using RSM. The RSM-based surrogate model proved to mimic the original constraint in a very accurate way; indeed, the resulting wing geometry and mass were very similar in the two cases. Then, a more realistic aeronautical application was considered: the reliability-based design of the main shear web of a wing, which is subject to an elliptical lift distribution and a drag force that are compatible to those that affect a four-seat, ultralight aircraft; the aerodynamic forces and the Young's modulus were subject to a gaussian distribution. The goal of the probabilistic design was to find the geometrical features which both minimize the structural mass and respect the probabilistic constraints on the maximum admissible tip deflection. As an analytical expression for the probabilistic constraint is not easy to be derived, a polynomial surrogate model was used, which was obtained by computing the response of a FEM model at some preset design points through RSM. As for the optimization algorithm, a genetic algorithm was used, and the random variables were set to their 99.87-percentile most critical value. Subsequently, the system probability of failure was computed by using MCS. The described process can be conducted repeatedly, until the desired reliability level is reached.

7.2. Final remarks and future works

The present work is devoted to both new applications of Reliability-Based Design Optimization (RBDO) algorithms and to the investigation of original possible methodologies for probabilistic design. A very simple RBDO algorithm was created and applied to the sizing of an elementary

structure: the resulting geometry proved to be compliant to the desired safety level. Then, some already existing and well-established RBDO algorithms were applied to perform a probabilistic design based on the elastic axis of a rectangular wing section; the results obtained were very promising, and brought to a structural configuration that allows to prevent aeroelastic instabilities. Then, some three-dimensional applications were analyzed, in which the RBDO procedure consists on an optimization loop via a genetic algorithm, followed by a direct reliability analysis loop (by using FORM); the procedure has to be repeated until the desired reliability level has been reached. Before all these analyses, starting from the very theoretical basics, the main reliability analysis and deterministic optimization algorithms were addressed; such an activity served as a prerequisite to the execution of the study that was proposed above.

As for the future steps, the probabilistic design based on elastic axis is planned to be applied to the analysis of very flexible wings, whose behavior can be described via the nonlinear beam theory; moreover, the probabilistic forces due to random gusts will be taken into consideration during the design. These analyses will provide an as good as possible realistic model, which will serve to enhance the prevention of aeroelastic instabilities in three-dimensional models. On the other hand, the study of the behavior of the different RBDO methods will be deepened, in order to find the one that is the most suitable for this kind of applications. The overall aim of these future works is to come to an unified approach for the probabilistic optimization of a wing structure.

Bibliography

1. Abbott, I.H., von Doenhoff, A.E., Theory of Wing Sections, Dover Publications, Inc., New York, 1959.
2. Anderson J. D. Jr., Fundamentals of Aerodynamics, Third Edition, Mc Graw-Hill, 2001.
3. Belan M., Corso di Fluidodinamica-Aerodinamica II, third version, July 2004, Politecnico di Milano, http://www.aero.polimi.it/~belan/bacheca/FluidoAeroII/dispense/cap19.pdf
4. Boin A. et al., Assessing NASA's Safety Culture: The Limits and Possibilities of High-Reliability Theory, Public Administration Review, November | December 2008, 1050-1062.
5. Bradley N., The Response Surface Methodology, Msc Thesis, Department of Mathematical Sciences, Indiana University of South Bend, 2007.
6. Breitung K. (1984), Asymptotic Approximations for Multinormal Integrals. ASCE Journal of Engineering Mechanics 110(3):357–366.
7. E. L. Brown, "Integrated strain actuation in aircraft with highly flexible composite wings", Ph.D. thesis, Massachusetts Institute of Technology, June 2003.
8. C. E. S. Cesnik, E. L. Brown, "Modeling of high aspect ratio active flexible wings for roll control", 43rd AIAA/ASME/ASCE/AHS/ASC Structures, Structural Dynamics, and Materials Con 22-25 April 2002, Denver, Colorado.
9. Cevher V. et al., Importance Sampling, 17th November, 2008, Rice University STAT 631 / ELEC 639: Graphical Models.
10. Clough, R.W., Penzien, J., Dynamics of Structures, Mc Graw-Hill, 1975.
11. Coccon M. N., Menegozzo M., Galvanetto U., A new methodology in Reliability-Based Design Optimisation for Aeronautical Structures, Royal Aeronautical Society *4th Aircraft Structural Design Conference* Conf. Proc., Belfast, Northern Ireland, 7th - 9th October, 2014.
12. Coccon M. N., Menegozzo M., Galvanetto U., New methodologies in Reliability-Based Design Optimization for Aerospace Structures, WCCM XI - ECCM V - ECFD VI 2014 Conf. Proc., Barcelona, Spain, 20th - 25th July, 2014.
13. Der Kiureghian A. et al., Second-Order Reliability Approximations, Journal of Engineering Mechanics, Volume 113, Issue 8 (August 1987), 1208-1225.
14. Der Kiureghian A. First- and second-order reliability methods. In: Nikolaidis E., Ghiocel D.M., Singhal S., editors. Engineering design reliability handbook. Boca Raton (FL): CRC Press; 2005. Chapter 14.
15. Du X, Guo J, Beeram H. Sequential optimization and reliability assessment for multidisciplinary systems design. Journal of Structural and Multidisci- plinary Optimization 2008;35(2):117–30.
16. Du X., Chen W., A Most Probable Point Based Method for Uncertainty Analysis,Proceedings of DETC'00 ASME 2000, Design Engineering Technical Conferences and Computers and Information in Engineering Conference Baltimore, Maryland, September 10-13, 2000.
17. Du X., Probabilistic Engineering Design, 2006, Missouri University of Science and Technology.
18. Engebretsen, K., Winterstein, S. R., Probabilistic Specification of Metocean Criteria: Generating and Search N-Year Contours for Extreme Response Estimation: The HTCNTR, IFORM, and SURFIT Routines, Reliability of Marine Structures Program, Report No. RMS-32, June 1998, University of Stanford, California.
19. Ferus F., Master Degree Thesis in Aerospace Engineering, University of Padova, 2013.
20. Frangopol D. M., Maute K., Life-cycle reliability-based optimization of civil and aerospace structures, Computers and Structures 81 (2003) 397–410.
21. Frangopol D. M., Maute K., Reliability-Based Optimization of Civil and Aerospace Structural Systems. Chapter 24 in: Engineering Design Reliability Handbook, Ed. Nikolaidis E., Ghiocel D.M., Singhal S., CRC Press LCC, 2005.

22. Guo J., Du X., Reliability Analysis for Multidisciplinary Systems with Random and Interval Variables, AIAA Journal Vol. 48, No. 1, January 2010.
23. Güneş M., Random-Variate Generation, University of Berlin, 2012.
24. Haftka, R. T., First Order Reliability Method, Lectures, University of Florida.
25. Hasofer, A.M. and Lind, N.C., 1974, "Exact and Invariant Second-Moment Code Format," Journal of the Engineering Mechanics Division, ASCE, Vol. 100, pp. 111-121.
26. Helton JC, Johnson JD, Sallaberry CJ, Storlie CB. Survey of sampling-based methods for uncertainty and sensitivity analysis. SAND2006-2901. Sandia National Laboratories; 2006.
27. Holland, J. H., Genetic Algorithms, Scholarpedia, 7(12):1482, 2012.
28. http://risk-reliability.uniandes.edu.co/
29. http://www.airbus.com
30. http://www.physics.smu.edu/fattarus/MonteCarloLab.html
31. http://www.matweb.com
32. http://www.mathworks.com
33. http://www.statisticalengineering.com/FORMSORM.htm
34. S.H. Huo, F.S. Wang, Z. Yuan and Z.F. Yue, "Composite wing elastic axis for aeroelasticity optimization design", Aircraft Engineering and Aerospace Technology: An International Journal 85/1 (2013) 10–1.
35. IEEE guide for the definition of reliability program plans for nuclear power generating stations. IEEE Std. 933-1999, 1999.
36. Ingram-Cotton J.B., Hecht M.J., Duphily R.J., Zambrana M., Hiramoto T., O'connor C. Reliability program requirements for space systems. Aerospace Report NO.TOR-2007(8583)-6889, US The Aerospace Corporation, 2007.
37. Kim, N. H., Structural Reliability, Lectures, Universiy of Florida, 2010.
38. Kurtz N., Song J., "Cross-entropy-based adaptive importance sampling using Gaussian mixture", Structural Safety 42 (2013) 35–44.
39. Ladevèze P. et al., Validation of structural dynamics models containing uncertainties, Computer Methods in Applied Mechanics and Engineering 195 (2006) 373–393.
40. Landau DP, Binder K. A guide to Monte Carlo simulations in statistical physics. 2nd ed. New York: Cambridge University Press; 2005.
41. Lee Y. J., Finite-Element-Based System Reliability Analysis and updating of Fatigue-Induced Sequential Failures, Ph.D. dissertation, University of Illinois at Urbana-Champaign, 2012.
42. Lee Y. K. et al., A study on the techniques of estimating the probability of failure, Journal of the Chungcheong Mathematical Society, Volume 21, No. 4, December 2008.
43. Liao Y. H., Sun C. T., An Educational Genetic Algorithms Learning Tool, IEEE, May 2001.
44. Matworks, Matlab 2014 documentation, 2014.
45. Mclean, D., Automatic flight control systems. Prentice Hall International, Series in Systems and Control engineering, 1990.
46. Melchers RE. Structural reliability analysis and prediction. Chichester: John Wiley and Sons; 1999.
47. MIL-STD-785REVB reliability program for systems and equipment devel- opment and production. MIL-STD-785B, US Department of Defense, 1980.
48. Noor AK. Nondeterministic approaches and their potential for future aero- space systems. NASA/CP-2001-211050. Langley Research Center; 2001.
49. Peters, D. A. and Johnson, M. J., "Finite-State Airloads for Deformable Airfoils on Fixed and Rotating Wings", In *Symposium on Aeroelasticity and Fluid/Structure Interaction, Proceedings of the Winter Annual Meeting*. ASME, November 6 -11, 1994.
50. Peters, D. A., Karunamoorthy, S., and Cao, W. M., "Finite State Induced Flow Models; Part I: Two-Dimensional Thin Airfoil", *Journal of Aircraft*, Vol. 32, No. 2, March ñ April 1995, pp. 313-322.

51. Rackwitz R., Reliability analysis - a review and some perspectives, Structural Safety 23 (2001), 365–395
52. C. Reeves, Genetic Algorithms; chapter 3 in: Handbook of Metaheuristics, F. Glover, G.A. Kochenberger Editors, 2003.
53. Rosenblatt M., Remarks on a Multivariate Transformation, The Annals of Mathematical Statistics, Vol. 23, No. 3 (September, 1952), pp. 470-472.
54. Scalchi, M., Aerodynamic and structural design of some components of an ultralight aircraft, Msc Thesis, University of Padova, 2014.
55. Schroeder B., Cumulative Distribution Functions, Louisiana Tech University, faculty.virginia.edu.
56. Schueller G. I. et al, A critical appraisal of reliability estimation procedures for high dimensions, Probabilistic Engineering Mechanics 19 (2004) 463–474.
57. Schueller G. I. et al., Uncertainty analysis of complex structural systems, International Journal for Numerical Methods in Engineering 2009; **80**:881–913, DOI: 10.1002/nme.2549.
58. Soize C., Stochastic modeling of uncertainties in computational structural dynamics - Recent theoretical advances, Journal of Sound and Vibration (2011), doi:10.1016/j.jsv.2011.10.010.
59. Srinivas, N., Deb, K. Muiltiobjective Optimization Using Nondominated Sorting in Genetic Algorithms, Evolutionary Computation, Vol. 2, No. 3, pp. 221-248, 1994.
60. Steenackers G. et al., Robust Optimization of an Airplane Component Taking into Account the Uncertainty of the Design Parameters, *Quality and Reliability Engineering International* 2009; **25**:255–282, (www.interscience.wiley.com). DOI: 10.1002/qre.966.
61. Swiler L.P., Eldred M. S., Reliability Methods: Determining small failure probabilities, SAND 2011-5917 C, Sandia National Laboratories, Albuquerque, New Mexico.
62. Tu J, Choi K K, Young H P. “A new study on reliability-based design optimization”. Journal of Mechanical Design 1999; 121(4):557–64.
63. Tu, J. and Choi, K. K., 1997, “A Performance Measure Approach in Reliability-Based Structural Optimization.” Technical Report R97-02, Center for Computer-Aided Design, The University of Iowa, Iowa City, IA.
64. Wen Yao, Xiaoqian Chen, Wencai Luo, Michel van Tooren, Jian Guo, Review of uncertainty-based multidisciplinary design optimization methods for aerospace vehicles, Progress in Aerospace Sciences 47 (2011) 450–479.
65. Wright J., Cooper J., Introduction to Aircraft Aeroelasticity and Loads, Wiley & Sons Ltd, 2007.
66. Youn B.D., Choi K.K. and Du L., "Enriched Performance Measure Approach for Reliability-Based Design Optimization", AIAA Journal Vol. 43, No. 4, April 2005.
67. Yu X., Du X., Reliability-Based Multidisciplinary Optimization for aircraft wing design, Structure and Infrastructure Engineering, Vol. 2, Nos. 3-4, September-December 2006, 277-289.
68. Zang T.A. et al., Needs and Opportunities for Uncertainty-Based Multidisciplinary Design Methods for Aerospace Vehicles, NASA / TM-2002-211462, July 2002.
69. Zhang L., Applied Statistics, MATH3070-001: Applied Statistics, Summer 2008, University of Utah.
70. Zhao, Y. G., Ono, T., A general procedure for first/second-order reliability method (FORM/SORM), Structural Safety 21 (1999) 95-112.

Appendix A

Structural analysis of a stalically determined structure undergoing fluidodynamic forces - a deterministic example

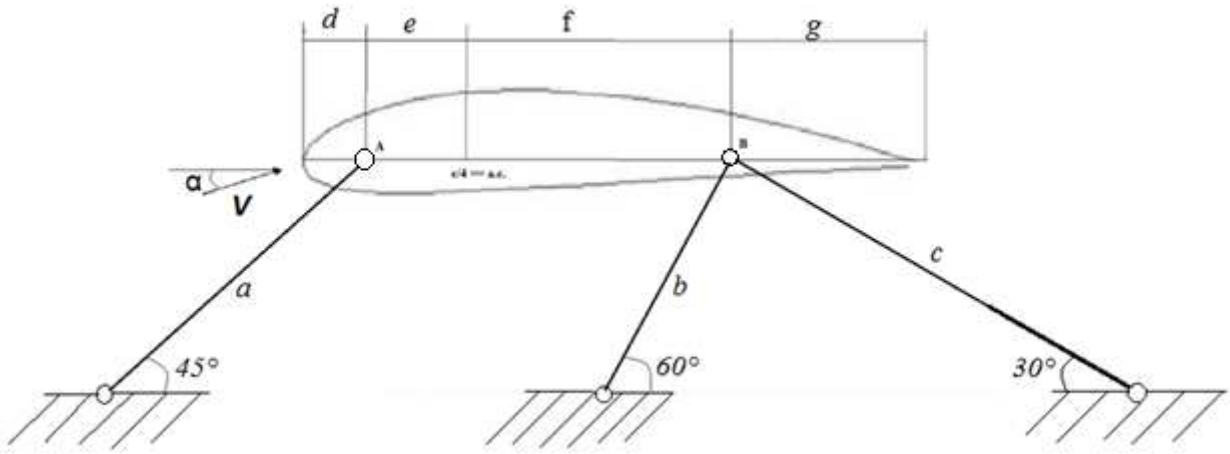

Figure A.1: the case study consists of a NACA 4415 airfoil.

As a preparatory step towards the execution of reliability analysis, a deterministic example will be considered.

A NACA 4415 airfoil of length 1.5 m and depth of 9 m passes through an air stream at different values of the angle of attack α. Such an airfoil is bound to a statically determinate structure in two nodes, called A and B. The main goal is to assess the value of the stresses on each of the three rods which the structure consists of. The problem data are herein provided.

A.1. Problem data

Air characteristics:

T = 288 K

Density ρ = 1.225 $\frac{kg}{m^3}$

Dynamic viscosity μ = $1.81*10^{-5}\ Pa*s$

Air velocity: 83.333 m/s (= 300 km/h)

Structural features:

the NACA 4415 airfoil is considered as a rigid body, and it is restrained by three rods, which are oriented as shown in figure 1. The bars have circular section, with the following values for the diameters and their respective cross-sectional areas:

$$d_a = 24\,mm \;=>\; A_a = 452.39mm^2$$

$$d_b = 15\,mm \;=> A_b = 176.71mm^2$$

$$d_c = 15\,mm \;=> A_c = 176.71mm^2$$

The rods lengths are, respectively,

$l_a = 1000mm$;

$l_b = 816mm$;

$l_c = 1414mm$

As it can be seen in Fig. 3.19, the longitudinal dimensions of the portions of the chord (i.e., *d*, *e*, *f* and *g*) are, respectively:

d = 150 *mm*;

e = 225 *mm*;

f = 675 *mm*;

g = 450 *mm*;

Material: Al 7075-T6, with Young's Modulus E = 71700 *MPa* and yield stress $\sigma_Y = 462$ *MPa*.

A.2. Determination of the physical quantities of interest

For a given value of the angle of attack α, the values of the coefficients of lift (c_L), drag (c_D) and moment (c_m) at a quarter of the chord are provided by experimental graphs for each profile (see Figures A.2 and A.3).

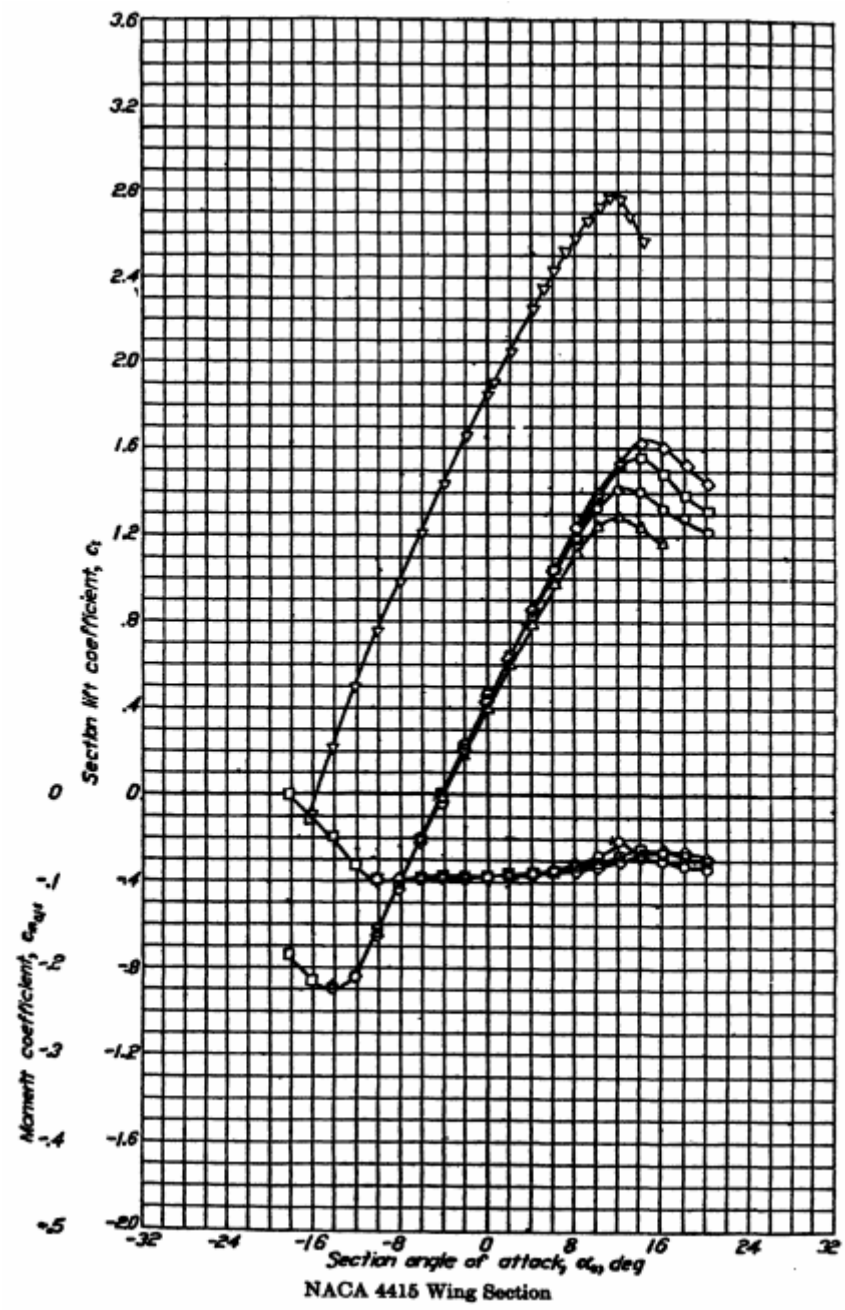

Figure A.2: Lift coefficient as a function of the angle of attack (from I. H. Abbott *et al.*, 1959).

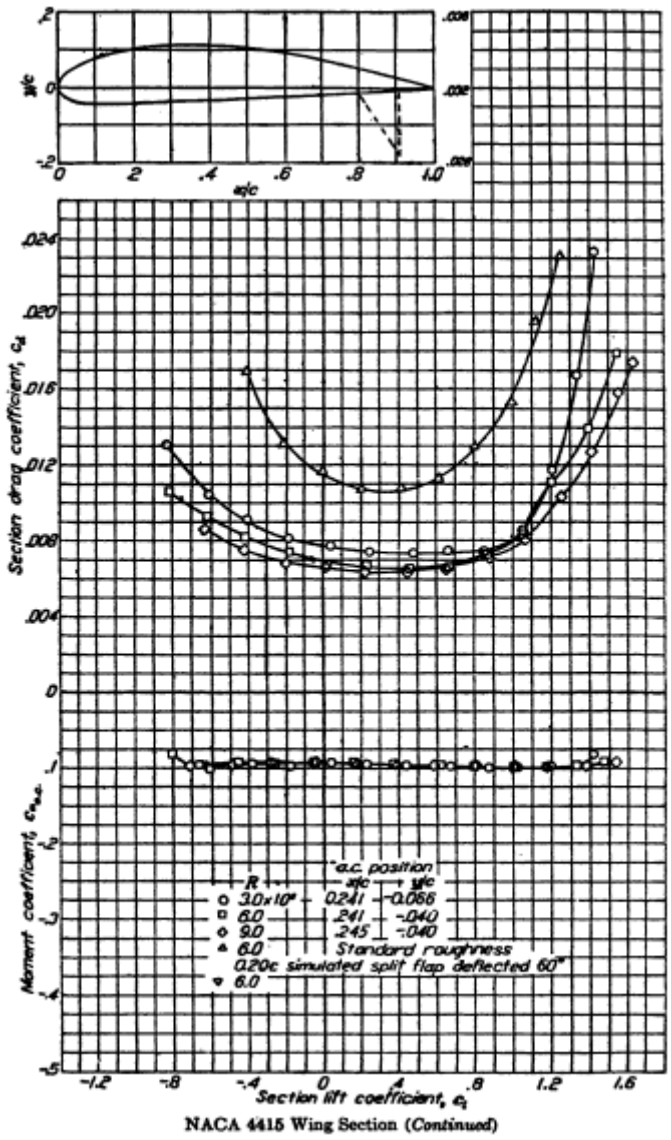

Figure A.3: Drag coefficient and momentum coefficient as a function of the lift coefficient (from I. H. Abbott *et al.*, 1959).

These coefficients are used to determine the forces and the twisting moment exerted on the airfoil by the air, according to the following formulae:

Lift:

$$L = \frac{1}{2}\rho V_\infty^2 c_L S \tag{A.1}$$

Drag:

$$D = \frac{1}{2}\rho V_\infty^2 c_D S \tag{A.2}$$

Twist moment at the aerodynamic center (for a low speed airfoil, this point is located at about 0.25**c*, i.e., at the quarter of the chord):

$$M_{AC} = \frac{1}{2}\rho V_\infty^2 c_m c S \tag{A.3}$$

Once the external forces acting on the airfoil have been obtained, the following step is to compute the reaction forces exerted by the pinned structure on the wing as a consequence of the aerodynamic stresses that are transmitted from the wing to the bars.

As for the reaction force from rod *a* (at point *A*), the only unknown is its intensity, being the direction fixed by the capability of a bar to sustain axial forces only.

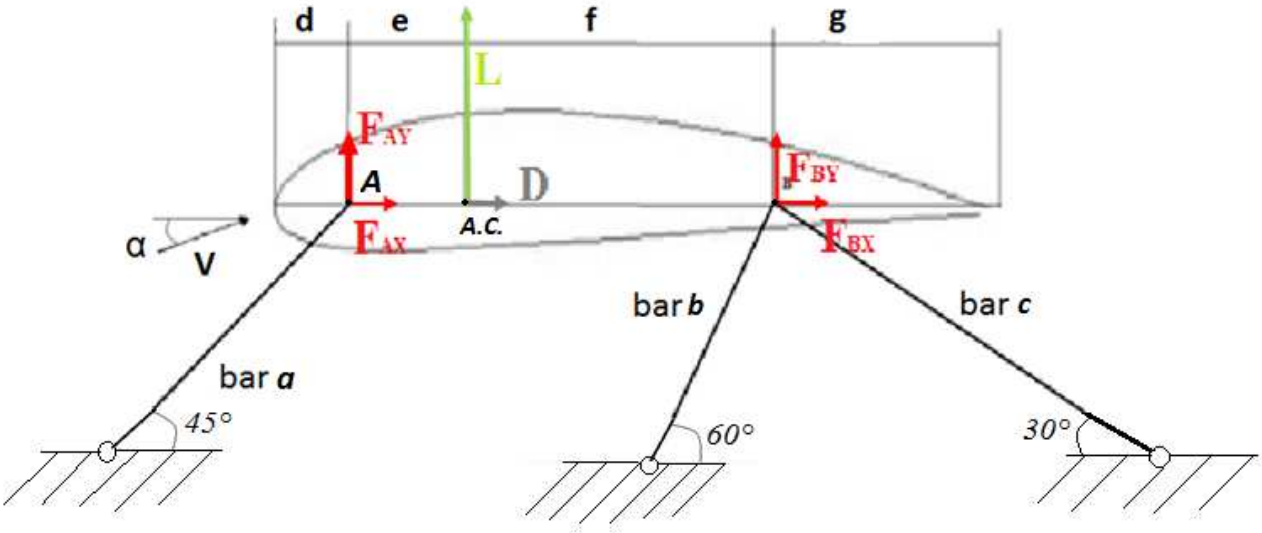

Figure A.4: The forces acting on the airfoil: Lift (*L*) and Drag (*D*) are exerted on the body by the air, while the forces highlighted in red are the reactions produced by the underlying structure on the airfoil itself.

With reference to the reaction force at point B, there are two unknowns, namely, its components on directions *x* and *y*, respectively.

To sum up, there are three unknowns, which can be determined by using equilibrium equations, namely

$$\begin{cases} \sum M_P = 0 \\ \sum F_x = 0 \\ \sum F_y = 0 \end{cases} \tag{A.4}$$

where P is a (any) point of the plane.

For the case under study, these equations have the following form:

$$\begin{cases} M_{c/4} + L \cdot e + F_{BY}(e+f) = 0 \\ F_A \cos 45° + D + F_{Bx} = 0 \\ F_A \sin 45° + L + F_{By} = 0 \end{cases} \tag{A.5}$$

Where $M_{c/4}$ is the twist moment at the aerodynamic center, which is normally considered to be equal to M_{AC}, whereas e and f are the dimensions that are shown in Fig. A.4. The solution of the aforementioned system gives the values of F_A, F_{Bx} and F_{By}.

The next step consists of deriving the reaction forces from each bar, by projecting F_A, F_{Bx} and F_{By} along the direction of the rods that are connected with each of the points A and B. The further division by the area of each bar section will provide the corresponding tensions. The final step

consists on getting the value of the displacements of points A and B along x and y directions. Positive values of the forces are related to a state of tension of the bars, while negative values indicate compression. Twist moments are considered to be positive in the anticlockwise sense. Several configurations of the airfoil were studied, which differ for the value of the angle of attack α, whereas the free stream velocity V_∞ was kept constant and equal to $83.333\ m/s$ (namely, $300\ km/h$); in each of these cases, once the aerodynamic coefficient have been obtained from the experimental graphs A.1 and A.2, they are used to compute the aerodynamic forces acting on the wing. Consequently, the three equations in the system (A.5) have three unknowns, and the forces acting on each of the rods can be easily derived. Then, the stress on the bars and the displacement of points A and B are immediately determined, and are reported in Table A.1.

Table A.1: Forces and tensions acting on the system for a fixed value of V_∞ = 83.333 m/s and varying α. The most critical case is that of α = 12°, where the safety factor for bar *c* is ν = σ_Y/σ= 1.343.

Angle of attack, α	**-3°**	**0°**	**2°**	**7°**	**12° (stall)**
Lift coefficient, c_L	0.15	0.4	0.61	1.05	1.28
Drag coefficient, c_D	0.0075	0.0075	0.0075	0.0087	0.0145
Moment coefficient at c/4, c_m	-0.1	-0.1	-0.1	-0.1	-0.09
Lift, L	8613 N	22969 N	35028 N	60292 N	73499 N
Drag, D	431 N	431 N	431 N	500 N	833 N
Twisting moment at c/4, M	-8613 N*m	-8613 N*m	-8613 N*m	-8613 N*m	-7752 N
Force acting on bar *a*	22670 N	37900 N	50687 N	77483 N	90139 N
Force acting on bar *b*	-14654 N	-16929 N	-18840 N	-22879 N	-23831 N
Force acting on bar *c*	10547 N	21667 N	31005 N	50633 N	60800 N

Tension acting on bar *a*	50 MPa	83.8 MPa	112 MPa	171.3 MPa	199.3 MPa
Tension acting on bar *b*	-82.9 MPa	-95.8 MPa	-106.6 MPa	-129.47 MPa	-134.9 MPa
Tension acting on bar *c*	59.7 MPa	122.6 MPa	175.5 MPa	286.53 MPa	344.1 MPa (ν=1.343)
f_{Ax} **displacement**	0.494 mm	0.826 mm	1.10 mm	1.689 mm	1.965 mm
f_{Ay} **displacement**	0.494 mm	0.826 mm	1.10 mm	1.689 mm	1.965 mm
f_{Bx} **displacement**	-1.40 mm	-2.55 mm	-3.51 mm	-5.524 mm	-6.47 mm
f_{By} **displacement**	-0.247 mm	0.247 mm	0.661 mm	1.527 mm	2.027 mm

A further survey that has been made consists on the study of the same model, for a fixed value of α = 0°, by varying the velocity V_∞ of the incoming air stream.

The results are summarized in Table A.2.

Table A.2: forces and tensions acting on the system for a fixed value of α = 0° and varying V_∞. The most critical case is that of V_∞ = 125 m/s, where the safety factor for bar *c* is ν = σ_Y/σ== 1.675.

Air velocity V_∞	**83.333 m/s**	**40 m/s**	**125 m/s**
Lift coefficient, c_L	0.4	0.4	0.4
Drag coefficient, c_D	0.0075	0.0075	0.0075
Moment coefficient at c/4, c_m	-0.1	-0.1	-0.1
Lift, L	22969 N	5292 N	51680 N

Drag, D	431 N	99 N	967 N
Twisting moment at c/4, M	-8613 N*m	-1984 N*m	-19375 N*m
Force acting on bar *a*	37900 N	8731 N	85266 N
Force acting on bar *b*	-16929 N	-3900 N	-38090 N
Force acting on bar *c*	21667 N	4992 N	48748 N
Tension acting on bar *a*	83.8 MPa	19.3 MPa	188.5 MPa
Tension acting on bar *b*	-95.8 MPa	-22.1 MPa	-215.6 MPa
Tension acting on bar *c*	122.6 MPa	28.2 MPa	275.9 MPa $\nu = \frac{\sigma_Y}{\sigma} = 1.675$
f_{Ax} **displacement**	0.826 mm	0.19 mm	1.859 mm
f_{Ay} **displacement**	0.826 mm	0.19 mm	1.859 mm
f_{Bx} **displacement**	-2.55 mm	-0.587 mm	-5.738 mm
f_{By} **displacement**	0.247 mm	0.0568 mm	0.555 mm

A.3. Definition of the limit-state functions

A limit-state function will be herein expressed for rod *a*, in terms of axial stress. Subsequently, the limit-state functions in terms of the displacement of point A will be considered, too.

Before the stall, the dependency of the lift coefficient from the angle of attack α is linear:

$$c_L = 2\pi * (\alpha - \alpha_{L=0}) \tag{A.6}$$

Where $\alpha_{L=0}$ is the angle at which lift is zero.

From the three equilibrium equations (A.5), and expressing c_L in the aforementioned form, it is possible to obtain the values of the axial stresses as functions of the structural characteristics and of three aerodynamic variables: α, V_∞ and ρ_∞. For the sake of simplicity, the latter two variables will be henceforth called as *V* and ρ, and the torque moment at *c/4* as *M*.

From the equation of momentum:

$$F_{BY} = \frac{-M - L*e}{e+f} \tag{A.7}$$

After some steps, the equation reduces to

$$F_{BY} = -\frac{1}{2}\rho * V^2 * S * \frac{\left(c_m * c + 2\pi * \left(\alpha - \alpha_{L=0}\right) * e\right)}{e+f} \tag{A.8}$$

Where c is the length of the chord.

From the third equation of system (A.5), one gets:

$$F_A = \sqrt{2}\left(-F_{BY} - L\right) \tag{A.9}$$

Which, after a few steps, becomes

$$F_A = -F_a = \frac{\sqrt{2}}{2} * \rho * V^2 * S\left\{\left[\frac{c_m * c + 2\pi * \left(\alpha - \alpha_{L=0}\right) * e}{e+f}\right] - 2\pi * \left(\alpha - \alpha_{L=0}\right)\right\} \tag{A.10}$$

Dividing by the cross sectional area of bar A, and changing the sign of the term on right (as focus is now on the rod), one gets

$$\sigma_a = -\frac{\sqrt{2}}{2A_a} * \rho * V^2 * S\left\{\left[\frac{c_m * c + 2\pi * \left(\alpha - \alpha_{L=0}\right) * e}{e+f}\right] - 2\pi * \left(\alpha - \alpha_{L=0}\right)\right\} \tag{A.11}$$

The performance function can therefore be expressed as

$$G_a(\rho, V, \alpha) = \sigma_a - \sigma_Y = \left(-\frac{\sqrt{2}}{2A_a} * \rho * V^2 * S\left\{\left[\frac{c_m * c + 2\pi * \left(\alpha - \alpha_{L=0}\right) * e}{e+f}\right] - 2\pi * \left(\alpha - \alpha_{L=0}\right)\right\} - \sigma_Y \le 0\right) \tag{A.12}$$

Another performance function can be introduced, in terms of the displacements of node A as an effect of the aerodynamic acting forces. Let $[K]$ be the stiffness matrix of a rod or system of rods, and let $\{\underline{F}\}$ and $\{\underline{f}\}$ be, respectively, the vector of the forces acting on the structure nodes and the vector of the displacements of the nodes, expressed in the global coordinate system (with the *x* axis aligned with the direction of motion). Thus,

$$\{\underline{F}\} = [K]\{\underline{f}\} \tag{A.13}$$

Let us call l_a, l_b and l_c, respectively, the lengths of rods *a*, *b*, and *c*.

For the case of rod *a*, where only one element is involved, one can consider that, along the bar direction:

$$F_a = K_a * f_A = \frac{E * A_a}{l_a} * f_A \tag{A.14}$$

Hence,

$$f_A = \frac{l_a}{E * A_a} * F_a = \frac{\sigma_a * l_a}{E} \tag{A.15}$$

Which, projected on the *x* and *y* axes, provides the two components of such displacement:

$$f_{Ax} = \frac{l_a}{E * A_a} * F_a * \cos\left(45^\circ\right) = \sqrt{2}/2 * \frac{\sigma_a * l_a}{E} \tag{A.16}$$

$$f_{Ay} = \frac{l_a}{E * A_a} * F_a * \cos\left(45^\circ\right) = \sqrt{2}/2 * \frac{\sigma_a * l_a}{E} \tag{A.17}$$

Equation (A.15) makes it possible to express the performance function in terms of nodal displacements, thus allowing the presence of the Young Modulus *E* in the performance function itself.

From (A.10), (A.15), and (A.16),

$$\begin{aligned} f_{Ax} &= \frac{l_a}{E * A_a} * F_a * \cos\left(45^\circ\right) = \frac{\sqrt{2}}{2} * \frac{l_a}{E * A_a} * F_a = \\ &= -\frac{1}{2} * \frac{l_a}{E * A_a} * \rho * V^2 * S\left\{\left[\frac{c_m * c + 2\pi * \left(\alpha - \alpha_{L=0}\right) * e}{e + f}\right] - 2\pi * \left(\alpha - \alpha_{L=0}\right)\right\} \end{aligned} \tag{A.18}$$

Similarly, from (A.10), (A.15) and (A.17):

$$\begin{aligned} f_{Ay} &= \frac{l_a}{E * A_a} * F_a * \cos\left(45^\circ\right) = \frac{\sqrt{2}}{2} * \frac{l_a}{E * A_a} * F_a = \\ &= -\frac{1}{2} * \frac{l_a}{E * A_a} * \rho * V^2 * S\left\{\left[\frac{c_m * c + 2\pi * \left(\alpha - \alpha_{L=0}\right) * e}{e + f}\right] - 2\pi * \left(\alpha - \alpha_{L=0}\right)\right\} \end{aligned} \tag{A.19}$$

Therefore, by fixing a *limit value* for each node in each direction (indicating it with the subscript *L*), it is possible to write the performance functions in terms of the nodal displacements:

$$G_{fAx} = G(\rho, V, \alpha, E) = f_{AX} - f_{AXL} =$$
$$\left\{ -\frac{1}{2} * \frac{l_a}{E * A_a} * \rho * V^2 * S \left\{ \left[\frac{c_m * c + 2\pi * (\alpha - \alpha_{L=0}) * e}{e + f} \right] - 2\pi * (\alpha - \alpha_{L=0}) \right\} - f_{AXL} \right\} \leq 0 \quad \text{(A.20)}$$

$$G_{fAy} = G(\rho, V, \alpha, E) = f_{AY} - f_{AYL} =$$
$$\left\{ -\frac{1}{2} * \frac{l_a}{E * A_a} * \rho * V^2 * S \left\{ \left[\frac{c_m * c + 2\pi * (\alpha - \alpha_{L=0}) * e}{e + f} \right] - 2\pi * (\alpha - \alpha_{L=0}) \right\} - f_{AYL} \right\} \leq 0 \quad \text{(A.21)}$$

Appendix B

Covariance matrices

Given a problem with *n* probabilistic physical variables, a question to deal with consists on evaluating and quantifying the physical correlation which exists between themselves, in order to make it possible to answer to the question: if there was a change on one of such variables, what would be its effect on the whole system? How considerably would the other physical quantities be affected? To deal with this problem, the correlation between these variables is often measured through the use of *covariance matrices*. A prerequisite to comprehend this tool is the knowledge of the concept of *covariance*.

Given a physical phenomenon involving two probabilistically distributed variables *X* and *Y*, and given *n* experiments or simulations, the *covariance* between *X* and *Y* is defined as

$$\mathrm{cov}(X,Y) = \sum_{i=1}^{n} \frac{1}{n-1} * \left[\left(X_i - \overline{X} \right) * \left(Y_i - \overline{Y} \right) \right] \tag{B.1}$$

where X_i and Y_i are the values of the variables corresponding to the *i*-th sample or simulation. Covariance, in other words, is a measure of how much two random variables change together.

Variance, on the other hand, involves every singular variables, and is defined (as it was seen in Eq. (2.7) and (2.8)), as

$$\mathrm{var}(X) = \sum_{i=1}^{n} \frac{1}{n-1} * \left(X_i - \overline{X} \right)^2 \tag{B.2}$$

i.e., is a measure of how spread a distribution around its mean is.

Equations (B.1) and (B.2) are valid for sufficiently great values of *n*; otherwise, the *n-1* term in the denominator turns to *n*.

The *covariance coefficient* (or *correlation coefficient*) is defined by

$$\rho(X,Y) = \frac{Cov(X,Y)}{\sigma(X) * \sigma(Y)} \tag{B.3}$$

where $\sigma(X)$ and $\sigma(Y)$ are the standard deviation of X and the standard deviation of Y, respectively.

It is important to recall that

$$\sigma(X) = \sqrt{\text{var}(X)} \tag{B.4}$$

In general, the value of a covariance coefficient ranges between -1 (anticorrelation) to 1 (complete correlation). The value 0 refers to complete uncorrelation.

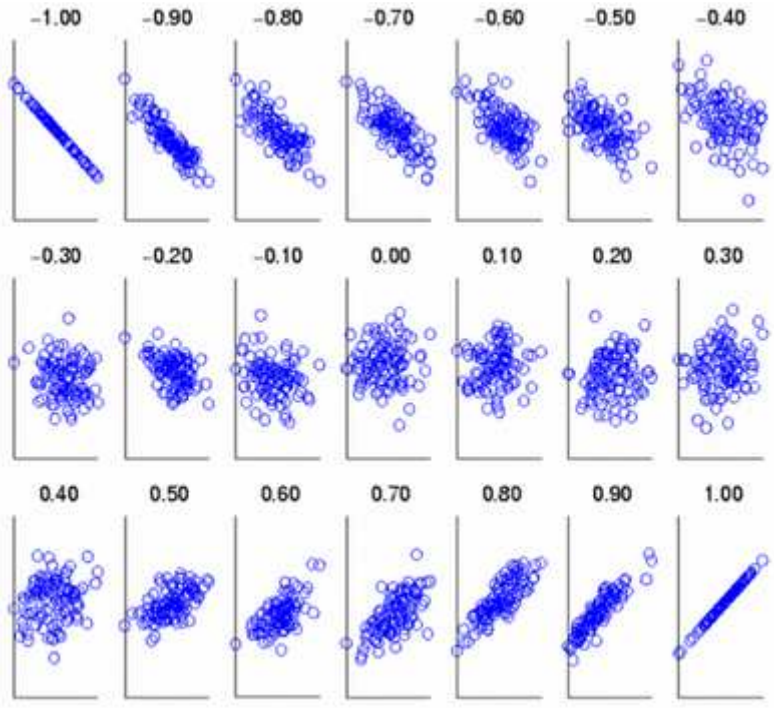

Figure B.1: some examples of statistical distributions, with their related correlation coefficients (from New York University).

With reference to the problem of section 3.5.4., the covariance matrix was built for the case of the two normally distributed random variables c_L and V. The following tables show the covariance matrix for an increasing number of simulations, which were performed via Monte Carlo. The terms in the main diagonal are variances, whereas the terms outside the main diagonal are covariances.

Covariance matrix (10^3 iterations)	c_L	V
c_L	0.0106	-0.1584
V	-0.1584	801.1573

(B.5)

Covariance matrix (10^5 iterations)	c_L	V
c_L	0.0100	0.0039
V	0.0039	906.6141

(B.6)

Covariance matrix (10^6 iterations)	c_L	V
c_L	0.0100	0.0013
V	0.0013	900.1912

(B.7)

Covariance matrix (10^7 iterations)	c_L	V
c_L	0.0100	$-5.3319*10^{-4}$
V	$-5.3319*10^{-4}$	899.7082

(B.8)

Covariance matrix (10^8 iterations)	c_L	V
c_L	0.0100	$9.2422*10^{-5}$
V	$9.2422*10^{-5}$	899.9533

(B.9)

As it can be noticed, as the number of iterations increases, the terms outside the main diagonal (i.e. the covariance terms) are approaching zero. This means that c_L and V have no correlation; indeed, this fact is correct, if one recalls that V and c_L were set as *independent* variables.

Appendix C

Deterministic optimization routines

The present appendix gathers together the Matlab routines that were used for solving the deterministic optimization problems which have been debated in chapter 4.

From paragraph 4.3.1.:

The following Matlab codes were used to minimize the *f*/*V* ratio (anyway inside a given interval) in the presence of a constraint.

Main Function

```
%Minimization of f/V ratio
d0=[150,0.675]; %starting point, V=150 m/s, f=0.675 m;
lb=[100,0.35]; %lower bounds for design variables;
ub=[200,1]; %upper bounds for design variables;
option=optimset('display','iter'); %set options to show the optimization history
d=fmincon('obj_fun',d0,[],[],[],[],lb,ub,'constr_fun',option); %call the optimizer
%Analysis at the optimal point
V=d(1);
f=d(2);
obj=f/V;
c=constr_fun(d); %calculate the constraint functions
disp(['The optimal point = ',num2str(d)]);
disp(['The objective function = ',num2str(obj)]);
disp(['The constraint functions = ',num2str(c)]);
```

Objective function

```
function obj=obj_fun(d)
%Objective function
V=d(1);
f=d(2);
obj=f/V;
```

Constraint function

```
function [c,ceq]=constr_fun(d)
%Constraint function
V=d(1);
f=d(2);

ro=1.225;    % air mass density
S=13.5;      % area of the wings
Cm=-0.1;     % momentum coefficient at a quarter of the chord
c=1.5;       % profile chord
CL=0.4;      % lift coefficient
Aa=452.39;   % area of the circular section of rod "a"

e=0.225;     % distance from node A to the quarter of the chord
c(1)=-sqrt(2)*ro*V^2*S*(Cm*c-CL*f)/(2*Aa*(e+f))-462;  % constraint

ceq=[]; % no equality constraint
```

The outputs from the optimization design of the (f/V) ratio are reported below. Here, the initial value of (f,V) for the *statically determinate profile* was set to (0.675 m; 150 m/s).

```
                                Max     Line search  Directional  First-order
 Iter F-count        f(x)   constraint   steplength   derivative   optimality Procedure
    0       3      0.0045       -0.325
    1       6   0.00445555      -0.3183            1     -0.00667      0.00667
    2       9   0.00233331            0            1     -0.00667    1.56e-005  Hessian modified

Local minimum possible. Constraints satisfied.

fmincon stopped because the predicted change in the objective function
is less than the default value of the function tolerance and constraints
are satisfied to within the default value of the constraint tolerance.

<stopping criteria details>

Active inequalities (to within options.TolCon = 1e-006):
  lower      upper     ineqlin   ineqnonlin
    2
The optimal point = 150.0015          0.35
The objective function = 0.0023333
The constraint functions = -168.6713
```

The following results refer to the case in which the initialization of (f,V) was set to (0.36 m; 199 m/s).

Iter	F-count	f(x)	Max constraint	Line search steplength	Directional derivative	First-order optimality	Procedure
0	3	0.00180905	52.45				Infeasible start point
1	6	0.00327643	17.45	1	0.00502	0.127	
2	9	0.00437076	3.459	1	0.00502	0.077	
3	12	0.00470748	0.198	1	0.00501	0.0118	
4	15	0.00472892	0.000711	1	0.00493	0.000499	Hessian modified
5	18	0.00472867	1.042e-007	1	-0.000376	0.000483	Hessian modified
6	21	0.00182699	16.45	1	-0.000376	0.00464	Hessian modified
7	24	0.00185895	0.1414	1	9.54e-006	0.00193	Hessian modified twice
8	27	0.00185923	1.082e-005	1	9.87e-006	1.82e-006	Hessian modified
9	30	0.00185923	3.411e-013	1	9.88e-006	1.18e-011	Hessian modified

Local minimum found that satisfies the constraints.

Optimization completed because the objective function is non-decreasing in
feasible directions, to within the default value of the function tolerance,
and constraints are satisfied to within the default value of the constraint tolerance.

<stopping criteria details>

Active inequalities (to within options.TolCon = 1e-006):

lower	upper	ineqlin	ineqnonlin
2			1

The optimal point = 188.25 0.35
The objective function = 0.0018592
The constraint functions = 3.4106e-013

From paragraph 4.3.2.:

In the next figure: optimization loop, outputs by *fmincon* function for (*b*,*h*) = (*50.8*, *50.8*) *mm* as starting values.

Iter	F-count	f(x)	Max constraint	Line search steplength	Directional derivative	First-order optimality	Procedure
0	3	2580.64	535.4				Infeasible start point
1	6	3761.17	186.4	1	60.8	502	
2	9	4768.89	52.01	1	53.9	489	
3	12	5342.61	5.692	1	81.5	83.3	
4	15	5386.32	1.723	1	9.18	26	
5	18	5401.17	0.5391	1	5.34	8.11	
6	21	5408.91	0.01565	1	11.4	0.234	
7	24	5409.14	0.0001908	1	3.12	0.00445	
8	27	5409.14	6.359e-09	1	7.1	2.5e-05	

Local minimum found that satisfies the constraints.

Optimization completed because the objective function is non-decreasing in
feasible directions, to within the default value of the function tolerance,
and constraints are satisfied to within the default value of the constraint tolerance.

<stopping criteria details>

Active inequalities (to within options.TolCon = 1e-06):

lower	upper	ineqlin	ineqnonlin
			1

The optimal point = 52.0055 104.011
The objective function = 5409.1443

The next figure reports the outputs by *fmincon* function for *(b,h)=(203.2, 50.8) mm* as starting values.

Iter	F-count	f(x)	Max constraint	Line search steplength	Directional derivative	First-order optimality	Procedure
0	3	10322.6	-25.4				
1	7	8368.82	-18.26	0.5	-150	1.2e+03	
2	11	7590.71	-14.46	0.5	-35.4	261	
3	16	6678.31	0.6243	0.25	-19.7	556	
4	23	6542.11	1.293	0.0625	-18	377	
5	29	6298.32	3.452	0.125	-17.8	60.1	
6	34	5892.39	9.729	0.25	-17.1	182	
7	38	5486.92	17.2	0.5	-13.1	339	
8	41	5334.88	13.72	1	-0.13	247	
9	44	5356.46	6.433	1	7.46	102	
10	47	5350.31	4.41	1	4.03	67.9	
11	50	5396.11	0.9073	1	10.9	13.5	
12	53	5407.52	0.1088	1	7.03	1.63	
13	56	5409.13	0.0009917	1	9.25	0.0148	
14	59	5409.14	4.152e-06	1	1.36	0.00238	
15	62	5409.14	1.888e-08	1	0.0852	2.67e-05	Hessian modified

Local minimum found that satisfies the constraints.

Optimization completed because the objective function is non-decreasing in
feasible directions, to within the default value of the function tolerance,
and constraints are satisfied to within the default value of the constraint tolerance.

<stopping criteria details>

Active inequalities (to within options.TolCon = 1e-06):

lower	upper	ineqlin	ineqnonlin
			1

The optimal point = 52.0055 104.011
The objective function = 5409.1443

Appendix D

Dynamic analysis of flexible wings with high aspect ratio

(From Coccon, Menegozzo and Galvanetto, 4th Royal Aeronautical Society Aircraft Structural Design Conference, Conf. Proc., 7th-9th October, 2014, Belfast, Northern Ireland).

As a preliminary step, a recall is made to the model for flexible wings with high aspect ratio, as it was proposed by Cesnik and Brown (2002) and Brown (2003). Let us consider two coordinate systems: *w*, the local one, which is attached to the deformed wing reference line (see Fig. D.1), and *B*, the inertial one, which is fixed to the airplane fuselage (indeed, it is assumed that the fuselage neither rotates nor accelerates).

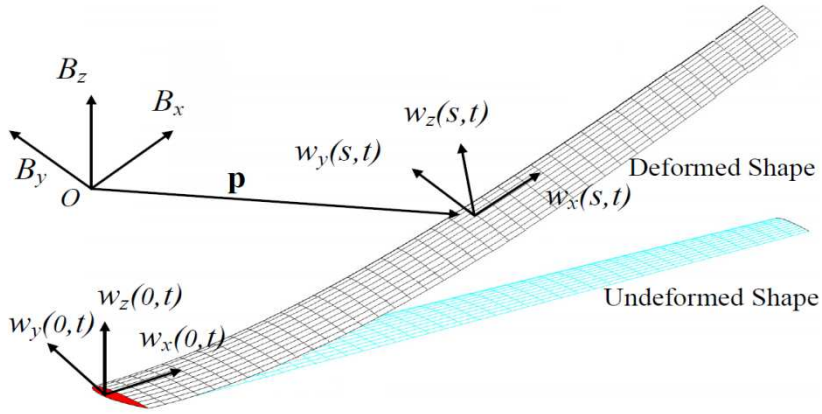

Figure D.1: Inertial and local coordinate systems of the wing (from E. L. Brown, 2003).

In the proposed formulation, the wing is sketched as a one-dimensional beam, which experiences three-dimensional bending and twisting deformations. Moreover, it is assumed that lengthwise and shear deformations are negligible. Under these hypotheses, the shape of the wing results to be determined simply by the curvature distribution along the beam coordinate, *s*:

$$\frac{\partial h(s,t)}{\partial s} = A\left(k_x, k_y, k_z\right)h(s,t) = \begin{bmatrix} 0 & I & 0 & 0 \\ 0 & 0 & k_z I & -k_y I \\ 0 & -k_z I & 0 & k_x I \\ 0 & k_y I & -k_x I & 0 \end{bmatrix} h(s,t) \qquad \text{(D.1)}$$

where $h = \left(p, w_x, w_y, w_z\right)^T$, being p the position vector of a generic point along the wing reference line, with respect to the inertial coordinate system, as well as the three component vectors w_x, w_y

and w_z. In the 12x12 square matrix, *A*, the three curvatures are indicated as k_x, k_y and k_z, while *I* is a 3x3 identity matrix. A solution for such evaluation may be attained by discretizing the beam length into n_k equally spaced coordinates, in order to identify a set of n_k-1 three-node elements, as depicted in Fig. D.2.

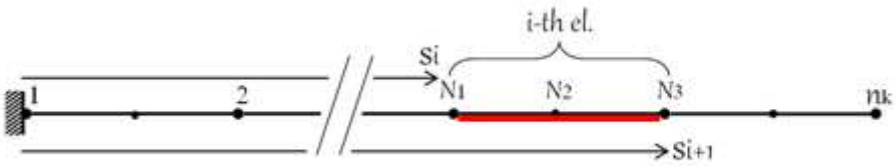

Figure D.2: Discretization of the beam reference line into n_k-1 three-node elements.

The curvature is assumed to be constant in the element, so that only the curvatures at the nodes need to be considered to solve Eq (D.1). In this way, the wing kinematics is simply defined by $3n_k$ generalized coordinates, i.e., the $3n_k$ elements of curvature vector, $\tilde{k}$, which is given by

$$\tilde{k} = \left(k_{x,1}, k_{y,1}, k_{z,1}, \dots, k_{x,n_k}, k_{y,n_k}, k_{z,n_k}\right) \tag{D.2}$$

The equation of motion is provided by the total virtual work done on the wing, which is the sum of the inertial virtual work (i.e., the work done by inertial forces, internal damping and elastic stresses) and the external virtual work (i.e., due to gravity loads and aerodynamic forces):

$$\delta W = \delta\tilde{k}^T \left(-M\frac{\partial^2\tilde{k}}{\partial t^2} - C\frac{\partial\tilde{k}}{\partial t} - K\tilde{k} + F\right) \tag{D.3}$$

From here, the equation of motion is derived by setting the total virtual work to zero; this can be done because the virtual displacement $\delta\tilde{k}$ is arbitrary. In the following, only the aerodynamic loads are calculated in order to explain the methodology proposed by Cesnik and Brown (2002) and Brown (2003).

D.1. Aerodynamic loads

The aerodynamic model used by Cesnik and Brown arises from the original formulation by Peters *et al.* (1994) and Peters *et al.* (1995). Such a theory was developed for a thin, deformable airfoil which experiences a wide motion in a subsonic flow, with small deformations about that motion.

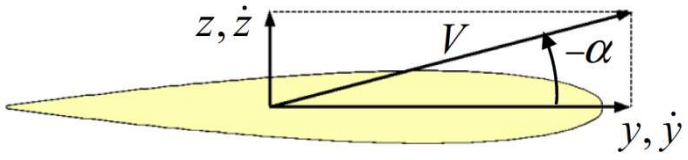

Figure D.3: airfoil motion (from Cesnik and Brown, 2002).

Lift, drag and moment are nonlinear functions of the state vector $\psi = (y, z, \alpha, \dot{y}, \dot{z}, \dot{\alpha}, \lambda_0)$ and its derivative, $\dot{\psi}$, where (y, z, α) is the instantaneous position of the airfoil (see Fig. D.3), and λ_0 is the induced flow due to the free vorticity. The lift force is expressed as

$$L = 2\pi\rho b \left\{ \dot{y} \left[\left(\frac{1}{2} b - d \right) \dot{\alpha} - \dot{z} - \lambda_0 \right] - \frac{1}{2} b \ddot{z} - \frac{1}{2} b d \ddot{\alpha} \right\} \tag{D.4}$$

where ρ is the air density, b is the airfoil semichord, and d is the distance of the beam reference line to the mid-chord.

The virtual work done by $F = (L, M, D)^T$ can be written in terms of the curvature vector, $\tilde{k}$, i.e.,

$$\delta W = \int_{s=0}^{L} (L\delta z + D\delta y + M\delta\alpha) ds = \delta\tilde{k}^T B \tilde{F} \tag{D.5}$$

where $\tilde{F}$ is the vector of the nodal aerodynamic forces, which can be linearized about the instantaneous state vector, $\left(\tilde{k}_a, \dot{\tilde{k}}_a\right)_{t=t_a}^{T}$, so that

$$\tilde{F} \cong \tilde{F}_a + \left[\tilde{F}_{\ddot{\tilde{k}}} \tilde{F}_{\dot{\tilde{k}}} \tilde{F}_{\tilde{k}} \right] \begin{Bmatrix} \ddot{\tilde{k}} \\ \dot{\tilde{k}} \\ \tilde{k} \end{Bmatrix} + \left[\tilde{F}_\lambda \tilde{F}_w \right] \begin{Bmatrix} \lambda \\ w \end{Bmatrix} \tag{D.6}$$

where the terms in square brackets are Jacobian matrixes, whereas w is the contribution of wind gusts, which can be seen as an aerofoil velocity term in Eq. (D.4). Such a term is defined according to Dryden's wind turbulence model (Mclean, 1990), which provides the following power spectral density (PSD) function:

$$S_w(\omega) = \sigma^2 \frac{L_t}{V} \frac{1 + 3\left(\frac{L_t \omega}{V}\right)^2}{\left(1 + \left(\frac{L_t \omega}{V}\right)^2\right)^2} \tag{D.7}$$

where ω is the frequency, V is the velocity of the aircraft relative to the air, L_t is the length scale of turbulence, and σ is the root mean square (RMS) of the vertical gust velocity. In order to generate the signal w in Eq. (D.6), the following relationship between the PSD of w and the PSD of a pre-generated white noise, u, can be introduced

$$S_w(\omega) = |H_{wu}(\omega)|^2 S_u(\omega) \tag{D.8}$$

Since the input signal u is a white noise, its PSD is $S_u(\omega) = 1$, therefore

$$H_{wu}(s) = \frac{w(s)}{u(s)} = \sqrt{K}\frac{a+s}{(b+s)^2} \quad \text{(D.9)}$$

where $K = 3V\sigma^2/L_t$, $a = V/(\sqrt{3}L_t)$, $b = V/L_t$, and $s = j\omega$, being j the imaginary unit. Finally, Eq. (D.9) can be represented in the state space by means of the linear filter shown in Fig. D.4, where the matrixes A, B and C are functions of the parameters K, a, b.

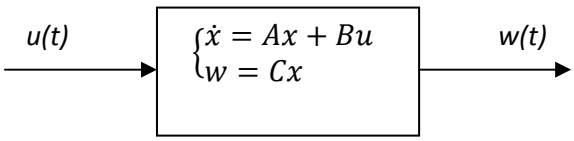

Figure D.4: Modeling atmospheric turbulence as filtered white noise.

The output signal *w(t)* represents the source of uncertainty in the reliability-based design optimization (RBDO) described in the following sections. An example of generated gust velocity is illustrated in Figure D.5.

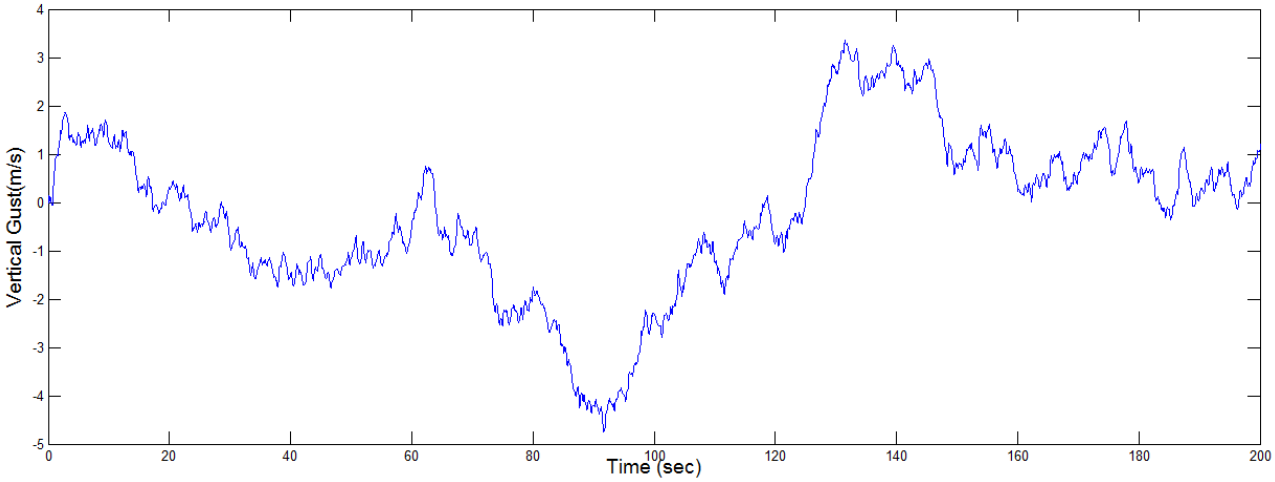

Figure D.5: Example of vertical turbulence profile.

Appendix E

Optimization design based on elastic axis

(from Coccon, Menegozzo and Galvanetto, New methodologies in Reliability-Based Design Optimization for Aerospace Structures, WCCM XI - ECCM V - ECFD VI 2014 Conf. Proc., Barcelona, Spain, 20th - 25th July, 2014).

A Multidisciplinary Design Optimization (MDO) problem has been recently proposed by Huo *et al.* (2013) to investigate the composite wing elastic axis and its influence on the aeroelasticity application problem. The elasticcentreis apoint on a section of the beam, where a shear force can be applied without inducing any torsion, and the elastic axis is the lineof all elastic centres. In general, the mechanical behavior of an aerofoil is mainly characterized by the position of three points: elastic centre, centre of mass and aerodynamic centre. Hereinafter, it will be shown that the elastic axis position plays a crucial role in the aeroelastic stability of an airfoil. Let *e* be defined as the distance of the elastic axis to the aerodynamic center, and α the airfoil attack angle, which is composed of initial attack angle, α_0, and torsion angle, θ. The aerodynamic moment on the elastic axis, M_e, can be written as

$$M_e = qScC_{MAC} + qS\left[\frac{\partial C_L}{\partial \alpha}(\alpha_0 + \theta)\right]e \tag{E.1}$$

where q is the dynamic pressure; S is the airfoil area, c is the cross section chord length; and C_{MAC} and C_L are respectively the moment and lift coefficients. If a torsional spring is used to simulate the torsional elasticity of the airfoil, i.e. $M_e = k_\theta\theta$, the equilibrium equation of aerodynamic moment and spring elastic moment can be written as

$$\theta = \frac{(qS)/(k_\theta)(e(\partial C_L/\partial\alpha)\alpha_0 + cC_{MAC})}{1-((qeS)/k_\theta)(\partial C_L/\partial\alpha)} \tag{E.2}$$

The torsion angle becomes infinite when the denominator of Eq. (E.2) equals zero, indicating that the wing is in a divergent state (instability). The corresponding divergence pressure, q_D, is given by

$$q_D = \frac{k_\theta}{eS(\partial C_L/\partial\alpha)} \tag{E.3}$$

from which it is seen that divergence instability is more likely to occur for high values of *e*. Hence, an optimization design based on elastic axis was proposed in by Huo *et al.* (2013). In this study, the wing mass and the distance from the elastic axis to the aerodynamic center define the following objective function

$$f = \frac{W_1 M}{M_{max}} + \frac{W_2 e}{c} \tag{E.4}$$

where M is the wing mass after optimization, M_{max} is the maximum wing mass in the design variable span, and W_1 and W_2 are weight coefficients. The constraints of the problem concern the maximum torsion angle, maximum strain and flutter frequency.

According to Coccon, Menegozzo and Galvanetto (2014), the optimization process described above can be extended to a reliability-based design optimization analysis, where the objective function in Eq. (E.4) is minimized while considering the uncertainties introduced by the randomness on the material properties as well as on the aerodynamic loads (random gusts).

Appendix F

Response Surface Methodology

In many physical applications, the evaluation of the performance functions can be computationally demanding, and this can be an issue, especially when their computation is required repeatedly. A possible solution is to create a surrogate physical model, whose evaluation is more simple and less expensive than the original performance function. This can be done through a sort of interpolation, i.e., by computing such a performance function (or *response function*) g, at a set of opportune, preset *design points*, which are then used to fit the simplified substitute model. This process is called Design Of Experiments (DOE). The main goal of DOE is to minimize the amount of information that is required for optimization, through selection of the appropriate points where the response should be evaluated, such that the surrogate model describes as accurately as possible the behavior of the original model. Among the possible methods for approximating the performance function, Response Surface Methodology (RSM) is one of the most popular ones, which allows to reduce the original, complex response function g to a polynomial function. The design points are taken from a set of *input variables* $\boldsymbol{X}$, each of them lying inside a preset bound. If the random variables are chosen as input variables, RSM allows to simplify the reliability assessment, which can then be performed through one of the classical methods, such as FORM, SORM or MCS. On the other hand, if the design variables are chosen as input variables, RSM results to be useful in simplifying and accelerating the optimization process.

The steps which are generally followed by RSM method are listed below.

1. Determination the design (input) variables $\boldsymbol{X}$ and the response variables g.
2. Definition of an opportune interval for each of the design variables.
3. Planning the locations of the design points where the experiment will be performed (namely, where the response function g will be evaluated) and the level of the variables (i.e., the number of design points for each of the input variables).
4. Performing the experiment to obtain the local value Y^{exp} of the response variable at each of the design points that have been determined in Step 3.
5. Derivation of the unknown coefficients of the response surface model, in order to obtain the polynomial function which represents the surrogate model behavior.
6. Using the response surface model for uncertainty assessment or for solving an optimization problem

An applicative example of application of RSM is described in the sequel, consisting on the geometrical optimization of a tapered wing shear web which undergoes a set of aerodynamic forces due to drag and elliptical lift distribution (see Fig. F.1). Due to the difficulty of deriving an analytical expression to describe the behavior of the system, the *response* (or *performance*) *function* Y is calculated at some predefined design points, each of them corresponding to a particular combination of the *input variables* X, which, in this case, are the *design variables* (i.e., the cross-sectional dimensions of the shear web, see Fig. F.2). Here, a two-level full factorial design is used,

which means that, for each input variable, two design points (i.e., levels) will be chosen, and the experiments will involve all the combinations of the design variable levels.

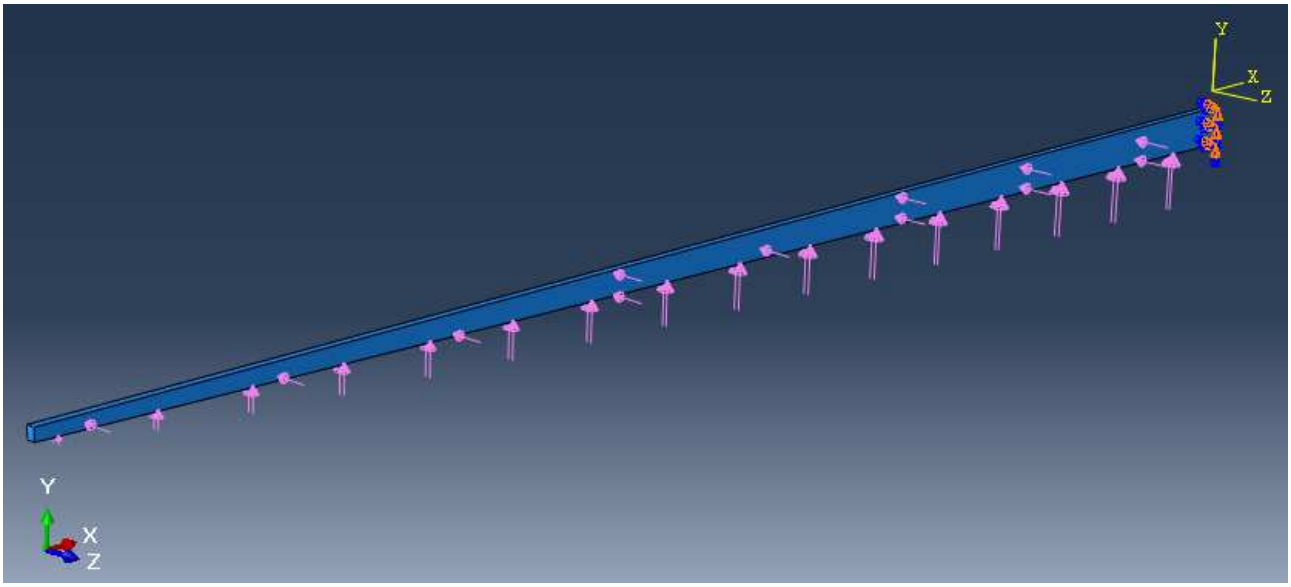

Figure F.1: the main shear web of a wing experiencing the elliptical lift distribution and the aerodynamic drag.

Figure F.2: shear web cross-sectional dimensions at the wing root (left) and at the wing tip (right).

<u>Step 1: Determination the design (input) variables *X* and the response variable *Y*</u>:
This is an optimization problem; therefore, the design variables (i.e., the cross-sectional dimensions of the shear web, see Fig. F.2) are chosen as input variables:

$$X_1 = t_R, \qquad X_2 = t_T, \qquad X_3 = t_c$$

As for the output variable *Y*, the tip displacement caused by the acting forces will be recorded for every combination of the input variables.

<u>Step 2: definition of an opportune interval for each of the design variables</u>:

$X_1 = [100, 160][mm]$,

$X_2 = [40, 80][mm]$,

$X_3 = [20, 30][mm]$;

Step 3: Planning the number of design points and the level of the input variables:

As it was previously stated, two design points (i.e., levels) will be chosen for each input variable: in this particular example, the minimum and the maximum value are chosen. For the sake of simplicity, every variable X_i is put in an adimensional form and is called X_i', which lies inside the interval [-1, +1], where -1 stands for the lower bound $X_{i,min}$, and +1 stands for the upper bound $X_{i,max}$; the relation between X_i and X_i' is:

$$X_i' = \frac{2(X_i - X_{i,min})}{X_{i,max} - X_{i,min}} - 1 \qquad \text{(F.1)}$$

Table F.1 shows the *DOE Matrix*, in which the *response* (or *performance*) *function Y* is computed for every combination of the levels of the input variables *X*, namely, for each of the design points.

Table F.1: DOE matrix; every experiment corresponds to a particular design point.

Experiment no.	X_1'	X_2'	X_3'
1	-1	-1	-1
2	-1	-1	+1
3	-1	+1	-1
4	-1	+1	+1
5	+1	-1	-1
6	+1	-1	+1
7	+1	+1	-1
8	+1	+1	+1

The polynomial function representing the surrogate model is given by

$$Y = \beta_0 + \beta_1 X_1' + \beta_2 X_2' + \beta_3 X_3' \qquad \text{(F.2)}$$

where β_i' (i= 1,2,3) are unknown coefficients, whose values will be found at Step 5.

A graphical representation of the DOE matrix is reported in Fig. F.3, where each node represents a design point.

Step 4: Performing the experiment to obtain the local value Y^{exp} of the response variable at each of the design points:

The response function Y_i^{EXP} (namely, the tip deflection, where i = 1,...,8) is calculated at the design points of Tab. F.1 by using a FEM code. The results of these experiments are reported in Tab. F.2 and Fig. F.3.

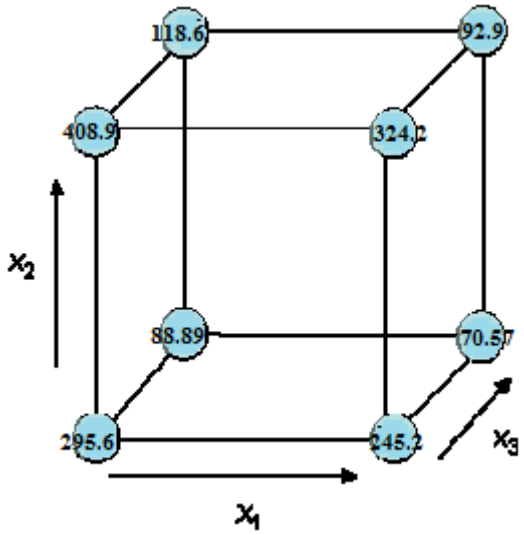

Figure F.3: graphical representation of the DOE matrix. The displacements are expressed in [mm].

Table F.2: DOE matrix with the response Y_i^{EXP} for each of the experiments.

Experiment no.	$X_1^{'}(t_R)$	$X_2^{'}(t_T)$	$X_3^{'}(t_c)$	Y_i^{EXP}
1	-1	-1	-1	295.6 mm
2	-1	-1	+1	88.89 mm
3	-1	+1	-1	408.9 mm
4	-1	+1	+1	118.6 mm
5	+1	-1	-1	245.2 mm
6	+1	-1	+1	70.57 mm
7	+1	+1	-1	324.2 mm
8	+1	+1	+1	92.9 mm

<u>Step 5: Derivation of the unknown coefficients of the response surface model, in order to obtain the polynomial function which represents the surrogate model behavior</u>:

To find the unknown coefficients β_i, one can apply the *least squares method*, by minimizing the difference between the experimental results Y_i^{exp} and the response which is predicted by the surrogate model of Eq. (F.2), namely

$$Min \sum_{i=1}^{8} \left[Y_i^{exp} - (\beta_0 + \beta_1 X_1' + \beta_2 X_2' + \beta_3 X_3') \right]^2 \qquad \text{(F.3)}$$

Another way to determine the unknown coefficients is based on the observation of the effect produced by the change of every single variable on the overall system response (i.e., the m*ain effects*).

The first coefficient is the average of the responses from all the design points, namely

$$\beta_0 = \frac{1}{8} \sum_1^8 Y^{exp,i} = 205.61 \qquad \text{(F.4)}$$

The other coefficients are derived by considering the main effect E_j of each input variable X_j', that is, the average change on the system when X_i' changes from - 1 to +1 while other variables remain unchanged.

The main effect E_j is computed as the difference between the average value P_j^+ of the response at the X_j' high level (+1) and the average value P_j^- of the response at the X_j' low level (-1) (Du, 2006), as depicted in Fig. F.4.

Now, let us compute β_1:

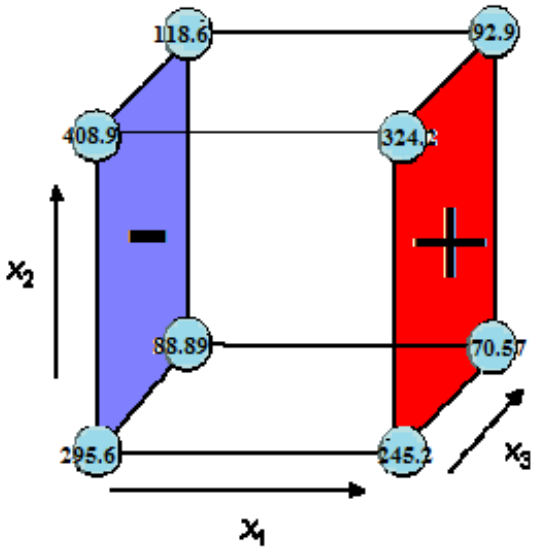

Figure F.4: the main effect of X_1', which is numerically expressed by Eq. (F.7).

With reference to Tab. F.2, the average response at X_1' high level (+1) (highlighted in red in Fig. F.4) is

$$P_{1+} = \frac{1}{4}(Y_5^{EXP} + Y_6^{EXP} + Y_7^{EXP} + Y_8^{EXP}) = 183.22 \quad \text{(F.5)}$$

whereas the average response at X_1' low level (-1) (highlighted in blue in Fig. F.4) is

$$P_{1-} = \frac{1}{4}(Y_1^{EXP} + Y_2^{EXP} + Y_3^{EXP} + Y_4^{EXP}) = 228.00 \quad \text{(F.6)}$$

Therefore, the main effect of X_1' is expressed as

$$E_1 = P_{1+} - P_{1-} = -44.78 \quad \text{(F.7)}$$

The coefficient β_1 is defined as half of the main effect E_1, namely

$$\beta_1 = \frac{E_1}{2} = -22.39 \quad \text{(F.8)}$$

The other coefficients (β_2 and β_3) are computed in an analogous way:

$$P_{2+} = \frac{1}{4}(Y_3^{EXP} + Y_4^{EXP} + Y_7^{EXP} + Y_8^{EXP}) = 236.15 \quad \text{(F.9)}$$

$$P_{2-} = \frac{1}{4}(Y_1^{EXP} + Y_2^{EXP} + Y_5^{EXP} + Y_6^{EXP}) = 175.07 \quad \text{(F.10)}$$

$$E_2 = P_{2+} - P_{2-} = 61.08 \quad \text{(F.11)}$$

$$\beta_2 = \frac{E_2}{2} = 30.54 \quad \text{(F.12)}$$

$$P_{3+} = \frac{1}{4}(Y_2^{EXP} + Y_4^{EXP} + Y_6^{EXP} + Y_8^{EXP}) = 92.74 \quad \text{(F.13)}$$

$$P_{3-} = \frac{1}{4}(Y_1^{EXP} + Y_3^{EXP} + Y_5^{EXP} + Y_7^{EXP}) = 318.48 \quad \text{(F.14)}$$

$$E_3 = P_{3+} - P_{3-} = -225.74 \quad \text{(F.15)}$$

$$\beta_3 = \frac{E_3}{2} = -112.87 \quad \text{(F.16)}$$

Therefore, the surrogate expression of the performance function is

$$Y = 205.61 - 22.39 * X_1' + 30.54 * X_2' - 112.87 * X_3' \quad \text{(F.17)}$$

Then, after substituting X_i' with X_i [see Eq. (F.1)], one obtains the surrogate performance function as a function of the original variables X_i:

$$Y = 775.41 - 0.746 * X_1 + 1.528 * X_2 - 22.58 * X_3 \quad \text{(F.18)}$$

and, recalling that $X_1 = t_R$, $X_2 = t_T$, and $X_3 = t_c$, Eq. (F.18) can be expressed as a function of the geometrical design variables:

$$Y(t_R, t_T, t_c) = 775.41 - 0.746 * t_R + 1.528 * t_T - 22.58 * t_c \quad \text{(F.19)}$$

Step 6: Using the response surface model for solving an optimization problem:

The polynomial performance function $Y(t_R, t_T, t_c)$ describing the tip displacement can now be used for optimization, by fixing a maximum allowed displacement δ_{lim} that has not to be overtook. Let the design aim be to find the geometrical features for which the shear web mass is minimized while respecting the constraint on the maximum allowed tip displacement; the problem can be formulated as:

$$\begin{cases} find\ (t_R, t_T, t_c) \\ s.t. \\ \min(m) \\ Y(t_R, t_T, t_c) - \delta_{lim} \leq 0 \\ t_R^l \leq t_R \leq t_R^u \\ t_T^l \leq t_T \leq t_T^u \\ t_c^l \leq t_c \leq t_c^u \end{cases} \tag{F.20}$$

In addition to optimization and reliability analysis, the simplification introduced by RSM can be used in probabilistic design as well, due to its usefulness in bringing down the computational effort.